Single Carrier Block Transmission in Ultra-wideband Communications

by

Yue Wang
B.Sc., Xi'an Jiaotong University, China, 1999
M.Sc., Xi'an Jiaotong University, China, 2002

A Dissertation Submitted in Partial Fulfillment of the
Requirements for the Degree of

DOCTOR OF PHILOSOPHY

In the Department of Electrical and Computer Engineering

SUPERVISORY COMMITTEE

Single Carrier Block Transmission in Ultra-wideband Communications

by

Yue Wang
B.Sc., Xi'an Jiaotong University, China, 1999
M.Sc., Xi'an Jiaotong University, China, 2002

Dr. Xiaodai Dong,

Supervisor, Department of Electrical and Computer Engineering

Dr. Aaron Gulliver

Departmental Member, Department of Electrical and Computer Engineering

Dr. Hong-chuan Yang

Departmental Member, Department of Electrical and Computer Engineering

Dr. Kui Wu

Outside Member, Department of Computer Science

Dr. John Nielsen

Additional Member, University of Calgary

Supervisory Committee

Dr. Xiaodai Dong
Supervisor

Dr. Aaron Gulliver
Departmental Member

Dr. Hong-chuan Yang
Departmental Member

Dr. Kui Wu
Outside Member

Dr. John Nielsen
Additional Member

ABSTRACT

In this thesis, single carrier block transmission with frequency-domain equalization (SC-FDE) is proposed as an alternative physical layer solution for IEEE 802.15.3a Ultra-wideband (UWB) communications to meet the high data rate and low complexity requirement. The performance of SC-FDE over UWB channels are analyzed, simulated and compared to that of the two currently existing physical layer solutions: the single carrier UWB using the direct-sequence (DS) technology and the multiband UWB utilizing the orthogonal frequency division complexing (OFDM). We show the superiority of SC-FDE over both IR-UWB and OFDM-UWB, especially when implementation issues such as low complexity and low power consumption are taken into consideration. Based on the proposed SC-FDE UWB, novel schemes are carried out to address the physical layer design issues. A low complexity frequency-domain channel estimation scheme is proposed. A novel time division multiple access (TDMA) scheme is proposed for high-speed SC-FDE UWB to address the multiple access issue. Furthermore, a novel transmitter pulse shaping design method is proposed to fit the FCC mask and introduce spectral nulls at the interference frequency band to limit the narrow band interference (NBI). In addition, the effects of imperfect channel estimation, carrier frequency offset (CFO) and sampling timing offset (STO) on the performance of SC-FDE over UWB channels are also investigated.

Table of Contents

List of Tables

List of Figures

List of Abbreviations

AWGN	additional white Gaussian noise
ADC	analog-to-digital converter
BER	bit error rate
CDMA	code division multiple access
CFO	carrier frequency offset
CLT	central limit theorem
CM	channel model
CP	cyclic prefix
CSI	channel state information
DS-UWB	direct sequence UWB
ESD	energy spectral density
FCC	Federal Communications Committee
FFT	Fast Fourier Transform
IBI	interblock interference
ICI	intercarrier interference
i.i.d.	independent and identically distributed
IFFT	inverse Fast Fourier Transform
IR	impulse radio
ISI	inter-symbol interference
LMMSE	linear mininum mean squared error
LOS	line of sight
LS	least square
MAI	multiple access interference
MBOA	Multiband OFDM Alliance
MB-OFDM	Multiband OFDM
MC-CDMA	multi-carrier code division multiple access

MIMO	multiple input multiple output
MLE	maximum-likelihood estimation
MSE	mean squared error
MMSE	minimum mean squared error
NBI	narrowband interference
NLOS	non-line of sight
OFDM	orthogonal frequency division multiplexing
PAPR	peak-to-average power ratio
PDF	probability density function
RF	radio frequency
RRC	root raised cosine
PSD	power spectrum density
RMS	root mean square
RV	random variable
SC	single carrier
SC-FDE	single carrier with frequency-domain MMSE equalization
SINR	signal-to-interference plus noise ratio
SNR	signal to noise ratio
STO	sampling time offset
SVD	singular value decomposition
S/P	serial-to-parallel
TDMA	time division multiple access
UWB	Ultra-wideband
WPAN	Wireless Personal Area Networks

Acknowledgments

First and foremost I would like to thank my supervisor, Dr. Xiaodai Dong, for her patient guidance, continuous encouragement and insightful technical advice throughout my study. This thesis work could not have been completed without the support and help from Dr. Dong.

I would like to thank Dr. Ivan Fair at the University of Alberta for the valuable ideas which spawned Chapter 5. His review and comments on the writing of Chapter 5 are also highly appreciated.

I would also like to thank Dr. Aaron Gulliver, Dr. Hong-chuan Yang and Dr. Kui Wu for the valuable suggestions on my proposal, oral exam and taking time reviewing my thesis. Special thanks to Dr. John Nielsen at the University of Calgary for being the external member.

Thanks to many of my colleagues and friends at both the University of Alberta and University of Victoria for being so nice and helpful that has made my stay in Alberta and Victoria a great pleasure. Especially, I would like to thank Xiaodi, Lei, Mohsen, Zhengang and Alfred at the University of Alberta and Dr. Wei Li, Le, Yihai, Hanfeng, Li, Rongrong, Massoud, Shiva and Omar at the University of Victoria.

Special thanks to Erik, Steve, Duncan, Vicky, Sarah, Moneca, Lynne and Mary-Anne for the many patient and constant help from them.

Last but not least, I would like to thank my parents for being so supportive all through these years. It is hard to put into word how much I appreciate their love and how grateful I feel to have them. So I will just say, thank you, Mom and Dad.

Dedication

To my parents

Chapter 1

Introduction

Ultra-wideband (UWB) is a promising radio technology owing to its potential to provide very high data rate transmission with low power and low implementation complexity. Originated as a baseband, carrier free technology, UWB has mainly been used in the intercept and detection for military and government communication systems for the past two decades. In February 2002, the Federal Communications Committee (FCC) approved the marketing and operation of UWB devices by granting the unlicensed 3.1-10.6 GHz spectrum to UWB communications [1]. Designed for short-range Wireless Personal Area Networks (WPAN) to complement the other longer range radio technologies such as Wi-Fi, WiMAX, and cellular wide area communications, UWB becomes the leading technology that brings the convenience and mobility of wireless communications to high-speed connections in devices throughout homes and offices.

1.1 Background of UWB Communications

FCC defines UWB as the communication system with a fractional bandwidth equal to or great than 20% of the center frequency, or a -10 dB bandwidth in excess of 500 MHz [1]. Having allocated up to 7.5 GHz bandwidth to UWB devices, FCC also restricted the transmission power spectrum density (PSD) of a UWB device to an extremely low level of -41.3 dBm/MHz, in order to protect the existing narrowband and wideband devices

from the interference that UWB might cause due to the overlay of the UWB spectrum [1]. Targeting at very high data rate transmission (110 Mbps at a distance of 10 meters and up to 480 Mbps at a distance of 2 meters), UWB is initially designed as a carrier-free baseband system, where data is transmitted through a train of narrow pulses. Each pulse is of very short duration and covers an extremely wide spectrum bandwidth, resulting in a highly dispersive communication environment with strong frequency selectivity. To represent the typical realistic indoor and outdoor UWB environment, four channel models (CM) have been proposed by the IEEE 802.15.3a Working Group [2], with their root mean square (RMS) delays ranging from around 5 ns to 25 ns and the maximum delay spread from 30 ns to 120 ns for CM1 to CM4, respectively.

The large bandwidth, high data rate and low complexity advantage of the UWB system has made it a promising candidate in industrial and commerical applications such as medical imaging, ranging, construction applications and high-speed home or office networking. For example, using the UWB technology will enable a medical imaging system to "see" or operate inside the body of a person, which may be used in a variety of health applications. Moreover, consumers can wirelessly and rapidly share photos, music, video and voice data among their networked PCs, mobile phones and consumer electronics such as DVD player and personal video recorder, enabling the possible removal of all the wires to the printer, scanner, mass storage devices and video cameras located in the home office [3].

The potential high data rate and low complexity property of a UWB system, on the other hand, also makes the transceiver design for UWB vastly different from that of the conventional narrowband and wideband systems. Data transmission and detection issues that have been well addressed in the traditional narrowband and wideband communications may become impractical or inferior in the world of UWB, leading to a number of system design challenges for UWB communications. For example, the large number of multipath components which could be more than 100 in typical UWB channels will preclude the implementation of the rake receiver structure where using enough rake fingers to capture all the multipath energy becomes unrealistic, especially in the non line-of-sight (NLOS) chan-

nel conditions. Moreover, in a typical UWB environment where channel can spread more than 30-100 symbol durations, severe inter-symbol interference (ISI) will be introduced, thus making equalization a major issue in UWB receiver design [4]. Additionally, system design issues such as channel estimation, multiple access and timing synchronization scheme in a UWB system will become more involved than in conventional narrowband and wideband systems.

1.2 DS-UWB vs. OFDM-UWB

Solutions targeting at addressing the physical layer design challenges in UWB systems have been presented in many research literature and standardization documents. In particular, two data transmission and detection schemes have been proposed to the IEEE 802.15.3a Working Group as the potential physical layer solution, i.e., the single carrier (SC) UWB using direct sequence (DS) spread spectrum technology introduced by XtremeSpectrum [5] and the multiband orthogonal frequency division multiplexing (OFDM) technology supported by the Multiband OFDM Alliance (MBOA) [6].

Ever since the two physical layer protocols were proposed, there have been numerous debates on the superiority of each other in terms of performance and implementation complexity [7]. DS-UWB is known to have strengths in the simple transmitter design where the baseband transmission frees the utilization of the modulator. However, when rake structures and time-domain equalization are utilized at the receiver as in most of the previous literature [5], [8], DS-UWB suffers from high complexity implementations where the large number of rake fingers and time-domain equalizer taps have to be employed to achieve a reasonable system performance. On the other hand, OFDM-UWB is gaining increasing research interest [9], [10] due to its simple receiver structure where a one-tap frequency-domain equalizer is sufficient to combat the multipath components. However, the inherent high peak-to-average-power ratio (PAPR) issue at an OFDM transmitter has become a serious issue when low power consumption in a UWB system is required.

Although the superiorities of both DS-UWB and OFDM-UWB have been well proven, neither side was able to gain the required 75 percent majority needed for confirmation in the standardization due to their respective shortcomings in system complexity and power consumption. In January 2006, while the stalemate in UWB standardization continued, the IEEE 802.15.3a Working Group decided to disband itself and leave the decision to the market. Various forms of UWB transmission and detection techniques are now allowed to coexist, thus providing opportunity for new UWB transceiver design schemes.

1.3 Single Carrier Block Transmission with Frequency-Domain Equalization

Single carrier block transmission with frequency-domain equalization (SC-FDE) is another physical layer transmission and detection technology that has been widely discussed in conventional narrowband and wideband systems. As in OFDM, SC-FDE inserts and removes cyclic prefix (CP) at the transmitter and receiver to convert the channel linear convolution into a circular convolution and make it sufficient for a one tap frequency-domain equalizer to cover the channel multipath components. However, unlike OFDM where the frequency-domain signals are converted into time domain at the transmitter, SC-FDE performs the inverse Fast Fourier Transform (IFFT) at the receiver, thus circumventing the high PAPR issue of an OFDM transmitter.

The comparisons in performance and implementation complexity between OFDM and SC-FDE were widely discussed in conventional narrowband and wideband systems [11–15], where both systems yield close performance with similar implementation complexity. However, the advantages of SC-FDE over OFDM become obvious when it comes to UWB communications where power consumption is a critical concern. Moreover, SC-FDE allows a much simpler receiver structure and possibly lower sampling rate than DS-UWB, where the high sampling rate analog-to-digital converter (ADC) might be too costly, if pos-

sible, for the current CMOS technology. Despite the many favorable properties suitable for high speed, low-cost and low-power transmission, SC-FDE has rarely been investigated for UWB communications.

In this thesis, we propose SC-FDE as an alternative physical layer solution for UWB communications and present a comprehensive investigation of the SC-FDE system over IEEE 802.15.3a UWB channels. We first study the performance of the proposed SC-FDE UWB communications and compare that with single user OFDM-UWB and single carrier impulse radio (IR) UWB using time-domain equalization and rake reception. We demonstrate the superiority of SC-FDE over UWB communications in terms of performance and implementation complexity over both IR-UWB and OFDM-UWB. The effects of system design parameters such as Fast Fourier Transform (FFT) size and CP length on the performance of the SC-FDE system are also investigated. This completes the basic system design. Based on the SC-FDE system model studied above, we propose novel schemes to address the channel estimation and multiple access problems for SC-FDE UWB. Further research includes the transmitted signal design to fit the FCC mask and introduce spectral nulls to limit narrowband interference (NBI) in UWB communications. Moreover, the effects of channel estimation errors, carrier frequency offset and sampling timing offset on the performance of SC-FDE UWB are also investigated.

1.4 Thesis Outline

The thesis is organized as follows.

Chapter 2 describes the SC-FDE system model and proposes SC-FDE as an alternative physical layer solution for IEEE 802.15.3a UWB communications. The performance of SC-FDE over IEEE 802.15.3a UWB channel models is analyzed, simulated and compared with that of OFDM-UWB and IR-UWB using time domain equalization and rake reception. The impact of channel coding on the performance of SC-FDE and OFDM in UWB is also studied and compared. Our results demonstrate performance advantage of the

SC-FDE system, especially when implementation issues such as low complexity and low power consumption for UWB are taken into account. The performance of SC-FDE with oversampling diversity combining is also investigated.

Chapter 3 addresses the channel estimation problem for SC-FDE system over IEEE 802.15.3a UWB channels. A lower bound of the mean-squared error (MSE) value for the frequency-domain linear minimum-mean-squared-error (LMMSE) channel estimator is derived and the optimal pilot sequence that achieves this lower bound is obtained. Further simplification leads to reduced computational complexity. Our results show that the proposed low complexity estimator performs well under UWB channels CM1-CM4 with performance degradation less than 1 dB compared to perfect channel estimation.

Chapter 4 proposes a time division multiple access (TDMA) scheme for the BPSK modulated SC-FDE over IEEE 802.15.3a UWB channels. The transmitter and receiver matrices for the proposed TDMA SC-FDE system are derived to achieve the multiple access interference (MAI) free and inter-block interference (IBI) free transmission without the insertion of CP between blocks, thus avoiding long CP and large FFT size in high speed UWB communications. The performance of the proposed TDMA SC-FDE system over UWB channels is investigated and compared with that of the block spreading CDMA scheme. The impact of oversampling diversity and imperfect channel estimation on the performance of the proposed system are also investigated. Results show that the proposed TDMA scheme can effectively eliminate the error floor in CDMA due to insufficient CP, and it is more efficient to accommodate larger number of users than CDMA in high data rate transmission.

Chapter 5 investigates spectrum shaping in UWB communications in order to introduce spectral nulls to limit interference with narrowband signals. Each transmitted symbol is represented by a " coded Gaussian monocycle pulse" in which Gaussian monocycles are weighted, delayed and summed in accordance with a designed codeword. The use of the Gaussian monocycle ensures that the UWB spectrum mask established by the FCC is met, and the codeword is designed to generate a spectral null at the frequency or frequen-

cies being used by existing narrowband devices. Signals obtained with different spectrum shapings (e.g., Butterworth, Chebyshev, elliptical) and by introducing nulls at multiple interference frequency bands are discussed. This approach can be used in various systems; as one application, we simulate the performance of a coded monocycle UWB system with a spectral null in the presence of NBI using SC-FDE, and compare its performance with that of an uncoded SC-FDE UWB system using a single Gaussian monocycle. Our results show that NBI can be effectively suppressed by transmitting and matched filtering the pulse with a spectral null at the interference frequency, therefore improving the robustness of UWB systems to NBI.

Chapter 6 investigated the performance of SC-FDE over UWB communications with channel estimation error. The probability density functions (PDF) of the frequency-domain MMSE equalizer taps are derived in closed form. The error probabilities of single carrier block transmission with frequency-domain MMSE equalization under imperfect channel estimation are presented and evaluated numerically. Compared with the simulation results, our semi-analytical analysis yields fairly accurate bit error rate (BER), thus validating the use of the Gaussian approximation method in the performance analysis of the SC-FDE system with channel estimation error.

Chapter 7 investigates the effect of carrier frequency offset (CFO) and sampling timing offset (STO) on the performance of SC-FDE over UWB channels. Signal-to-interference-plus-noise ratio (SINR) of SC-FDE UWB in the presence of CFO is analyzed and compared with that of OFDM. We also study the effect of a constant STO on the performance of SC-FDE. Two forms of STO are considered, i.e., a shifted sampling timing point other than the optimal timing point and a distorted sampling rate other than the symbol rate. Our results show that the performance of SC-FDE is rather channel dependent when sampling at a non-optimal time instant within one symbol duration, and the energy of the sampled equivalent channel at the sampling point determines its BER performance. Moreover, an SC-FDE system is fairly sensitive to a distorted sampling rate at the receiver, where severe performance degradation can occur due to the mismatched sampling rate at the transmitter

and receiver. The BER performance of SC-FDE in the presence of a constant STO is simulated and compared with that of OFDM-UWB. Moreover, timing jitter that is modeled as a uniformly distributed random timing error, is also simulated for SC-FDE and OFDM over UWB channels.

Chapter 8 concludes the thesis and proposes future work.

1.5 Contributions

The primary contribution of this thesis is to study the performance and transceiver design of SC-FDE over UWB communication channels, which could possibly be a better option for the high data rate, low complexity IEEE 802.15.3a UWB systems.

In addition to the system study, we investigated the channel estimation, multiple access and pulse shaping design for SC-FDE UWB. We also did performance analysis of SC-FDE UWB with channel estimation errors and carrier frequency offset and sampling timing offset.

Based on these work, 6 journal papers are published, to appear, or submitted. We also have 6 conference papers published and one patent filed.

1.6 Notation

Notation: Bold upper case and lower case letters denote matrices and column vectors, respectively; $(\cdot)^T$, $(\cdot)^H$ and $(\cdot)^{-1}$ denote matrix transpose, Hermitian transpose and matrix inverse respectively. We use $\mathbb{M}_N$ for the set of N by N matrices and $\mathbf{I}_N$ for an $N \times N$ identity matrix. Moreover, $(\cdot)_{ij}$ denotes the (i,j)-th entry of a matrix, $\mathbb{T}\mathrm{r}\{\cdot\}$ denotes the trace of an $N \times N$ matrix, $\det(\cdot)$ denotes the determinant of a matrix and $(\cdot)^*$ denotes the complex conjugate. Furthermore, $\mathbb{E}$ denotes expectation, $\otimes$ stands for Kronecker's product, $\mathrm{Re}\{\cdot\}$ denotes the real part and $\mathrm{sgn}(\cdot)$ is the element-wise algebraic sign function.

Chapter 2

Cyclic Prefixed Single Carrier Transmission in Ultra-wideband Communications

2.1 SC-FDE System Model and Performance Analysis

We consider the cyclic prefixed single carrier block transmission with frequency-domain equalization over UWB channels. The system model of an SC-FDE system over UWB channels is illustrated in Fig. 2.1, where a block of signals $\mathbf{x} = [x_0, x_1, \cdots, x_{N-1}]^T$ is transmitted with block length N. CP is inserted between blocks to eliminate IBI. As long as the CP duration is longer than that of the channel impulse response, IBI effects can be ignored. The same block can be transmitted more than once to increase the received signal to noise ratio (SNR) or one symbol in a block can be repeated several times.

Suppose that the equivalent symbol spaced channel impulse response is of order L with taps $\mathbf{h} = [h(0), \cdots, h(L-1)]^T$. Assuming timing is acquired, the received signal $\mathbf{y}$ after removing CP can be expressed in a matrix form as [16]

$$\mathbf{y} = \tilde{\mathbf{H}}\mathbf{x} + \mathbf{n} \tag{2.1}$$

where $\tilde{\mathbf{H}}$ is the circulant Toeplitz matrix with the first column being $\mathbf{h}$ zero padded to length N [16]. Each element in the noise vector $\mathbf{n}$ is a real Gaussian random variable (RV) with

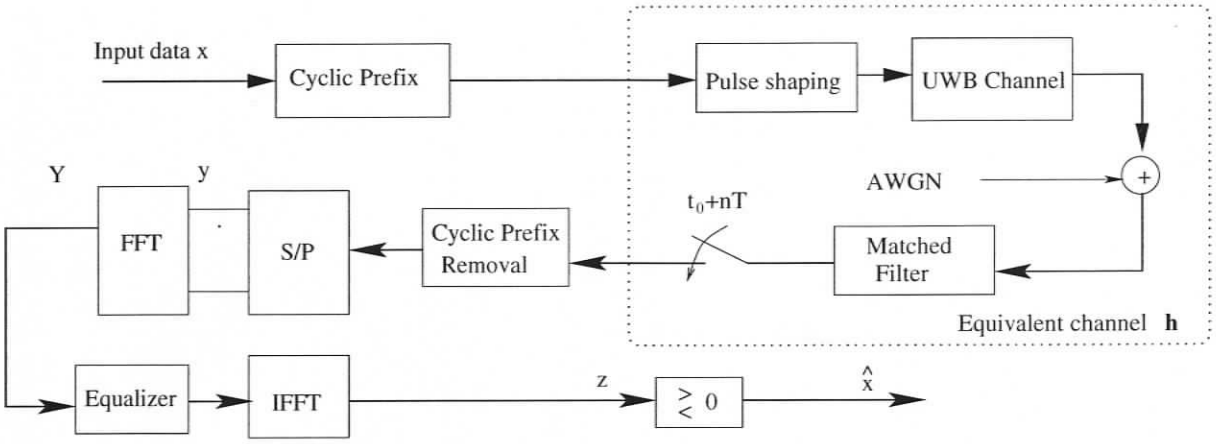

Figure 2.1. *SC-FDE System Model*

variance $\frac{N_0}{2}$, where N_0 is the one-sided noise power spectral density. At the receiver, after serial-to-parallel (S/P) transform, the sampled received signal is converted to the frequency domain by the FFT operator, followed by the frequency-domain MMSE equalization, with equalizer taps given by [11]

$$C_k = \frac{H_k^*}{|H_k|^2 + N_0/(2E_b)} \tag{2.2}$$

where E_b is the energy per transmitted bit and $H_k = \sum_{n=0}^{N-1} h_n e^{-j\frac{2\pi}{N}nk}$ is the kth attenuation factor of the channel impulse response. After frequency-domain equalization and IFFT, signal detection is performed in the time domain. For simplicity and without loss of generality, we consider BPSK modulation and the decision variable becomes $\hat{\mathbf{x}} = \text{sgn}(\mathbf{z})$, where $\mathbf{z}$ is the signal vector after the frequency-domain equalization and IFFT.

Next, we analyze the performance of the BPSK modulated SC-FDE over UWB channels, based on the assumption that the CP duration is long enough to eliminate IBI. It is known that the circulant matrix $\tilde{\mathbf{H}}$ can be decomposed as [16]

$$\tilde{\mathbf{H}} = \mathbf{F}^H \Lambda \mathbf{F} \tag{2.3}$$

where $\mathbf{F}$ is the FFT matrix with $F_{lk} = \frac{1}{\sqrt{N}} \exp\left(-j\frac{2\pi lk}{N}\right)$, $0 \le l,k \le N-1$. Moreover, Λ is a diagonal matrix with its kth diagonal element being H_k. The received time-domain signal

$\mathbf{y}$ is then transformed to the frequency domain as

$$\mathbf{Y} = \mathbf{F}\mathbf{y} = \Lambda\mathbf{F}\mathbf{x} + \mathbf{F}\mathbf{n}. \tag{2.4}$$

After equalization and IFFT, the received signal $\mathbf{z}$ becomes

$$\mathbf{z} = \mathbf{F}^H\mathbf{C}\mathbf{Y} = \mathbf{F}^H\mathbf{C}\Lambda\mathbf{F}\mathbf{x} + \mathbf{F}^H\mathbf{C}\mathbf{F}\mathbf{n} \tag{2.5}$$

where $\mathbf{C}$ is an $N \times N$ diagonal matrix with its kth diagonal element as the frequency-domain equalizer taps C_k, for $k = 0, 1, \cdots, N-1$. To analyze bit error rate, we will, without loss of generality, consider the detection of bit x_0. The corresponding z_0 given by (2.5) can be expressed as

$$z_0 = \frac{1}{N}\sum_{k=0}^{N-1}\eta_k x_0 + \frac{1}{N}\sum_{l=1}^{N-1}\left(\sum_{k=0}^{N-1}\eta_k e^{-j\frac{2\pi}{N}lk}\right)x_l + \tilde{n} \tag{2.6}$$

where

$$\eta_k = \frac{|H_k|^2}{|H_k|^2 + N_0/(2E_b)} \tag{2.7}$$

and

$$\tilde{n} = \frac{1}{N}\sum_{l=0}^{N-1}\left(\sum_{k=0}^{N-1}e^{-j\frac{2\pi}{N}lk}C_k\right)n_l \tag{2.8}$$

with n_l being the lth element in $\mathbf{n}$, and $\tilde{n}$ is the real Gaussian noise after equalization and IFFT with variance

$$\sigma_n^2 = \mathbb{E}[|\tilde{n}|^2] = \frac{N_0}{2N^2}\sum_{l=0}^{N-1}\left|\sum_{k=0}^{N-1}C_k e^{-j\frac{2\pi}{N}lk}\right|^2. \tag{2.9}$$

The MMSE receiver is not ISI free, where the second term in (2.6) is the interference. Denote $S_l = \frac{1}{N}\sum_{k=0}^{N-1}\eta_k e^{-j\frac{2\pi}{N}lk}$. It follows that

$$z_0 = \frac{1}{N}\sum_{k=0}^{N-1}\eta_k x_0 + I + \tilde{n} \tag{2.10}$$

where I is the residual ISI term and $I = \sum_{l=1}^{N-1}S_l x_l$. Conditional on I and the channel impulse response $\mathbf{h}$, the probability of error for SC-FDE is given by

$$\mathrm{P}_{MMSE}(e|\mathbf{h}, I) = \Pr(z_0 > 0 | x_0 = -1, \mathbf{h}) = Q\left(\frac{\frac{1}{N}\sum_{k=0}^{N-1}\eta_k - I}{\sigma_n}\right) \tag{2.11}$$

where $Q(\cdot)$ is the Gaussian tail function. Using the techniques in [17], the probability of error unconditioned from I can then be obtained as

$$\begin{aligned} P_{MMSE}(e|\mathbf{h}) &= \frac{1}{2} - \frac{2}{\pi} \sum_{\substack{m=1 \\ m\,odd}}^{M} \left[\frac{\exp(-m^2\omega^2/2)\sin(m\omega g_0)}{m} \right. \\ &\quad \left. \prod_{l=1}^{N-1} \cos(m\omega g_l) \right] + \alpha + \beta \end{aligned} \tag{2.12}$$

where $\omega = \frac{2\pi}{T_1}$, $g_0 = \frac{\frac{1}{N}\sum_{k=0}^{N-1}\eta_k}{\sigma_n}$ and $g_l = \frac{S_l}{\sigma_n}$. Also, α and β represent the approximation error and truncation error. The BER calculated from (2.12) can approach the exact value as accurately as desired by adjusting M and T_1. Alternatively, using the Gaussian approximation for the residual ISI term I, we have

$$\tilde{P}_{MMSE}(e|\mathbf{h}) = Q\left(\frac{\frac{1}{N}\sum_{k=0}^{N-1}\eta_k}{\sqrt{E_b \sum_{l=1}^{N-1} |S_l|^2 + \sigma_n^2}} \right). \tag{2.13}$$

Our calculation using Gaussian approximation in (2.13) for ISI matches (2.12) very well, in agreement with the Gaussianity of MAI analyzed in [18], [19]. The unconditional probability of error for SC-FDE is then obtained by averaging over various UWB channel realizations of a particular channel model.

2.2 Simulation Results and Discussions

2.2.1 Performance Comparison of SC-FDE, IR-UWB and OFDM-UWB

The performance of the MMSE based SC-FDE over UWB channels is evaluated using the formulas derived in the previous section and compared with the performance of OFDM-UWB and IR-UWB employing rake receiver and time-domain MMSE equalization. Simulation is carried out assuming perfect channel state information (CSI) available at the receiver, due to the slow time-varying nature of the UWB channel. The UWB channels used are CM1-CM4 models proposed by the IEEE 802.15.3a Working Group [2], where the channel RMS delay spread ranges from around 5 ns to 25 ns. In all simulations, the

transmitter pulse shaping filter, the receiver matched filter and one of the 100 channel realizations for a particular UWB channel model are convolved and sampled to form 100 different equivalent channel realizations over which the BERs are averaged. For fair comparison, we evaluate the performance of three systems at the same effective system data rate of 400 Mbps. For both SC-FDE and OFDM-UWB, we use a data block length $N = 256$, CP length of 64, symbol duration of 2 ns and the root raised cosine (RRC) pulse with roll off factor of 0.5. For the IR-UWB, the performance is simulated using a 2.5 ns symbol duration with a 0.5 ns long the second derivative of a Gaussian pulse $p(t) = (1 - 4\pi(t/\tau)^2)e^{-2\pi(t/\tau)^2}$, where $\tau = 0.18$ ns. The oversampling factor 16 of the 0.5 ns pulse is used to perform rake reception, where the maximal ratio combining is utilized, with 10 rake fingers for CM1-CM3 [8] and 20 rake fingers for CM4, and different number of equalizer taps (10 for CM1 and CM2, 20 for CM3 and 30 for CM4). These parameters are chosen as a performance/complexity tradeoff where the investigated system can yield reasonable performance with comparable (if not favors IR-UWB) complexity. Complexity issues will be detailed in Section 2.2.4.

Figs. 2.2 and 2.3 show the performance comparison of IR-UWB, OFDM-UWB, and SC-FDE under UWB channel models CM1-CM4. It can be observed that SC-FDE substantially outperforms OFDM-UWB for each channel model. The reason lies in the fact that for single carrier transmission, the energy of an individual bit is distributed over the whole available frequency spectrum and therefore already enjoys frequency diversity [12]. In OFDM-UWB, however, the receiver decisions are made independently on each sub-carrier, the detection of data symbols on the subcarriers with spectral nulls will be unreliable and dominate the performance degradation [12], which can be compensated by effective coding schemes as in Section 2.2.2. Comparing the IR-UWB and SC-FDE, an IR-UWB system with 10 rake fingers and 10 time-domain MMSE equalizer taps outperforms SC-FDE under CM1, where the small number of multipaths (10 major paths and maximum 60 resolvable paths) and the line-of-sight (LOS) channel condition validate the use of rake reception and eliminates the ISI, while SC-FDE in CM1 still suffer from the ISI effect. However, the ad-

vantage of IR-UWB diminishes for CM2-CM4 when the channel condition becomes worse (i.e., the maximal number of resolvable paths increases to 120-300 for CM2-CM4 with 12-50 major paths for a 0.5 ns pulse) where the number of rake fingers and time domain equalizer taps are not sufficient to gather enough channel energy or to combat ISI, while the performance of SC-FDE does not vary much from CM1 and SC-FDE outperforms the IR-UWB even though a larger number of time-domain equalizer taps and rake fingers are used for IR-UWB. For instance, IR-UWB yields inferior performance to SC-FDE even when 20 rake fingers and 30 time-domain equalizer taps are utilized for CM4, as in Fig. 2.2. Increasing the number of rake fingers will lead to improved BER performance, yet at the expense of high implementation complexity, as will be illustrated in 2.2.4.

2.2.2 Impact of Channel Coding

The convolutional codes of rate $R = 1/3$ with generator polynomial $g_0 = 133_8, g_1 = 145_8, g_2 = 175_8$, and rate $R = 1/2$ with polynomial $g_0 = 133_8, g_1 = 171_8$ are used as an example to compare the performance of coded OFDM-UWB and SC-FDE UWB. Both of the rate $1/2$ and $1/3$ convolutional codes have a constraint length of 7. For simplicity purpose, equalization and decoding are completely separated in the design. The receiver employs Viterbi algorithm to perform maximum-likelihood decoding of the coded symbol block by block. For single carrier transmission, the soft-decision metric, or the Euclidean distance between a block of the received signal and the transmitted data is given by

$$D = \|\mathbf{z} - \mathbf{x}\|^2 = \sum_{k=0}^{N-1} |z_k - x_k|^2 \tag{2.14}$$

where $\mathbf{z}$ is the equalized signal sequence. The Viterbi decoder then searches through the trellis to find the maximum likelihood path with the smallest metric and performs decoding [20].

In the case of coded OFDM, however, channel state information should be included in the metrics computation to yield a good performance [11]. It is well known that a received

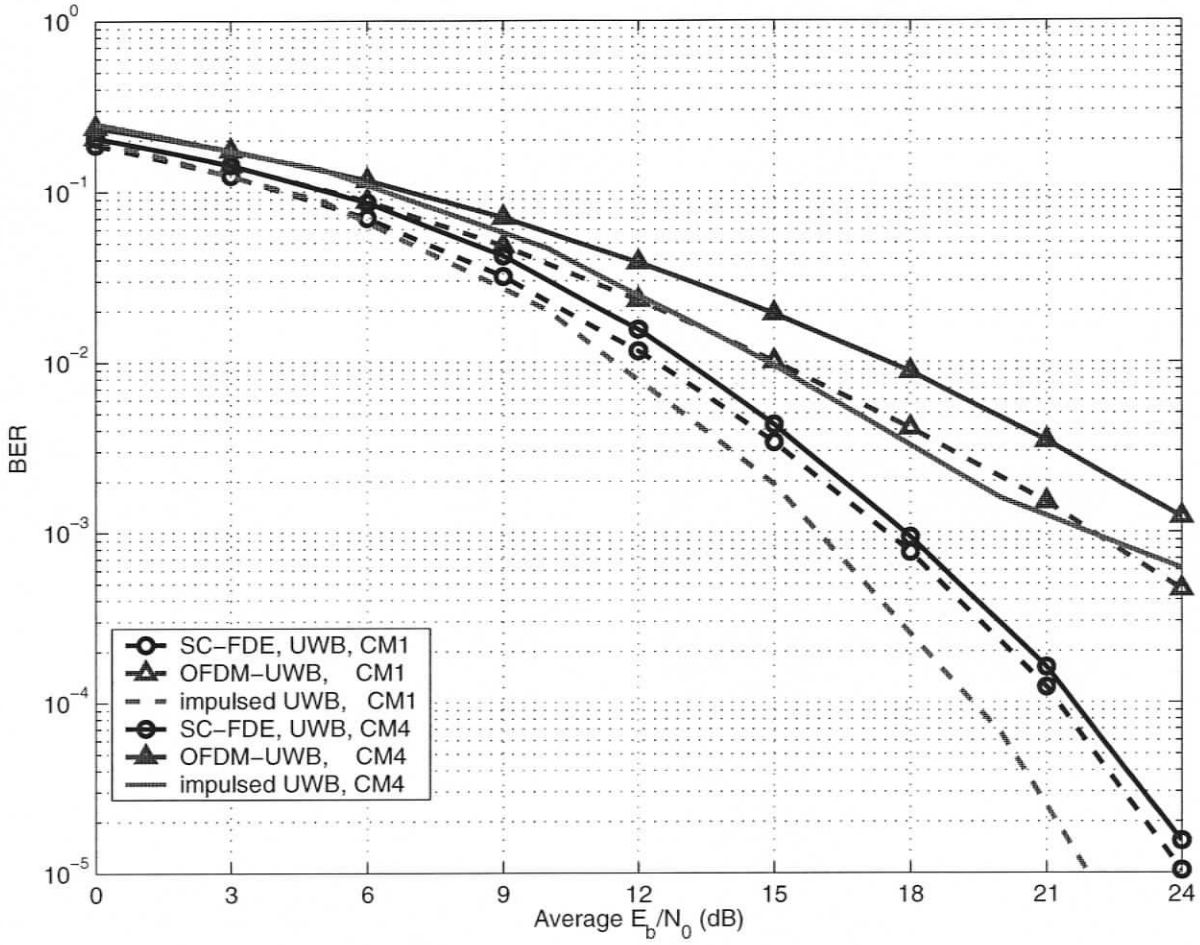

Figure 2.2. *Performance comparison of SC-FDE, OFDM-UWB, and IR-UWB under the UWB channel CM1 and CM4. IR-UWB uses 10 rake fingers, 10 equalizer taps for CM1 and 20 rake fingers, 30 equalizer taps for CM4.*

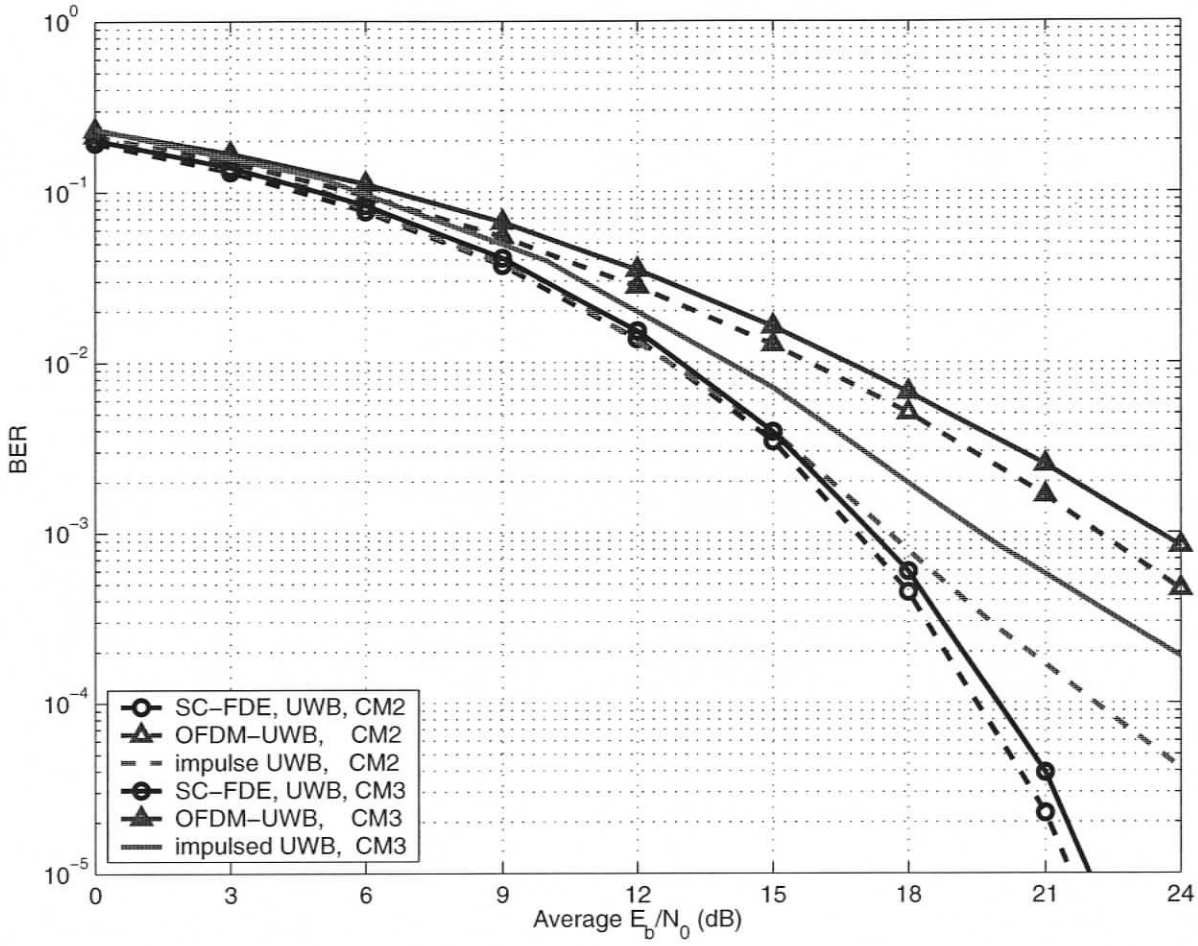

Figure 2.3. *Performance comparison of SC-FDE, OFDM-UWB, and IR-UWB under the UWB channel CM2 and CM3. IR-UWB uses 10 rake fingers, 10 equalizer taps for CM2 and 20 equalizer taps for CM3.*

OFDM signal before equalization can be expressed as

$$y_k = H_k x_k + n_k \tag{2.15}$$

where x_k is the $k\text{-}th$ bit of the transmitted signal in one DFT block, H_k is the $k\text{-}th$ DFT coefficient of channel impulse response $\mathbf{h}$ and y_k is the $k\text{-}th$ received bit of the unequalized signal. The $k\text{-}th$ bit of the equalized sequence $\mathbf{z}$ is $z_k = y_k/H_k = x_k + v_k$, where v_k is the Gaussian noise with variance $\sigma_{v_k}^2 = \frac{N_0}{2|H_k|^2}$. The log-likelihood function for one transmitted block can be written as

$$\begin{aligned}
\ln \Pr(\mathbf{z}|\mathbf{x}) &= \sum_{k=0}^{N-1} \ln \Pr(z_k|x_k) \\
&= \sum_{k=0}^{N-1} \ln \left[\frac{1}{\sqrt{2\pi\sigma_{v_k}^2}} \exp\left(-\frac{|z_k - x_k|^2}{2\sigma_{v_k}^2} \right) \right] \\
&= \sum_{k=0}^{N-1} \ln \frac{|H_k|}{\sqrt{\pi N_0}} - \frac{1}{N_0} \sum_{k=0}^{N-1} |H_k|^2 |z_k - x_k|^2.
\end{aligned} \tag{2.16}$$

To maximize the log-likelihood function $\ln \Pr(\mathbf{z}|\mathbf{x})$ is equivalent to minimizing the second term in (2.16). Denoting $\mathrm{CSI}_k = |H_k|^2$ as the channel attenuation parameter for each subcarrier, the soft-decision metric in the weighted decoding algorithm can be obtained as

$$D' = \sum_{k=0}^{N-1} \mathrm{CSI}_k |z_k - x_k|^2 \tag{2.17}$$

which is in accordance with the results in [11]. The decoder searches the maximum likelihood path with the smallest weighted metric through the trellis and performs decoding. Since unreliable detection due to a severe channel attenuation on a particular subcarrier can be compensated by the weighted CSI, an improved coding gain for OFDM will be realized compared to using the Euclidean distance metric (2.14).

Performance comparisons between the coded SC-FDE and OFDM over UWB channels with different code rates are shown in Figs. 2.4-2.7. It can be observed that both OFDM and SC-FDE with channel coding achieve a significant performance gain over the uncoded systems. In the case of a coding rate of 1/3 under CM1 and CM3, the performance of coded

OFDM-UWB slightly outperforms coded SC-FDE (approximately 1 dB for CM1 and 0.5 dB for CM3 at 10^{-5}), while perfect channel state information is assumed in the decoding metric of OFDM-UWB. The gap between coded SC-FDE and OFDM-UWB diminishes when the code rate increases to 1/2, where the performance of SC-FDE is slightly better than OFDM at high SNRs. Since unreliable detection due to a severe channel attenuation on a particular subcarrier can be compensated by the weighted CSI, an improved coding gain for OFDM will be realized.

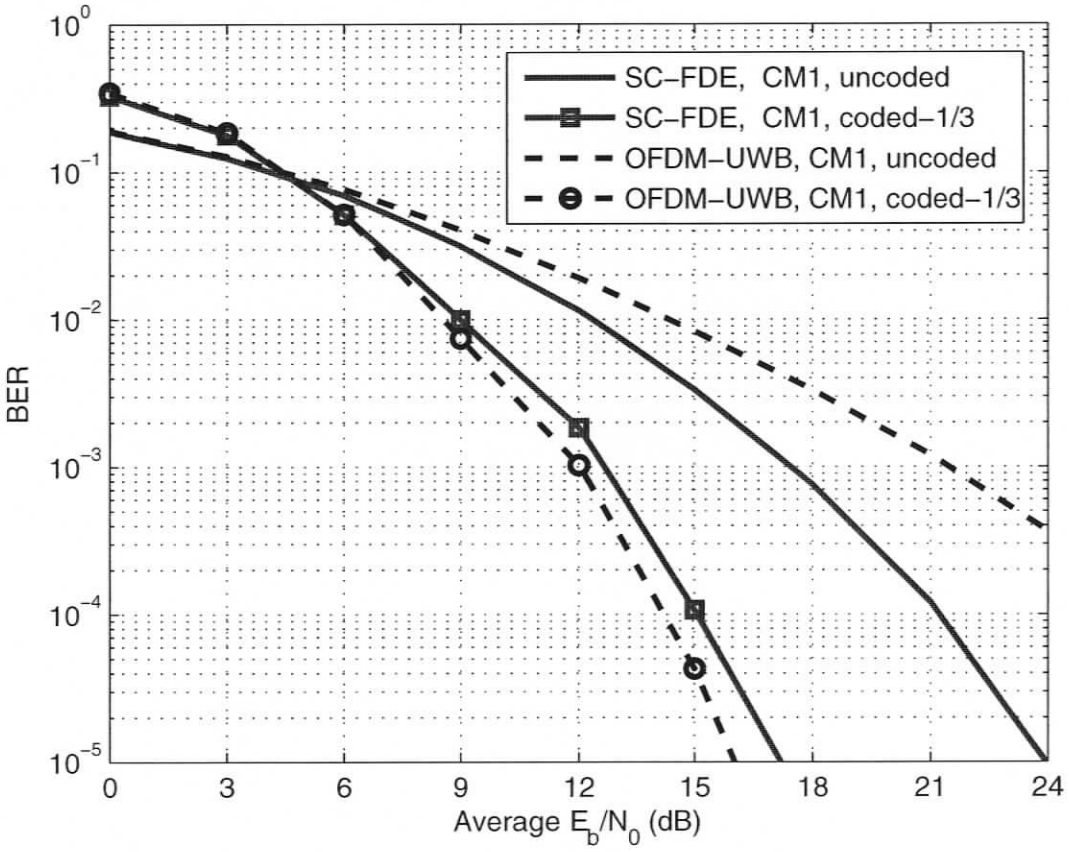

Figure 2.4. *Performance of coded OFDM and SC-FDE under the UWB channel CM1 with code rate 1/3, FFT size of 256, CP length of 64.*

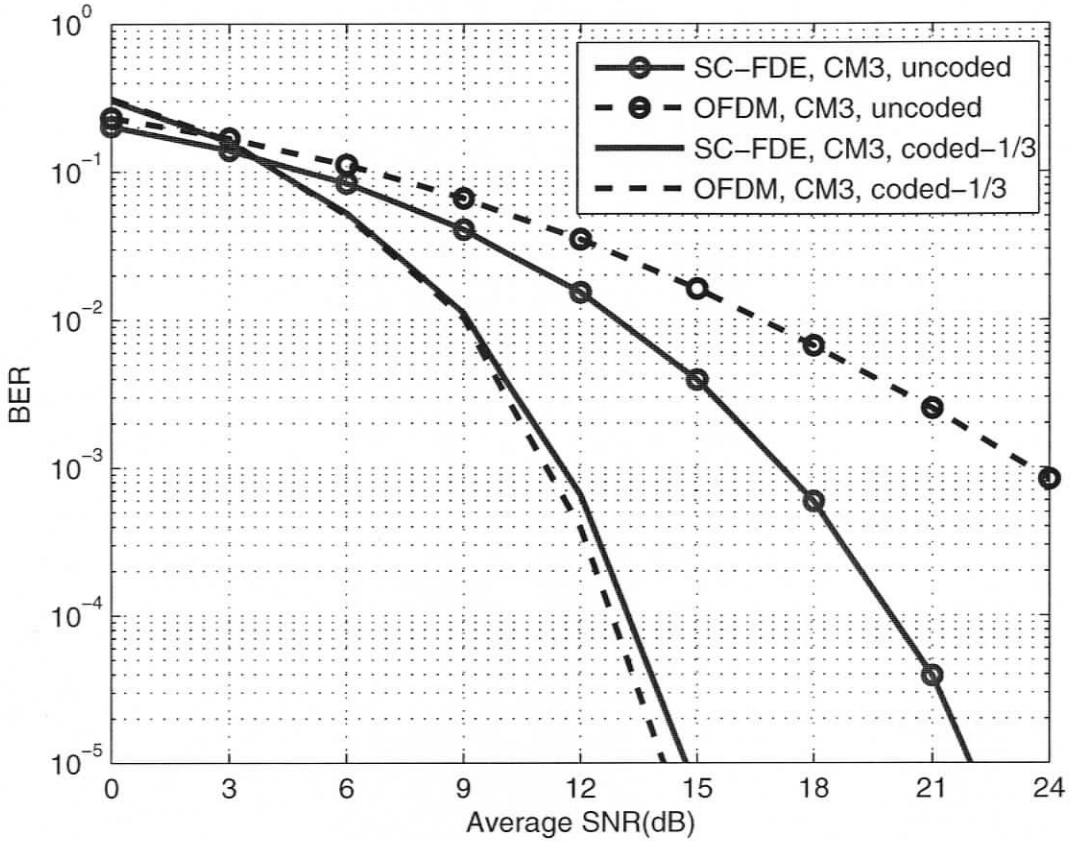

Figure 2.5. *Performance of coded OFDM and SC-FDE under the UWB channel CM3 with code rate 1/3, FFT size of 256, CP length of 64.*

2.2.3 Impact of CP length and FFT size

The results for SC-FDE and OFDM presented so far are based on the FFT size of 256 and CP length of 64, achieving a system data rate of 400 Mbps. Our study shows that the same error performance can be obtained by employing a 128 point FFT with 32 CP for UWB channels CM1 and CM2 at data rates up to 400 Mbps. For channel models with larger delay spread, as in CM3 and CM4, an FFT size of 128 and CP length of 32 is only sufficient to achieve a system data rate of 200 Mbps. At higher data rates, Figs. 2.8-2.9 show both OFDM-UWB and SC-FDE suffer performance degradation due to insufficient CP,

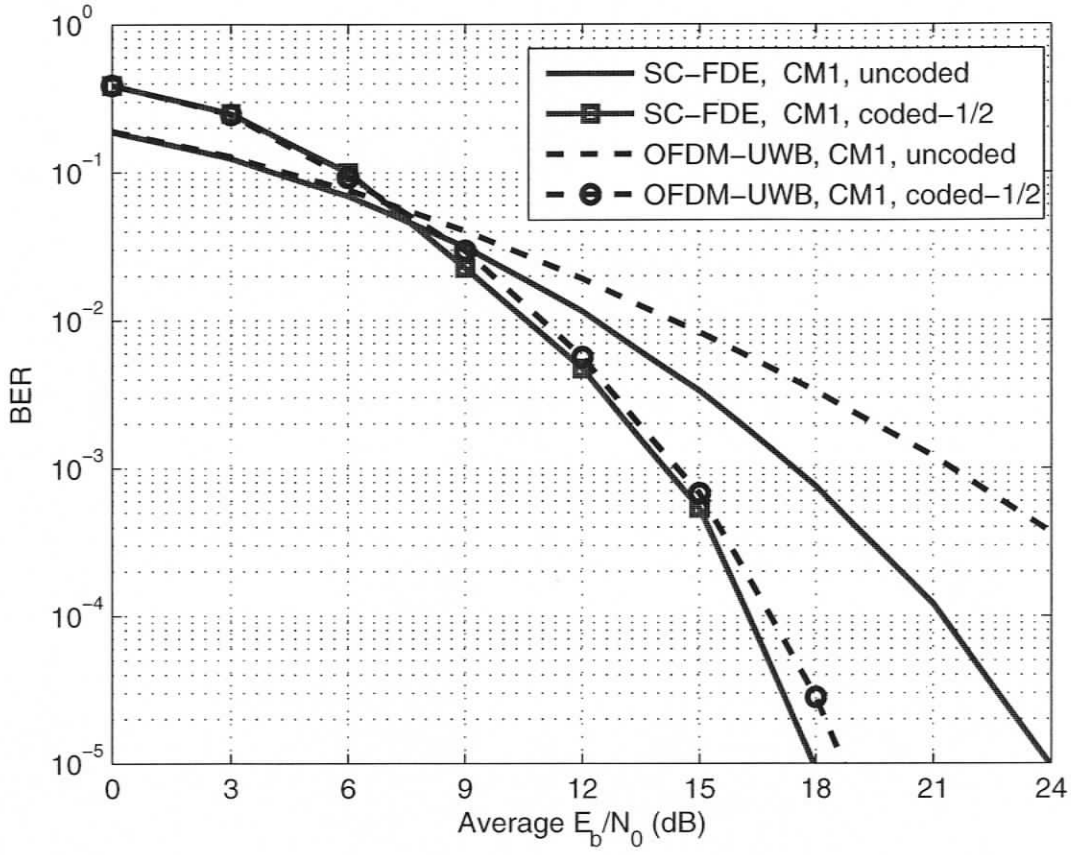

Figure 2.6. *Performance of coded OFDM and SC-FDE under the UWB channel CM1 with code rate 1/2, FFT size of 256, CP length of 64.*

with SC-FDE more sensitive to it. The reason lies in the fact that IBI primarily distorts the time-domain symbols at the beginning of each block. In SC-FDE, since detection is also performed in the time-domain, a few severely distorted time-domain symbols lead to overall substantial performance degradation. In OFDM-UWB, however, detection is performed in the frequency domain. The energy of the distortion is distributed to all subcarriers by the subsequent FFT operator, thus making the performance degradation in each subcarrier less severe. The higher sensitivity of the SC-FDE to the IBI effect, however, can be compensated by effective coding schemes. Utilizing 128 FFT/IFFT and 32 CP in a coded SC-FDE is sufficient to cover the worst UWB channel models (CM3 and CM4) at high data rates

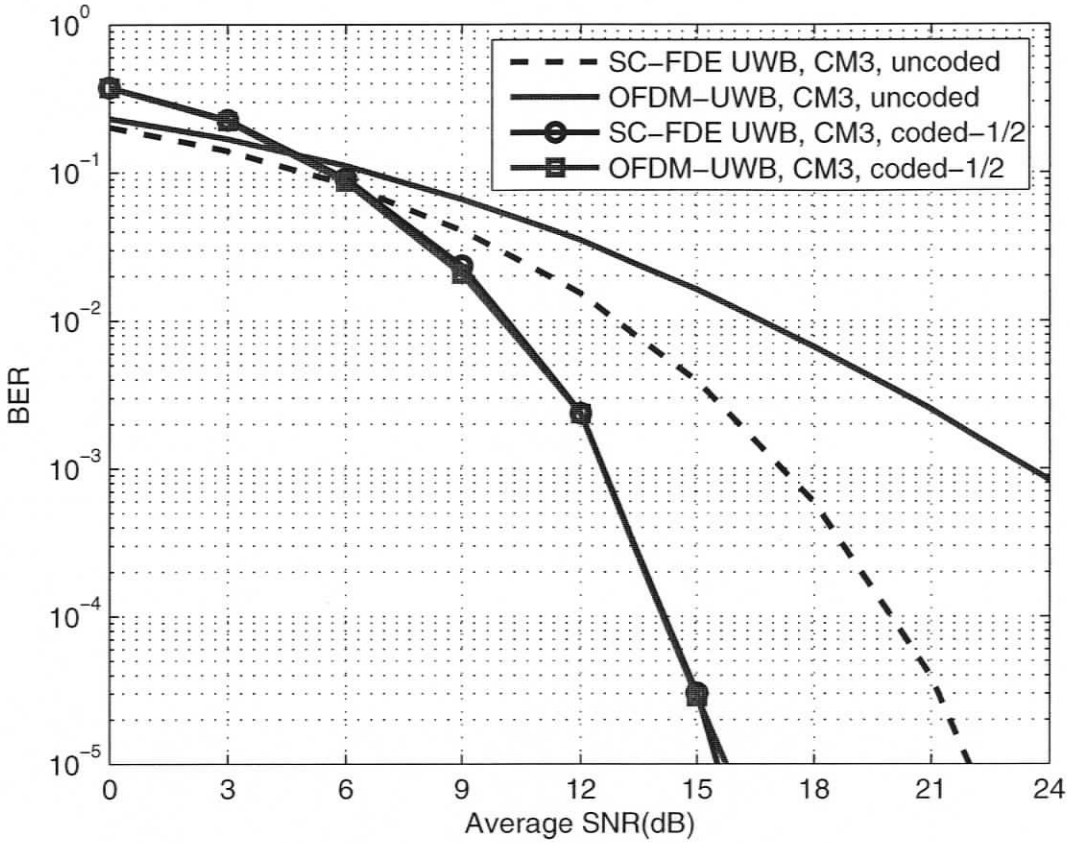

Figure 2.7. *Performance of coded OFDM and SC-FDE under the UWB channel CM3 with code rate 1/2, FFT size of 256, CP length of 64.*

and yields comparable performance to the coded OFDM-UWB.

2.2.4 Implementation Advantages of SC-FDE UWB over IR-UWB and OFDM-UWB

Compared to IR-UWB, SC-FDE has a simpler receiver structure and relatively lower power consumption. To implement L rake fingers in impulse radio, either higher sampling rate than symbol rate is required, or multiple (L) symbol rate samplers like in [8] are necessary. As in the simulation for IR-UWB when oversampling is used to perform rake reception,

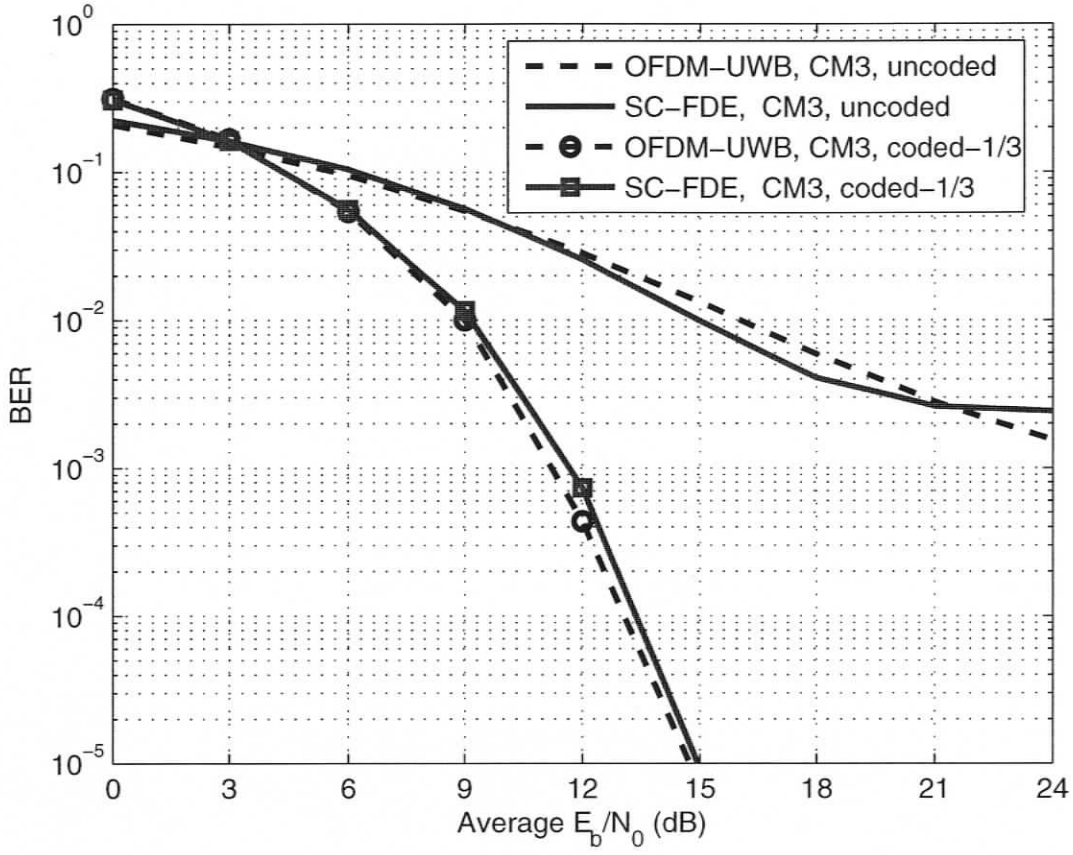

Figure 2.8. *Performance of OFDM-UWB and SC-FDE under the UWB channel CM3 with FFT size of 128 and CP length of 32, at system data rate 400 Mbps.*

32 GHz sampling rate is utilized to achieve a reasonable performance, which is too costly (if possible) for current CMOS technology, with severe power consumption issue. On the other hand, to achieve symbol rate sampling, each finger requires a high speed analog correlator and an ADC converter. Using more rake fingers to capture multipath energy increases circuit complexity, power dissipation and storage requirement. In addition, a large number of channel taps and delays has to be estimated. Moreover, severe ISI becomes the dominant detrimental factor to performance at high SNRs, especially for high data rate transmission. Substantial number of time-domain equalizer taps required in channels with large delay spread (e.g., 80 taps for CM4 at data rate of 400 Mbps) increases the com-

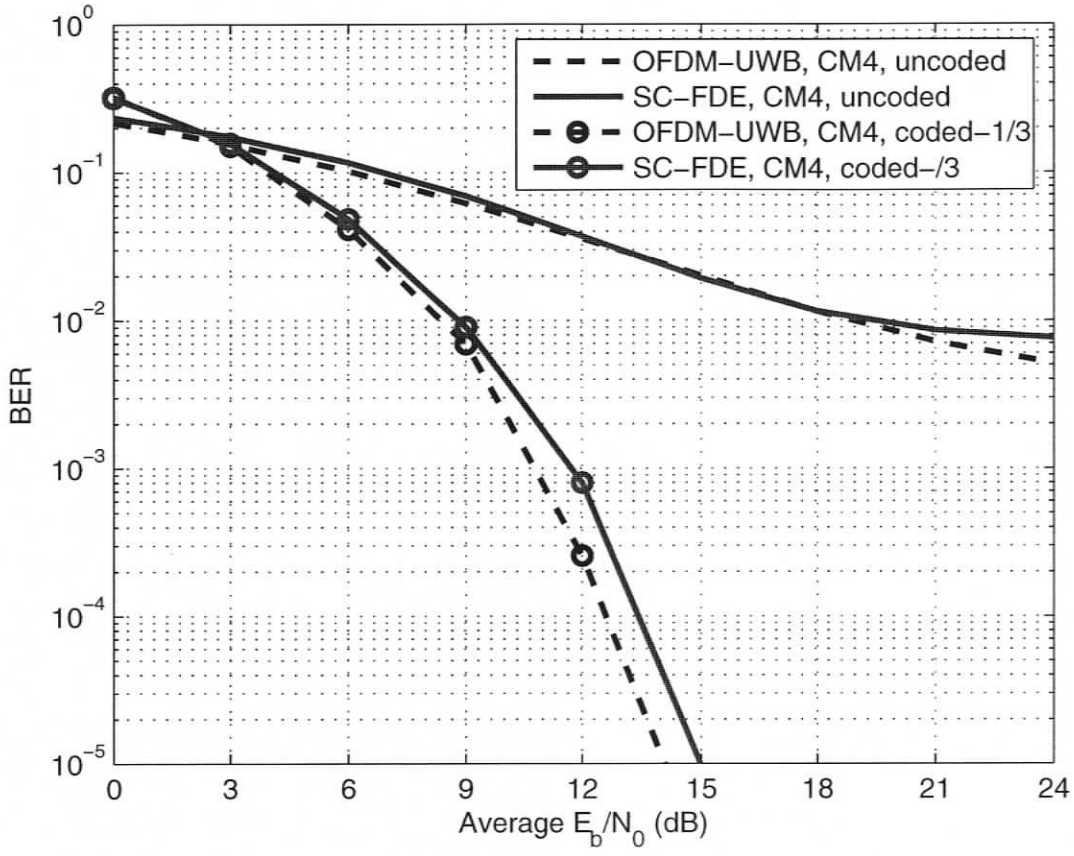

Figure 2.9. *Performance of OFDM-UWB and SC-FDE under the UWB channel CM4 with FFT size of 128 and CP length of 32, at system data rate 400 Mbps.*

plexity significantly. Assume that perfect CSI is available at the receiver. For the IR-UWB, time-domain MMSE equalization involves a $K \times K$ matrix inverse to calculate the equalizer taps, where K is the number of equalizer taps. Cholesky decomposition can be utilized to perform the matrix inverse at a reduced computational complexity at an order of K^3 multiplications [21]. As shown in Fig. 2.2, $L = 20$ rake fingers and $K = 30$ equalizer taps used for CM4 still lead to inferior performance to SC-FDE, although the receiver complexity is already very high. SC-FDE, however, yields a much lower computational complexity compared to the IR-UWB. To calculate the frequency-domain equalizer taps, N complex multiplications are required. The frequency-domain equalization performs FFT/IFFT, at

complexity of $N\log_2 N$ order of multiplications [13]. The overall computational complexity is then $N\log_2 N$ of multiplications per symbol, and is independent of the number of multipaths. Therefore, SC-FDE UWB has a lower implementation and power consumption than IR-UWB using rake receiver and time-domain equalization in very high speed UWB communications.

Compared to OFDM-UWB, SC-FDE transmission enables a similar overall complexity but solves the major implementation issue in OFDM transmitters where high PAPR values lead to significantly higher radio-frequency (RF) front-end costs and higher power consumption. As a result, SC-FDE makes it possible for a low cost, low power consumption front end device to be implemented.

2.3 SC-FDE with Diversity Combining

The simulation results in Section 2.2 are based on the assumption that the receiver matched filter output is sampled once every T interval, where T is the symbol duration. To further improve the performance of SC-FDE, diversity combining schemes can be employed by oversampling the received signal to form multiple branches. Fig. 2.10 shows the block diagram of the oversampling system which has a similar structure to the SC-FDE with spatial diversity in [22], while no multiple receiver antennas are required.

The matched filter output is oversampled at time instants $kT + t_m$, $m = 0, 1, \cdots, M-1, k = 0, 1, \cdots, N-1$ and $0 < t_m < T$. Assume timing offsets t_m's are chosen to yield the best possible performance. Multiple branches of the received signal in one symbol are hence obtained. After FFT and equalization, the signal is combined in the frequency domain as $\mathbf{u} = \frac{1}{M}\sum_{m=1}^{M} \mathbf{C}\mathbf{F}\mathbf{y}^m$ and the detection rule for BPSK signals becomes $\hat{\mathbf{x}} = \text{sgn}(\mathbf{F}^H\mathbf{u})$. Fig. 2.11 shows the performance of the SC-FDE under UWB channels with 3 branch oversampling diversity combining, using an FFT size of 256 and CP length 64. It can be observed that a 4 dB performance gain is achieved by using the oversampling diversity. Note that the additional diversity branches obtained through oversampling have decreasing

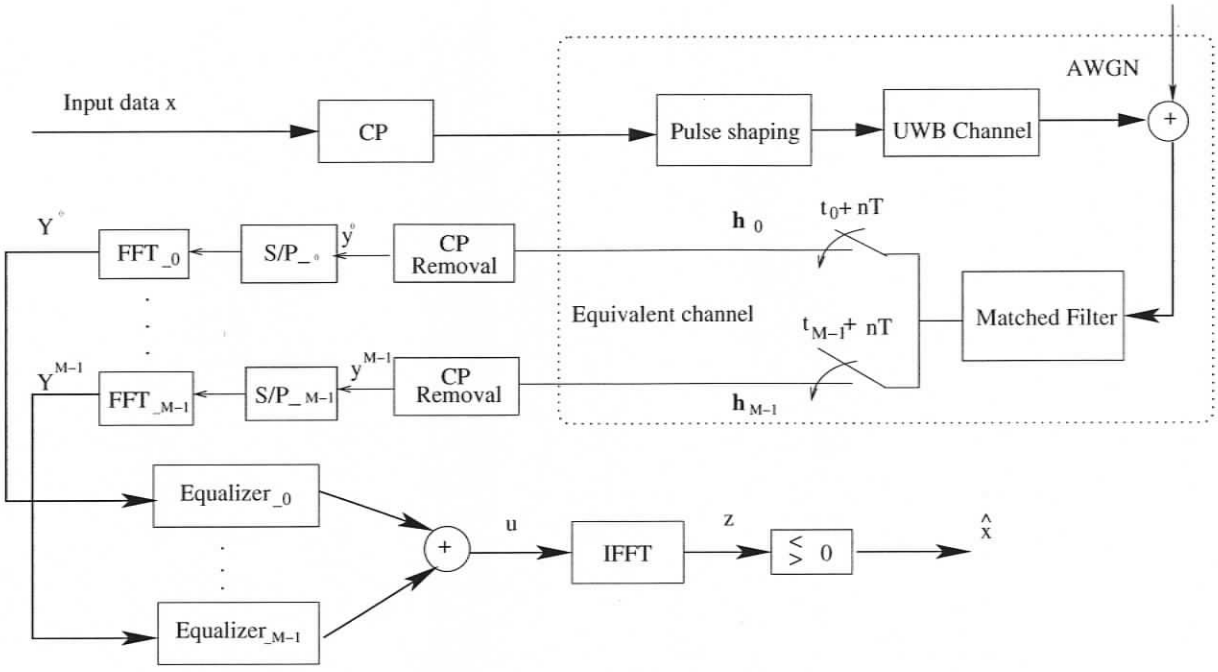

Figure 2.10. *SC-FDE system with diversity combining*

average SNR's and are not independent and identically distributed (i.i.d). Therefore the performance gain is less substantial than that having i.i.d branches as in the spatial diversity. Our results also show that using larger number of branches (say 4 branches) in the oversampling diversity scheme does not yield more performance gain than 3 branches, due to the correlation among these branches.

2.4 Summary

Cyclic prefixed single carrier block transmission with frequency-domain equalization has been proposed as an alternative physical layer technology for UWB communications. Performance wise, SC-FDE UWB achieves better performance than OFDM-UWB with no coding and comparable performance with channel coding at coding rate $1/3$ or $1/2$, and it outperforms IR-UWB in a majority of realistic UWB channels. Implementation wise, SC-FDE does not have the high PAPR issue at an OFDM transmitter and it is more effec-

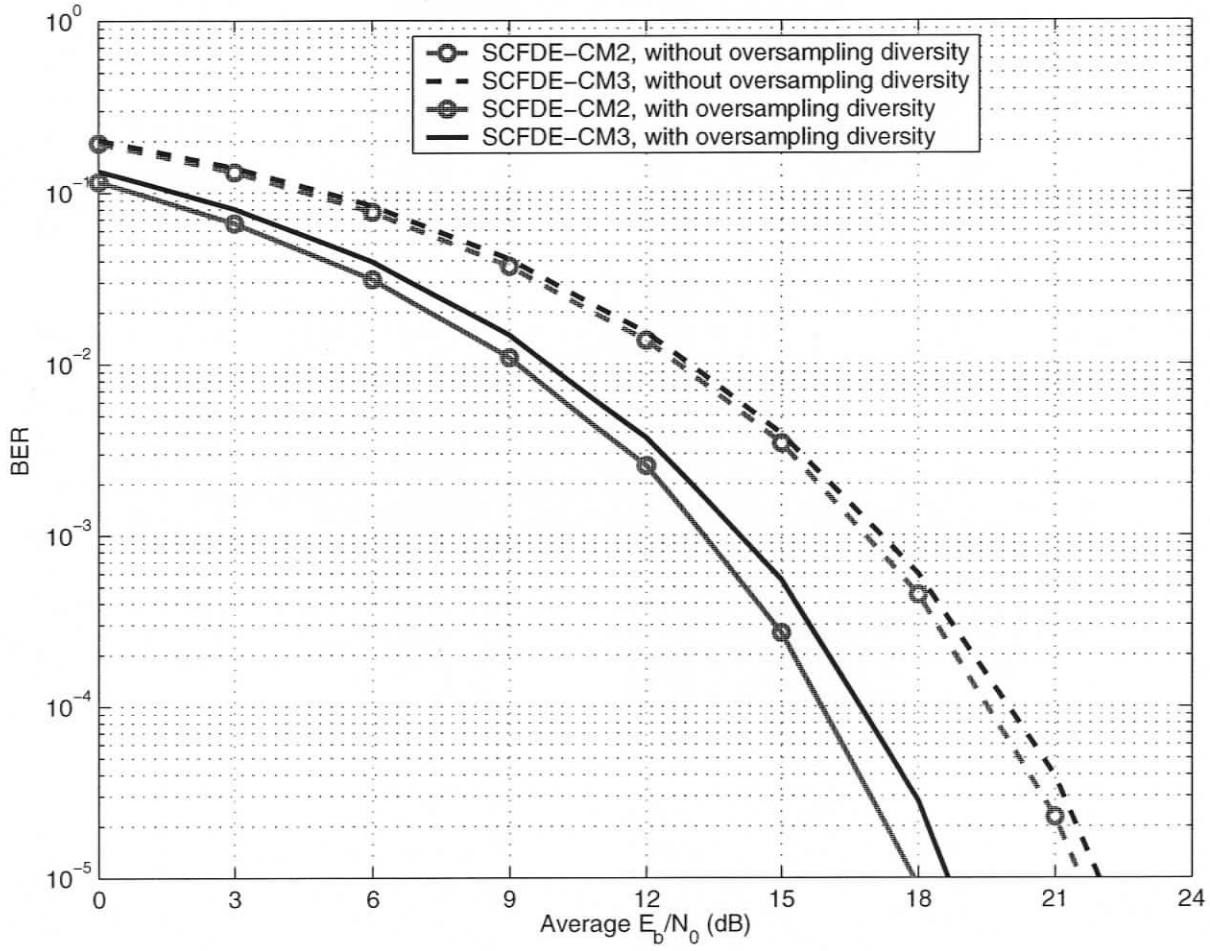

Figure 2.11. *Performance of SC-FDE with 3 diversity branches, with FFT size of 256 and CP length of 64.*

tive in collecting multipath energy and combating ISI than IR-UWB, where rake structure and time-domain equalization become too complex in the highly frequency selective UWB channels. With the overall advantages compared to IR-UWB and OFDM-UWB, SC-FDE block transmission is a promising candidate to meet the implementation requirements of high speed, low power and low cost UWB communications.

Furthermore, oversampling of the matched filter output has been investigated to increase the received SNR and a 4 dB gain has been achieved with a 3 branch combining.

Chapter 3

A Low Complexity Frequency-Domain UWB Channel Estimation for SC-FDE

3.1 Background

We presented the system model of SC-FDE over UWB channels in Chapter 2, with the assumption that perfect channel state information is available at the receiver. However, this is not the case in practical systems, where channel estimation has to be carried out with a reasonable performance and complexity. In this chapter, we address the channel estimation problem for the SC-FDE UWB systems.

UWB channel estimation is a subject of plenty research interests [8], [23]. In coherent impulse radio UWB, a large number of multipath gains and delays in the time domain have to be estimated within a short data transmission time, thus making it more difficult than in typical narrow band or wideband communications. The utilization of an SC-FDE system for UWB transmission, however, makes it possible for both the channel estimation and equalization to be carried out in the frequency domain. In [24], a channel impulse response was estimated by performing least-square (LS) channel estimation in the frequency domain followed by inverse Fourier Transform. This method produced a low complexity search strategy for optimal pilot sequences, but it was shown in [25] that it does not always result in lowest achievable MSE by the time-domain LS estimation. In [26], an LS channel estimation scheme for multiple-input multiple-output (MIMO) OFDM systems based on pilot

tones was developed and the optimal pilot sequences and optimal placement of pilot tones with respect to the MSE of LS channel estimation were derived. Two estimation schemes for OFDM, the maximum likelihood estimator (MLE) and the Bayesian minimum mean square error estimator (MMSE) estimator of the channel impulse response, were compared in [27]. Both [26] and [27] performed channel estimation in the time domain first and used FFT to obtain channel frequency response. In [28] and [29], frequency-domain channel estimators for OFDM were presented. Furthermore, a low rank channel estimator was proposed to reduce the computational complexity, which inspired our frequency-domain channel estimation schemes in this Chapter due to the similarity between OFDM and SC-FDE.

This chapter is organized as follows. In Section 3.2, an MSE lower bound for the frequency-domain LMMSE estimators is derived and the optimal pilot sequence that achieves this lower bound is obtained. Section 3.3 presents the low complexity frequency-domain channel estimator. Simulation results and discussions are presented in Section 3.4. Section 3.5 briefly summarizes this chapter.

3.2 MSE Lower Bound of the Frequency-Domain LMMSE Channel Estimator

In this chapter, we address the channel estimation scheme for SC-FDE UWB system. Fig. 3.1 shows the block diagram of the investigated SC-FDE system with frequency domain channel estimations. Supposing the symbol duration spaced equivalent channel impulse response is $\mathbf{h} = [h_0, h_1, \cdots, h_{L-1}]^T$, our objective is to estimate the kth coefficient of channel frequency response $H_k = \sum_{l=0}^{L-1} h(l) \exp(-j2\pi kl/N)$. The frequency-domain channel coefficients are estimated using pilot symbols and then utilized by the subsequent equalizer to perform frequency-domain channel equalization.

Suppose a block of pilot sequence $\mathbf{p} = [p_0, p_1, \cdots p_{N-1}]^T$, where $p_k \in \pm 1$, is transmitted

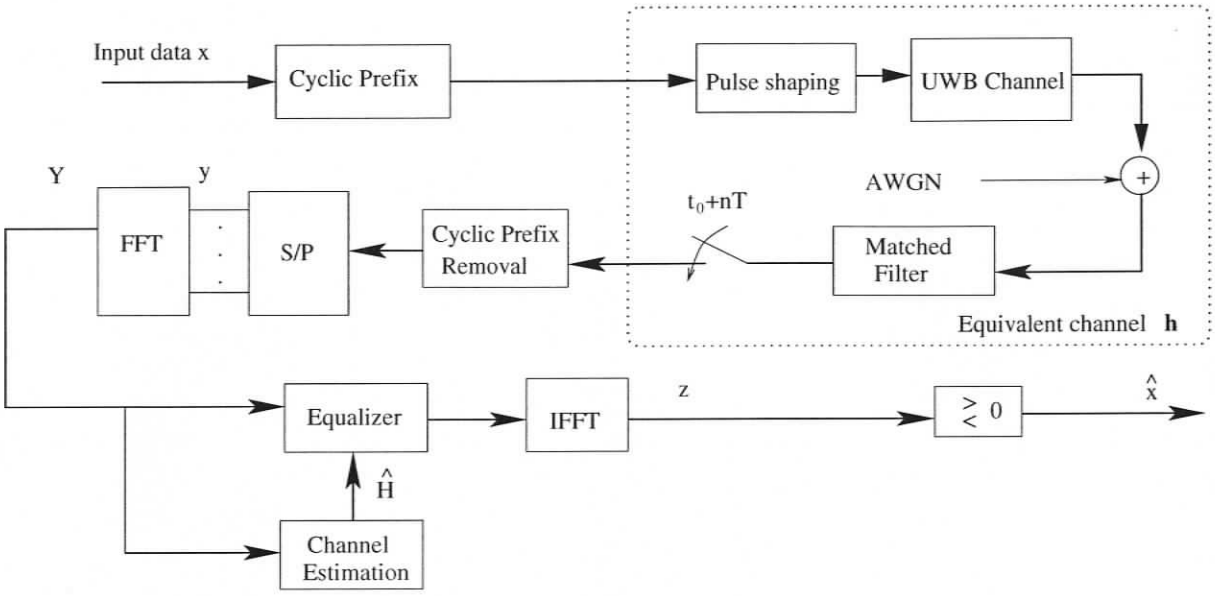

Figure 3.1. *SC-FDE system with frequency domain channel estimations*

for channel estimation purpose. By matrix manipulations, (2.4) can be rewritten as

$$\mathbf{Y} = \mathbf{PH} + \mathbf{N} \tag{3.1}$$

where $\mathbf{P}$ is a diagonal matrix with its kth diagonal element P_k as the kth coefficient of the frequency-domain spectrum of the pilot sequences $\mathbf{p}$, and $\mathbf{N} = \mathbf{Fn}$ is the Fourier Transform of the white Gaussian noise vector $\mathbf{n}$.

Our objective is to estimate the frequency-domain channel coefficients $\mathbf{H} = [H_0, \cdots, H_{N-1}]^T$, based on the received frequency-domain signal $\mathbf{Y}$. It is known that the LMMSE estimator can be expressed as [30]

$$\hat{\mathbf{H}}_{MMSE} = \mathrm{R}_{\mathbf{HY}} \mathrm{R}_{\mathbf{YY}}^{-1} \mathbf{Y} \tag{3.2}$$

where

$$\mathrm{R}_{\mathbf{HY}} = \mathbb{E}[\mathbf{H}\mathbf{Y}^H] = \mathrm{R}_{\mathbf{HH}} \mathbf{P}^H \tag{3.3}$$

and

$$\mathrm{R}_{\mathbf{YY}} = \mathbb{E}[\mathbf{Y}\mathbf{Y}^H] = \mathbf{P}\mathrm{R}_{\mathbf{HH}} \mathbf{P}^H + \sigma_n^2 \mathbf{I}_N \tag{3.4}$$

are the cross correlation matrix between $\mathbf{H}$ and $\mathbf{Y}$ and the auto-correlation matrix of $\mathbf{Y}$, respectively. Moreover, $\mathrm{R}_{\mathbf{HH}}$ is the auto-correlation matrix of channel frequency-domain response $\mathbf{H}$, which is assumed to be known for LMMSE channel estimators. In practice, $\mathbf{R}_{HH}$ can be estimated as in [31]. The LMMSE channel estimator in (3.2) can be obtained as

$$\begin{aligned}\hat{\mathbf{H}}_{MMSE} &= \mathrm{R}_{\mathbf{HH}}(\mathrm{R}_{\mathbf{HH}}+\sigma_n^2(\mathbf{P}^H\mathbf{P})^{-1})^{-1}\hat{\mathbf{H}}_{LS} \\ &= \mathbf{Q}\hat{\mathbf{H}}_{LS} \end{aligned} \tag{3.5}$$

where $\mathbf{H}_{LS}=\mathbf{P}^{-1}\mathbf{Y}$ and $\mathbf{Q}$ is the weighting matrix, given by

$$\mathbf{Q}=\mathrm{R}_{\mathbf{HH}}(\mathrm{R}_{\mathbf{HH}}+\sigma_n^2(\mathbf{P}^H\mathbf{P})^{-1})^{-1}. \tag{3.6}$$

A good estimator should minimize the variance of the estimated error. To evaluate the performance of the LMMSE estimators, we calculate the average MSE [28]

$$\mathrm{MSE}=\frac{1}{N}\mathbb{T}\mathrm{r}\left\{\mathbb{E}[\mathbf{e}_p\mathbf{e}_p^H]\right\} \tag{3.7}$$

where $\mathbf{e}_p=\mathbf{H}-\hat{\mathbf{H}}_{MMSE}$. The MSE for the LMMSE channel estimator can be written as

$$\begin{aligned}\mathrm{MSE}_{MMSE} &= \frac{1}{N}\mathbb{T}\mathrm{r}\left\{\mathbb{E}[(\mathbf{H}-\hat{\mathbf{H}}_{MMSE})(\mathbf{H}-\hat{\mathbf{H}}_{MMSE})^H]\right\} \\ &= \frac{1}{N}\mathbb{T}\mathrm{r}\left\{\mathrm{R}_{\mathbf{HH}}-\mathbf{Q}\mathrm{R}_{\mathbf{HH}}-\mathrm{R}_{\mathbf{HH}}\mathbf{Q}^H+\mathbf{Q}\mathbb{E}[\hat{\mathbf{H}}_{LS}\hat{\mathbf{H}}_{LS}^H]\mathbf{Q}^H\right\} \end{aligned} \tag{3.8}$$

and

$$\mathbb{E}\left[\hat{\mathbf{H}}_{LS}\hat{\mathbf{H}}_{LS}^H\right]=\mathrm{R}_{\mathbf{HH}}+\sigma_n^2(\mathbf{P}^H\mathbf{P})^{-1}. \tag{3.9}$$

Following (3.6) and (3.9), the MSE for LMMSE channel estimator can be obtained as

$$\mathrm{MSE}_{MMSE}=\frac{1}{N}\mathbb{T}\mathrm{r}\left\{\mathrm{R}_{\mathbf{HH}}-\mathbf{Q}\mathrm{R}_{\mathbf{HH}}\right\}. \tag{3.10}$$

To analyze the MSE, we assume that the auto-correlation matrix $\mathrm{R}_{\mathbf{HH}}$ is positive definite (please refer to Appendix A), and therefore invertible. Following (3.6), there is

$$\begin{aligned}\mathbb{T}\mathrm{r}\left\{\mathbf{Q}\mathrm{R}_{\mathbf{HH}}\right\} &= \mathbb{T}\mathrm{r}\left\{(\mathrm{R}_{\mathbf{HH}}^{-1}+\mathrm{R}_{\mathbf{HH}}^{-1}\sigma_n^2(\mathbf{P}^H\mathbf{P})^{-1}\mathrm{R}_{\mathbf{HH}}^{-1})^{-1}\right\} \\ &= \mathbb{T}\mathrm{r}\left\{(\mathbf{U}\Lambda_{\mathbf{H}}^{-1}\mathbf{U}^H+\mathbf{U}\Lambda_{\mathbf{H}}^{-1}\mathbf{U}^H\sigma_n^2(\mathbf{P}^H\mathbf{P})^{-1}\mathbf{U}\Lambda_{\mathbf{H}}^{-1}\mathbf{U}^H)^{-1}\right\} \\ &= \mathbb{T}\mathrm{r}\left\{(\Lambda_{\mathbf{H}}^{-1}+\Lambda_{\mathbf{H}}^{-1}\mathbf{U}^H\sigma_n^2(\mathbf{P}^H\mathbf{P})^{-1}\mathbf{U}\Lambda_{\mathbf{H}}^{-1})^{-1}\right\} \end{aligned} \tag{3.11}$$

where $\Lambda_{\mathbf{H}}$ is the diagonal matrix containing the eigenvalues λ_i ($i = 0, 1, \cdots, N-1$) of $\mathrm{R}_{\mathbf{HH}}$ on its diagonal and $\mathbf{U}$ is a unitary matrix containing eigen-vectors of $\mathrm{R}_{\mathbf{HH}}$ as its columns. The second equality is a result of the singular value decomposition (SVD) of matrix $\mathrm{R}_{\mathbf{HH}}$ ((A.4) in Appendix A) and the last equality is due to the fact that $\mathbb{T}\mathrm{r}\{\mathbf{URU}^H\} = \mathbb{T}\mathrm{r}\{\mathbf{R}\}$ when $\mathbf{U}$ is a unitary matrix and $\mathbf{R} \in \mathbb{M}_N$. We want to minimize the MSE in (3.10) through the design of $\mathbf{p}$, which is equivalent to maximizing (3.11).

Denote the $N \times N$ matrix $\mathbf{W}$ as

$$\mathbf{W} = \Lambda_{\mathbf{H}}^{-1} + \Lambda_{\mathbf{H}}^{-1}\mathbf{U}^H\sigma_n^2(\mathbf{P}^H\mathbf{P})^{-1}\mathbf{U}\Lambda_{\mathbf{H}}^{-1}. \tag{3.12}$$

It is shown in Appendix B that

$$\mathbb{T}\mathrm{r}\{\mathbf{W}^{-1}\} \leq \sum_{i=0}^{N-1} \frac{\lambda_i^2}{\lambda_i + \sigma_n^2} \tag{3.13}$$

where equality holds when

$$\mathbf{P}^H\mathbf{P} = \mathbf{I}_N. \tag{3.14}$$

Or equivalently

$$|P_i|^2 = 1, \text{ for } i = 0, 1, \cdots, N-1. \tag{3.15}$$

That is, the MSE of LMMSE estimator can achieve its minimum value when the pilot sequence has a flat spectrum. This result is in agreement with optimal training sequence properties for the LS frequency-domain channel estimator in [24].

When the optimal pilot sequence is utilized, the average MSE of the channel estimator can be obtained from (3.6), (3.10), (3.14) and (A.4) as

$$\begin{aligned} \mathrm{MSE}' &= \frac{1}{N}\mathbb{T}\mathrm{r}\{\Lambda_{\mathbf{H}} - \Lambda_{\mathbf{H}}(\Lambda_{\mathbf{H}} + \sigma_n^2\mathbf{I}_N)^{-1}\Lambda_{\mathbf{H}}\} \\ &= \frac{1}{N}\sum_{i=0}^{N-1}\left(\lambda_i - \frac{\lambda_i^2}{\lambda_i + \sigma_n^2}\right) \\ &= \frac{1}{N}\sum_{i=0}^{N-1}\frac{\lambda_i}{\lambda_i + \sigma_n^2}\sigma_n^2. \end{aligned} \tag{3.16}$$

Also, we can obtain from (3.13) that

$$\begin{aligned} \text{MSE} &= \frac{1}{N}\mathbb{T}\text{r}\{\text{R}_{\mathbf{HH}} - \mathbf{Q}\text{R}_{\mathbf{HH}}\} \\ &= \frac{1}{N}\mathbb{T}\text{r}\{\Lambda_{\mathbf{H}} - \mathbf{W}^{-1}\} \\ &\geq \frac{1}{N}\sum_{i=0}^{N-1}\left(\lambda_i - \frac{\lambda_i^2}{\lambda_i + \sigma_n^2}\right) \\ &= \text{MSE}' \end{aligned} \tag{3.17}$$

where the equality holds when (3.14) is satisfied. Therefore, the average MSE of the LMMSE channel estimator is lower bounded by MSE$'$, with its minimum value achieved when the optimal pilot symbols with a flat spectrum are utilized. Examples of optimal pilot symbols can be found in [24].

Note that a different method to estimate the channel frequency response $\mathbf{H}$ is to perform MMSE estimation of the L $(< N)$ channel taps $\mathbf{h}$ in the time domain followed by an FFT. However, it can be shown that the time domain method does not guarantee the lowest MSE in the frequency domain (Please see Appendix D). That is, performing an FFT on the time-domain taps obtained by MMSE estimation does not guarantee an optimal estimation in terms of MSE in the frequency domain.

3.3 Frequency-Domain Channel Estimation with Reduced Complexity

Under the condition when optimal pilot symbols are utilized, the matrix inverse in (3.6) is independent of the pilot sequence and needs to be performed only once if $\text{R}_{\mathbf{HH}}$ and σ_n^2 are known beforehand [28]. Therefore, the LMMSE estimator has a reduced complexity and becomes

$$\begin{aligned} \hat{\mathbf{H}}'_{MMSE} &= \text{R}_{\mathbf{HH}}(\text{R}_{\mathbf{HH}} + \sigma_n^2\mathbf{I}_N)^{-1}\hat{\mathbf{H}}_{LS} \\ &= N\mathbf{F}\text{R}_{\tilde{\mathbf{h}}\tilde{\mathbf{h}}}(N\text{R}_{\tilde{\mathbf{h}}\tilde{\mathbf{h}}} + \sigma_n^2\mathbf{I}_N)^{-1}\mathbf{F}^H\hat{\mathbf{H}}_{LS} \end{aligned} \tag{3.18}$$

where $\mathrm{R}_{\tilde{\mathbf{h}}\tilde{\mathbf{h}}} = \mathbb{E}[\tilde{\mathbf{h}}\tilde{\mathbf{h}}^H]$ is the time-domain auto-correlation function and the second equality in (3.18) is due to (A.4) in Appendix A.

As the estimator is now using time-domain channel statistics, the computational complexity of the LMMSE channel estimator can be further reduced as in [28], by knowing the fact that for typical UWB channels, time-domain channel taps only dominate the first L' taps, where L' varies for different channel models and data rates in UWB channels. Therefore, matrix $\mathrm{R}_{\tilde{\mathbf{h}}\tilde{\mathbf{h}}}$ can be reduced to $\mathrm{R}'_{\mathbf{hh}}$, which is an $L' \times L'$ auto-correlation matrix of the first L' time-domain channel taps, and the typical values of N, L and L' are presented in Section 3.4. The simplified estimator can be obtained as

$$\begin{aligned} \hat{\mathbf{H}}'_{MMSE} &= N\mathbf{F}'_L\mathbf{R}'_{\mathbf{hh}}(N\mathbf{R}'_{\mathbf{hh}} + \sigma_n^2\mathbf{I}_{L'})^{-1}\mathbf{F}'^H_L\hat{\mathbf{H}}_{LS} \\ &= \mathbf{Q}'\hat{\mathbf{H}}_{LS} \end{aligned} \tag{3.19}$$

where $\mathbf{F}'_L$ is the first L' columns of the DFT matrix $\mathbf{F}$ and the weighting matrix becomes

$$\mathbf{Q}' = N\mathbf{F}'_L\mathbf{R}'_{\mathbf{hh}}(N\mathbf{R}'_{\mathbf{hh}} + \sigma_n^2\mathbf{I}_{L'})^{-1}\mathbf{F}'^H_L. \tag{3.20}$$

The number of complex multiplication of matrix calculation in (3.19) therefore becomes $N \times L'^2$, which is much smaller than N^3 required in (3.18). The reduction in computational complexity, however, is at the expense of the performance degradation in terms of MSE. That is, the simplified estimator in (3.19) no longer yields the minimum MSE as (3.18), since not all the non-zero channel taps are involved in calculating the channel auto-correlation matrix. Nevertheless, as long as a reasonable number of time-domain channel taps are chosen, the performance degradation is very small and the simplified estimator performs well under the evaluated UWB channels, as will be shown in Section 3.4.

We further notice that in estimator (3.19), an optimal pilot block with flat spectrum is required, which can be obtained by the employment of a search procedure [24]. Efforts on the search of the optimal sequence exert additional computational complexity in channel estimation. To further reduce the complexity in channel estimation, we simplify the estimator in (3.19) by using non-optimal pilot sequences and dividing the channel estimation

into two steps:

1) Perform the coarse LS estimation of $\mathbf{H}$ by $\hat{\mathbf{H}}_{LS}$, with no restrictions on the pilot sequence. That is, the pilot sequences are not obligated to be optimal and have a flat spectrum.

2) Get the fine estimation value by weighting $\hat{\mathbf{H}}_{LS}$ with $\mathbf{Q}'$ in (3.20).

Simulation results employing the non-optimal pilot symbols are also presented in Section 3.4, where randomly generated BPSK symbols are used as pilots. Our results show that the performance degradation due to non-optimal pilot symbols can be compensated by sending multiple blocks of pilot symbols, at the expense of a reduced throughput.

3.4 Simulation Results and Discussions

The performance of the proposed low complexity frequency-domain channel estimator under UWB propagation environments is presented in this section, compared with that with perfect channel state information. The UWB channels used are CM1-CM4 proposed by the IEEE 802.15.3a study group [2]. The investigated SC-FDE system follows that of the system model in Chapter 2, where a data block length $N = 256$ is used, with CP length of 64 and the bit duration of 2 ns, indicating an information data rate of 400 Mbps. As in Chapter 2, the root raised cosine pulse with roll off factor of 0.5 is employed as the pulse shaping filter. In both numerical evaluation and simulations, the transmitted pulse shaping filter, the receiver matched filter and one of the 100 channel realizations for a particular UWB channel model are convolved to form 100 different equivalent channel realizations over which the BERs are averaged. The second order channel statistics are obtained using Monte-Carlo simulation, where $\mathbf{h}\mathbf{h}^H$ is calculated and averaged over 100 channel realizations. The length L' is chosen by simulation to gather up to 99% of the channel energy (30 for CM1, 40 for CM2, 70 for CM3 and 100 for CM4). Fewer number of time-domain taps can be selected, at the cost of a performance degradation, as will be shown in Fig. 3.10.

For multiple blocks of pilot symbols, the estimates of channel spectrum coefficients are obtained from each pilot block and then averaged over these blocks. The non-optimal

pilot blocks used in the simulation are randomly generated BPSK symbols, while the optimal pilots are simply a delta pulse with energy $\sqrt{N}$, based on the assumption that the transmitter is capable of providing two distinct power levels, one for pilots and one for data transmission. In practice, however, perfect flat spectrum of pilot symbols is usually hard to obtain and the search of optimal pilot sequences is required. Some low complexity search strategies where presented in [24] and [25]. Nevertheless, with an ideal flat spectrum for pilots constructed in our simulation, the results presented here are the best achievable performance of the proposed estimator when optimal pilot symbols are utilized.

The lower bound of the MSE value and the MSE of the proposed channel estimator (3.19) for UWB channels CM1-CM4 are shown in Figs. 3.2-3.5, compared with the MSE for the LMMSE channel estimator in (3.5). As can be observed, for each evaluated UWB channel model, the MSE of the proposed channel estimator achieves its lower bound at low SNRs. Reducing the dimension of the auto-correlation matrix tends to have more effect on performance at high SNRs where the value of MSE diverges from the lower bound and becomes slightly larger than that of the frequency-domain LMMSE estimator (3.5). However, the MSE of the proposed channel estimator can achieve its lower bound MSE$'$ at all the evaluated SNR when additional non-zero channel taps are included in the calculation of $\mathbf{R}'_{\mathbf{hh}}$.

The performance of the frequency-domain low complexity channel estimator (3.19) for SC-FDE under the UWB channels CM1-CM4 are plotted in Figs. 3.6-3.9, where both the optimal and non-optimal pilot sequences are employed. The BER performance with perfect channel state information is also shown for comparison. It is observed that the proposed low complexity estimator performs well for the SC-FDE system under UWB propagation environment. Compared to the performance with perfect channel state information, when 3 blocks of non-optimal pilot symbols are utilized, only a slight performance degradation of about 0.5 dB is incurred for CM1 and CM2, while approximately a 2 dB performance degradation relative to the performance with perfect channel state information is observed for CM3 and CM4. Furthermore, increasing the length of the pilot symbols only slightly

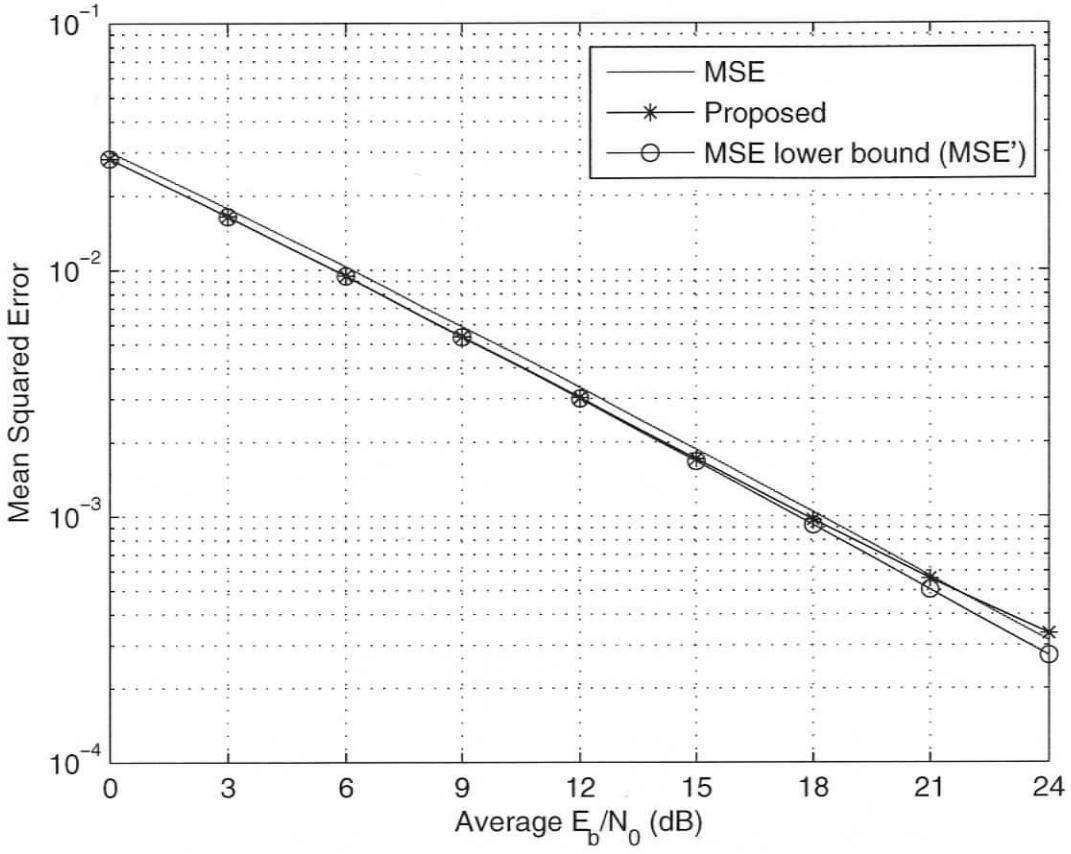

Figure 3.2. *The MSE comparison of the proposed low-complexity estimator, frequency-domain LMMSE estimator, and MSE lower bound for the UWB channel CM1.*

improves the BER performance for CM1 and CM2, where the performances with 2 and 3 blocks of pilot symbols are already very close. However, this is not the case for channel models CM3 and CM4, where a performance gain of about 1 dB can be obtained when the length of pilot symbols increases from 1 block to 3 blocks. When the optimal pilot symbols are utilized, a slight performance improvement of 0.5 dB can be obtained for CM3 and CM4 by increasing the length of pilot symbols from 1 block to 2 blocks. It can also be observed that, for each evaluated UWB channel model, the performance with 3 blocks of non-optimal pilot symbols is very close to that with 1 block optimal pilot symbols. Therefore, the degradation due to non-optimal pilots can be compensated by

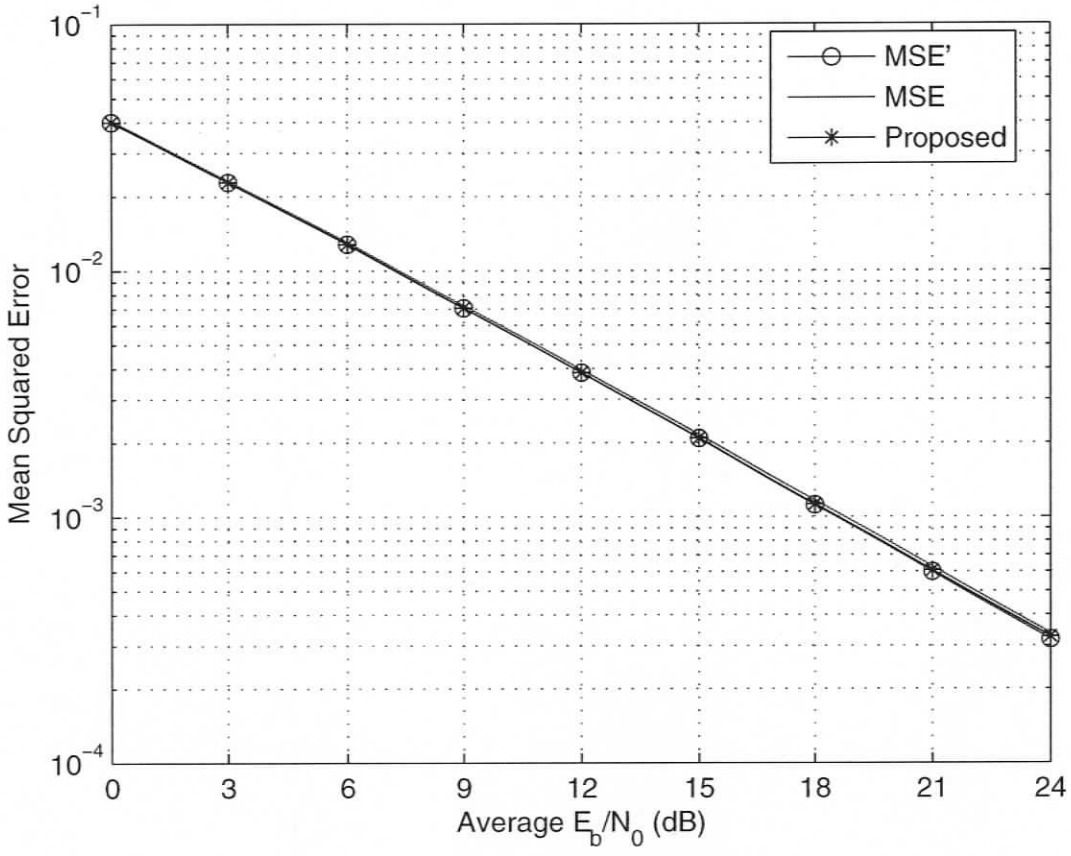

Figure 3.3. *The MSE comparison of the proposed low-complexity estimator, frequency-domain LMMSE estimator, and MSE lower bound for the UWB channel CM2.*

sending multiple pilot blocks at the transmitter, at the cost of reduced throughput.

In order to illustrate the effect of L' selection for the proposed low complexity frequency-domain channel estimator, we plot in Fig. 3.10 the average BER performance over 100 UWB channel realizations of CM4 using the proposed low complexity frequency-domain channel estimator with different number of channel taps. The percentile of the gathered energy averaged over 100 UWB channel realizations is shown in Table I. It can be observed that at low to medium SNRs, there is minor performance degradation using fewer time-domain channel taps (such as 60, 70 or 80). However, at high SNRs, although the channel energy gathered by fewer time-domain channel taps only slightly decreases, obvi-

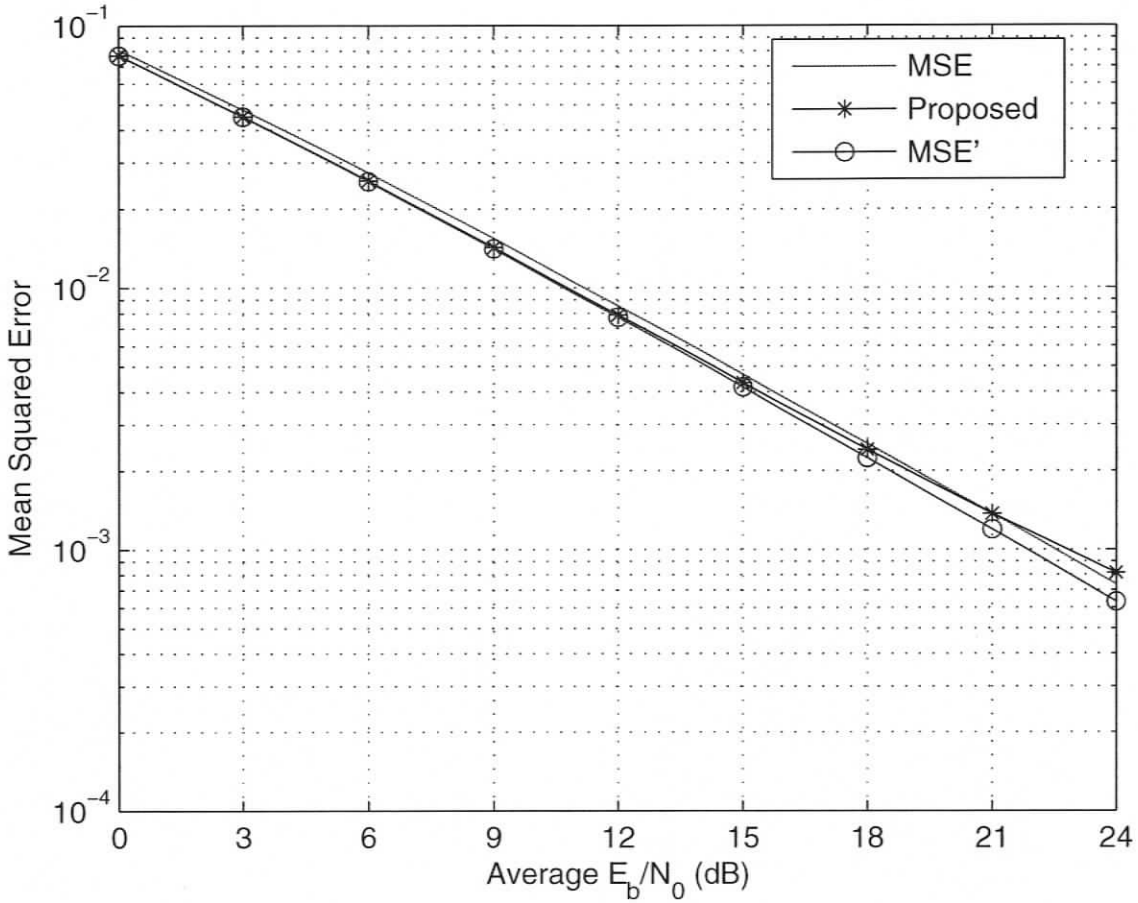

Figure 3.4. *The MSE comparison of the proposed low-complexity estimator, frequency-domain LMMSE estimator, and MSE lower bound for the UWB channel CM3.*

ous performance degradation can be observed by using 60, 70 or 80 time-domain channel taps. Therefore, gathering enough channel energy does not guarantee a reasonable performance for the low complexity frequency-domain channel estimator at high SNRs, and sufficient number of channel taps has to be utilized. This is due to the fact that an increased MSE divergence from its lower bound occurs when the number of channel taps is reduced. Note that even when 100 taps are used for the time-domain auto-correlation matrix, the dimensionality is still much lower than the N-by-N (e.g., 256×256) frequency-domain auto-correlation matrix.

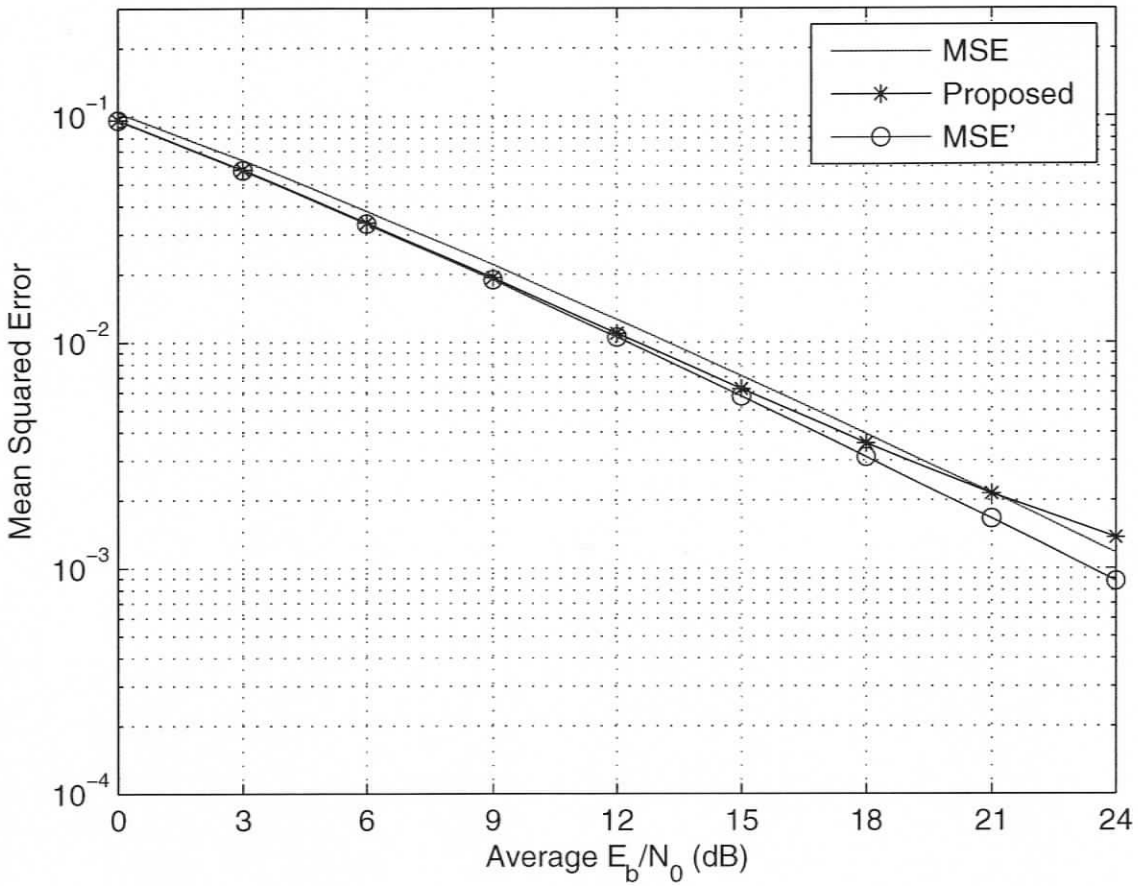

Figure 3.5. *The MSE comparison of the proposed low-complexity estimator, frequency-domain LMMSE estimator, and MSE lower bound for the UWB channel CM4.*

Table 3.1. *Number of Taps vs. Gathered Channel Energy in CM4*

Number of Taps	Energy Gathered
100	99.9%
90	99.7%
80	99.4%
70	98.9%
60	97.9%

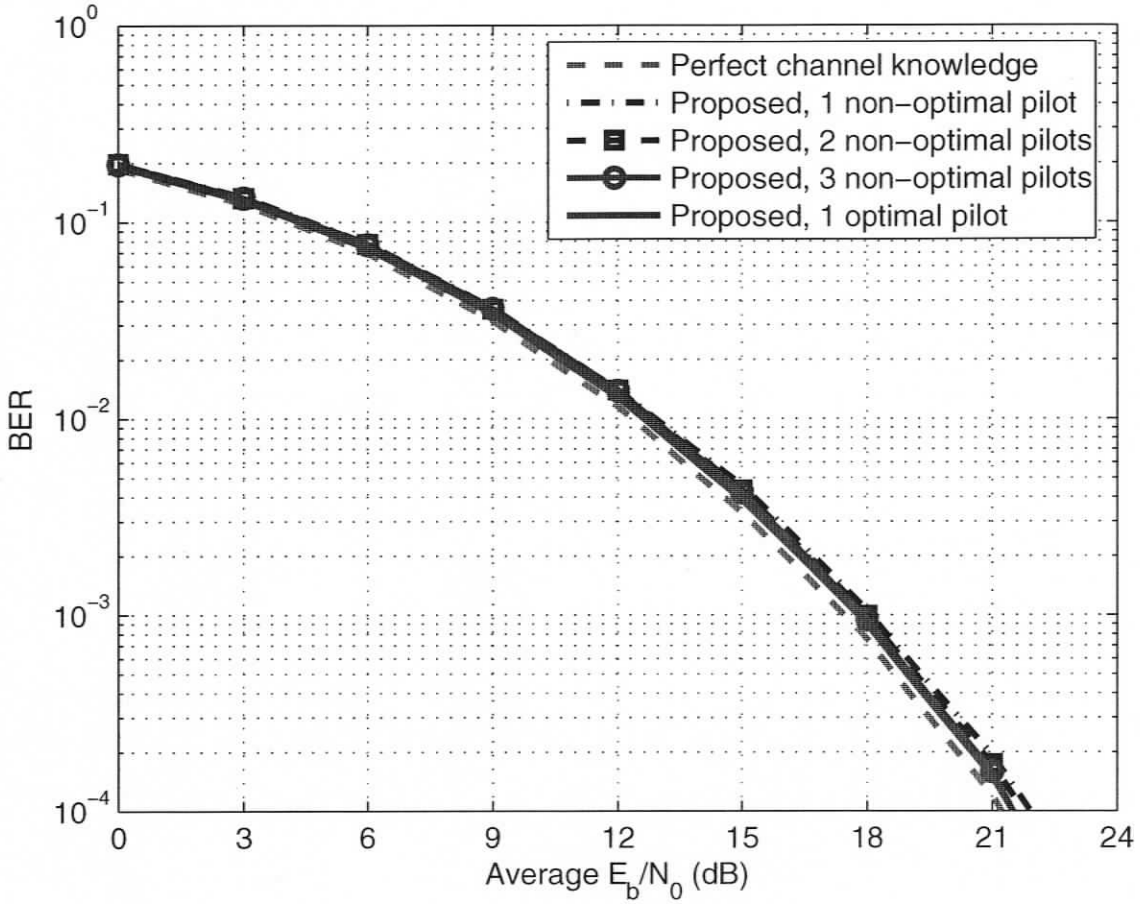

Figure 3.6. *The performance comparison between the proposed low-complexity estimator with that of the perfect channel state information of the SC-FDE transmission over the UWB channel CM1.*

3.5 Summary

Based on a derived lower bound for the MSE of the frequency-domain LMMSE estimator, a low complexity frequency-domain channel estimator for SC-FDE transmission over UWB IEEE 802.15.3a channels has been proposed and its performance has been evaluated. The effects of employing optimal and non-optimal pilot symbols in the proposed channel estimator have been compared and discussed. It has been shown that the proposed channel

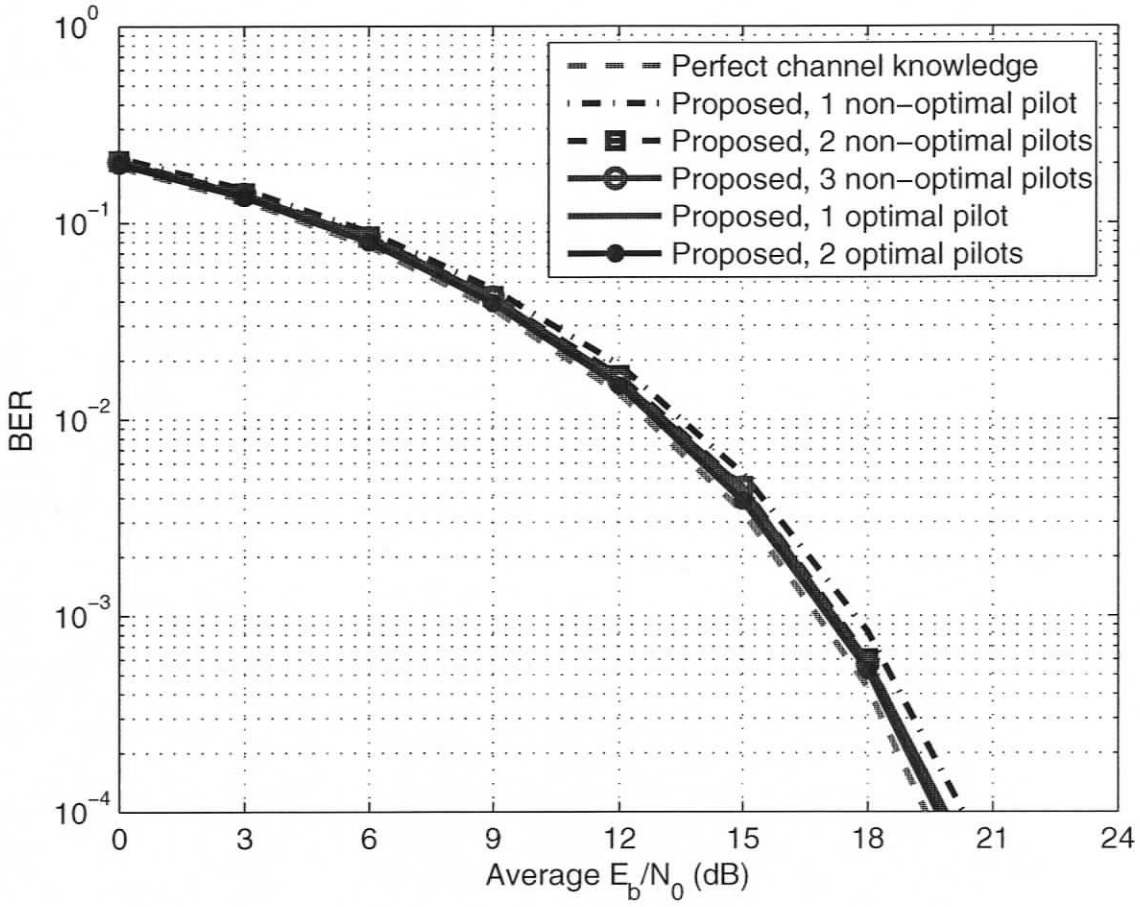

Figure 3.7. *The performance comparison between the proposed low-complexity estimator with that of the perfect channel state information of the SC-FDE transmission over the UWB channel CM2.*

estimator works reasonably well for the SC-FDE system under UWB channels and the performance degradation due to non-optimal pilots can be compensated by sending multiple blocks of pilot symbols.

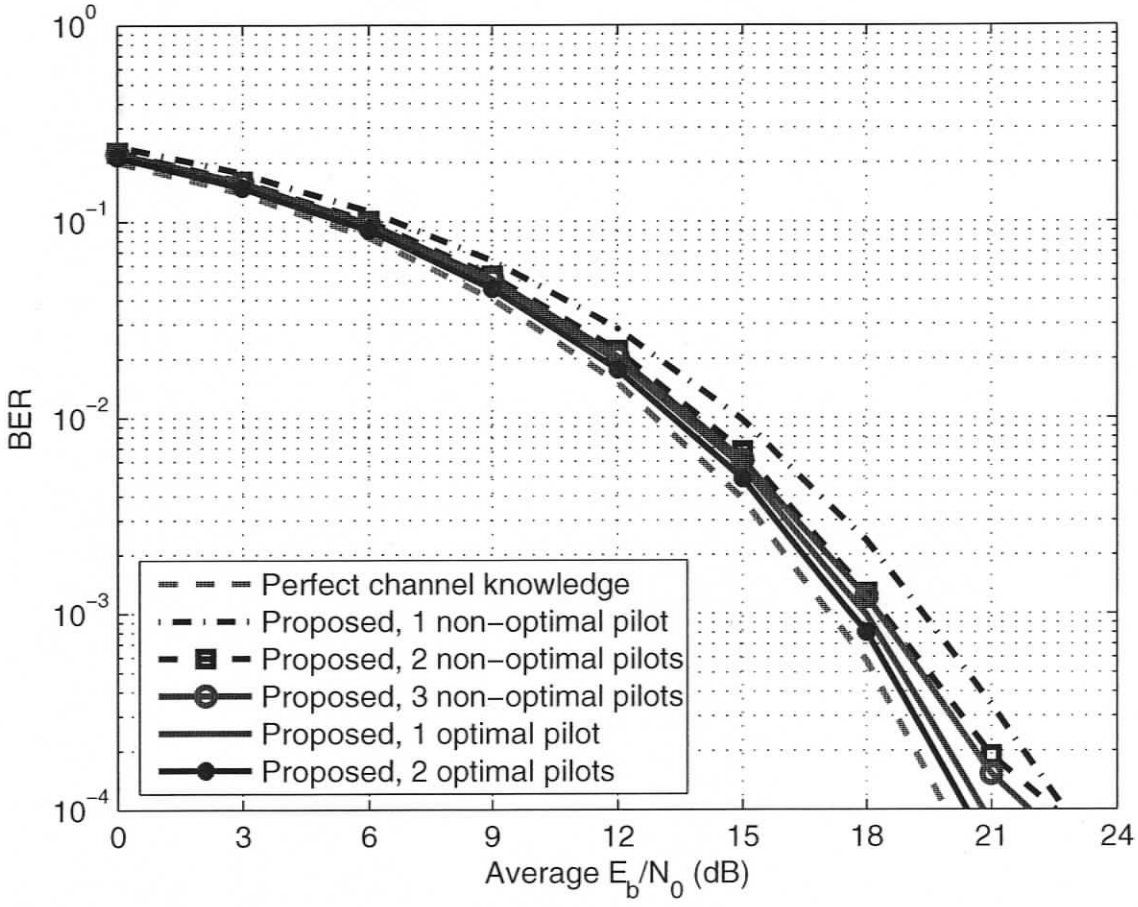

Figure 3.8. *The performance comparison between the proposed low-complexity estimator with that of the perfect channel state information of the SC-FDE transmission over the UWB channel CM3.*

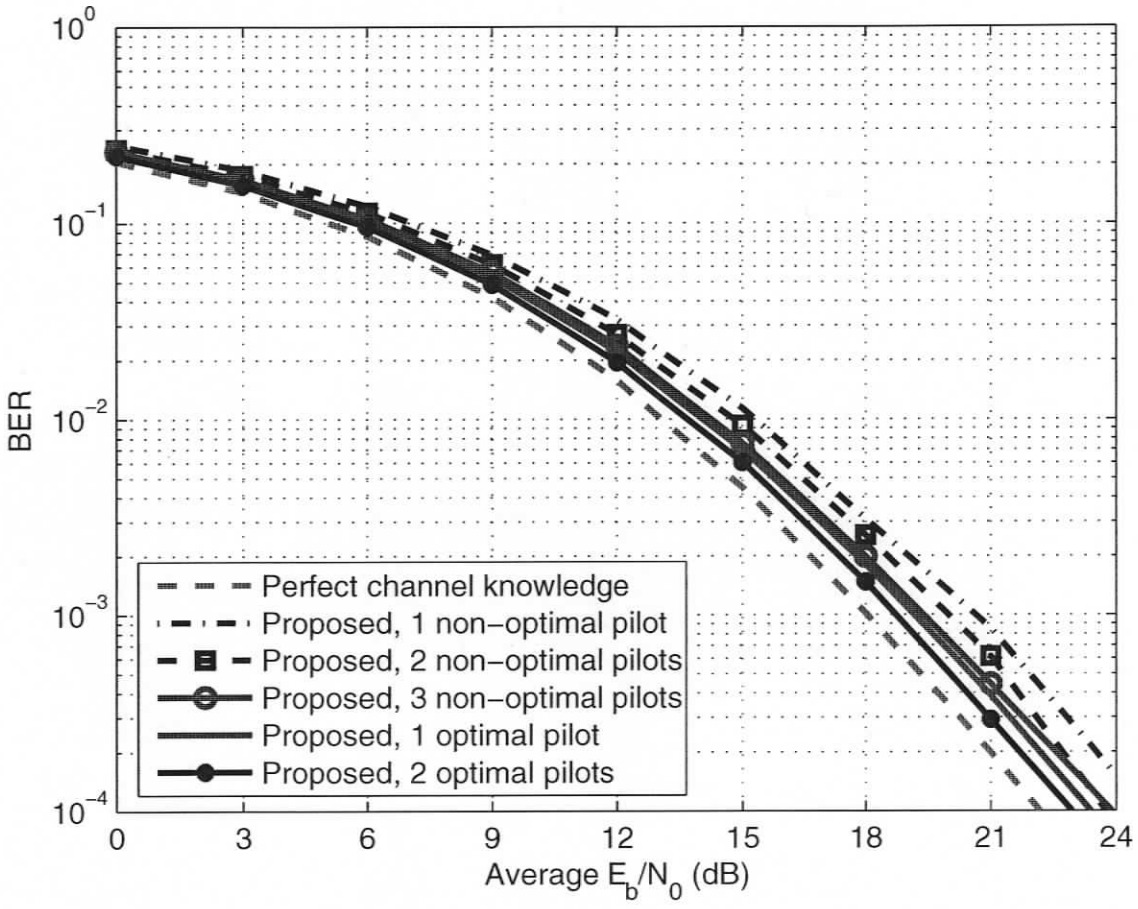

Figure 3.9. *The performance comparison between the proposed low-complexity estimator with that of the perfect channel state information of the SC-FDE transmission over the UWB channel CM4.*

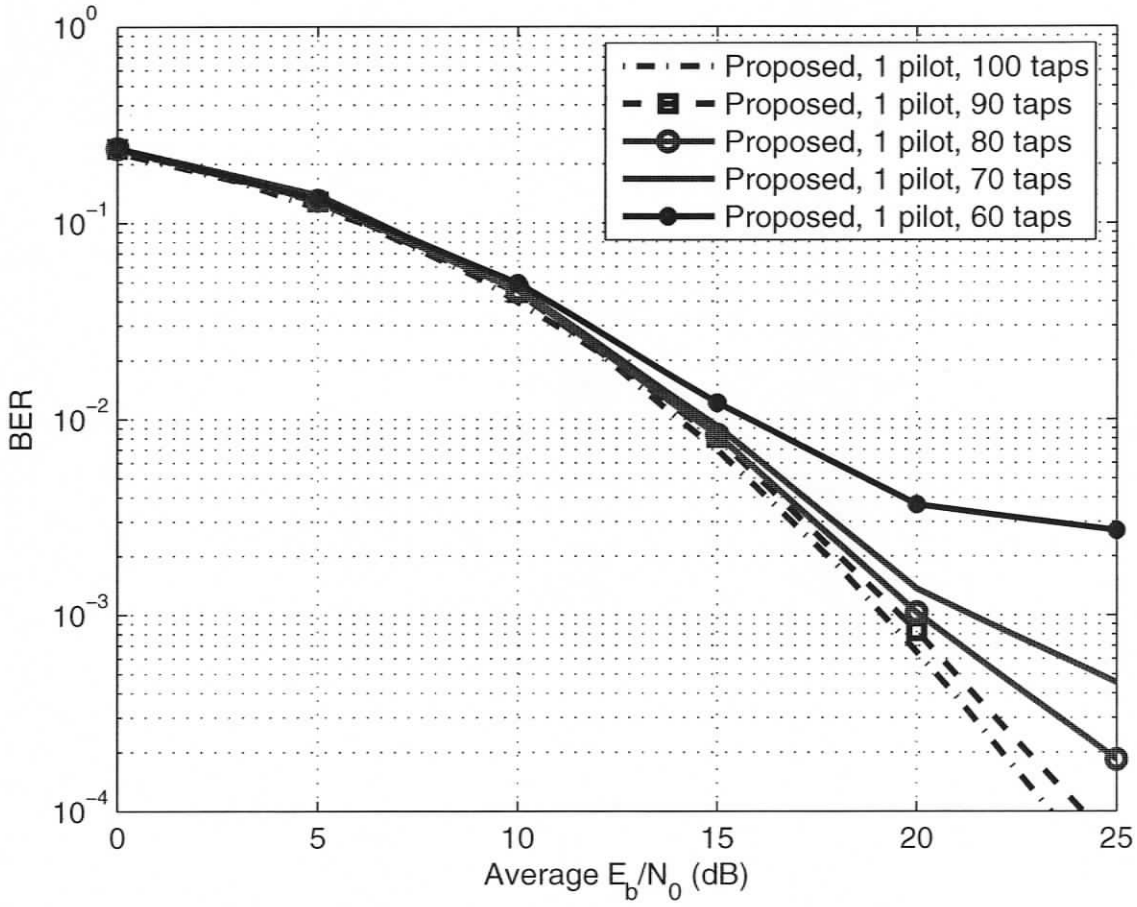

Figure 3.10. *BER performance of the proposed channel estimator using different number of time-domain channel taps for the auto-correlation matrix in CM4.*

Chapter 4

A Time Division Multiple Access SC-FDE System with IBI Suppression for UWB Communications

4.1 Background

In this chapter, we extend the single user SC-FDE system in Chapter 2 to a multiple access system, where the BPSK modulated data for each user are transmitted block-wisely over UWB channels.

Multiple access in UWB communications has gained a considerable research interest [5], [32], [33]. Relying on orthogonal spreading codes to separate different users, most of the current scheme for block transmission are based on CDMA, where MAI free reception is achieved when the orthogonality of the spreading codes among different users can be guaranteed. However, it is usually hard to maintain the code orthogonality in a propagation environment where large number of multipath components are present, as in UWB channels. When rake reception is utilized to collect the multipath components, a large number of channel taps and delays have to be estimated within a short data transmission time, which leads to high computational complexity. In [32], adaptive MMSE scheme was proposed for UWB multiuser detection and was shown to have a better performance than rake reception with 8 fingers. However, in the UWB channel with a large number of multipath

components, the computational complexity of the MMSE scheme is too high and thus practically unaffordable [33]. Recently, the block spreading CDMA, initially proposed in [34], was applied to MAI free detection in UWB communications [33]. It was shown to achieve a better performance than the MMSE multiuser detection and at the same time maintain a simple receiver structure. As in all block transmissions with frequency-domain equalization, the CDMA scheme proposed in [33] requires the insertion of CP between blocks to combat IBI. In a UWB environment where large channel delay spread is present, a long CP is required to ensure IBI free. This issue becomes more critical when block spreading is utilized to accommodate multiple users, since the channel impulse response will span even a greater number of chips due to the high chip rate required to achieve a desired system data rate, resulting in a larger CP length to avoid IBI. In practice, however, a reasonable system complexity for UWB communications has been recommended as an FFT size of 128 and CP length of 32 [6], which is much shorter than that required in the block spread CDMA system [33].

To achieve a high system data rate and keep a low implementation complexity, we propose a novel TDMA transceiver scheme for the BPSK modulated SC-FDE system in UWB channels, where IBI-free transmission is achieved without inserting CP between blocks. Thanks to the simple BPSK, where only in-phase baseband signals are used for detection, interference due to multiple access can be lumped into the quadrature component after the transmitter and receiver processing, resulting in an MAI free SC-FDE system at possibly high data rate for UWB communications.

This chapter is organized as follows. Section 4.2 presents a brief description of the multiple access SC-FDE system model. In Section 4.3, we derive the transmitter and receiver matrices of the proposed TDMA scheme for BPSK modulated SC-FDE system in UWB communications. Transmitter and receiver matrices design on how to achieve the desired MAI and IBI free reception for arbitrary number of users is illustrated, followed by the application of the oversampling diversity combining scheme to the proposed system. In Section 4.4, we present the simulation results of our proposed TDMA system, compared

with that of the block spread CDMA system [33] in various UWB channel models. The effects of oversampling diversity and channel estimation errors on the performance of the proposed TDMA system are also studied. System data rate and bandwidth efficiency are discussed in the last part of Section 4.4. Section 4.5 concludes this chapter.

4.2 Multiple Access SC-FDE System Model

We consider a BPSK modulated multiple access SC-FDE system over IEEE 802.15.3a UWB channels with M total number of users. Data stream of the mth ($m = 1,2,\cdots M$) user is transmitted on a block by block basis with a block length N, where the ith block of the transmitted signals is denoted as $\mathbf{x}_m(i) = [x_m((i-1)N), x_m((i-1)N+1), \cdots, x_m(iN-1)]^T$, and where the symbols $x_m(i)$ are binary and have values ± 1. We assume the block boundaries of all users are synchronized. The transmitted block of each user is then multiplied by an $(M+1)N \times N$ transmitter matrix $\mathbf{T}_m$ and yields a column vector $\mathbf{s}_m(i)$, given by

$$\mathbf{s}_m(i) = \mathbf{T}_m \mathbf{x}_m(i). \tag{4.1}$$

The transmitted data block $\mathbf{x}_m(i)$ of length N is thus expanded to the "superblock" $\mathbf{s}_m(i)$ of length $(M+1)N$, where each element in $\mathbf{s}_m(i)$ is referred to as a "chip". The vectors $\mathbf{s}_m(i)$ then form a serial stream of data $[s_m(0), s_m(1), \cdots, s_m((M+1)N), s_m((M+1)N+1), \cdots]^T$ of the mth user, which is pulse shaped and transmitted over the UWB channel. It will become clear later why $M+1$ times the block length is needed for the superblock.

At the receiver, the composite received data stream $\mathbf{y}$ is obtained by each user and processed separately. At each user end, the received signal with noise and interference from other users is fed to the matched filter and sampled at the chip rate. Assuming timing is acquired, the composite received sequence can be written as [34]

$$y(k) = \sum_{m=1}^{M} \sum_{l=0}^{L_m-1} h_m(k) s_m(l-k) + n(k) \tag{4.2}$$

where $h_m(k)$ is the kth channel tap of the equivalent T-spaced channel impulse response of the mth user, L_m is the total number of paths in the mth propagation channel. Moreover,

the kth noise component $n(k)$ is a Gaussian RV with variance $\sigma_n^2 = \frac{N_0}{2}$. A more general scenario is that there are M pairs of transmit-receive users, and the signal arriving at each receiver may not be the same as those at the other $M-1$ receivers due to different propagation channels among the M pairs of users. The multiple access scheme presented in this chapter is applicable to the general scenario and the subsequent discussion only considers one identical received sequence $y(k)$ to illustrate the multiple access scheme.

After S/P conversion, the serial received data stream is divided into length $(M+1)N$ column vectors $\mathbf{y}(i)$, which is the ith received superblock and $\mathbf{y}(i) = [y((i-1)(M+1)N), y((i-1)(M+1)N+1), \cdots, y(i(M+1)N-1)]^T$. A matrix multiplication is then performed on the received superblock. The data block of the rth user before the FFT can then be obtained as

$$\mathbf{v}_r(i) = \mathrm{Re}\{\mathbf{u}_r(i)\} = \mathrm{Re}\{\mathbf{R}_r\mathbf{y}(i)\} \tag{4.3}$$

where $\mathbf{R}_r$ is the receiver matrix with dimension $N \times (M+1)N$. After the matrix transformation, taking the real part of $\mathbf{u}_r(i) = \mathbf{R}_r\mathbf{y}(i)$ will be able to separate the rth user data from the received composite signal $\mathbf{y}(i)$. Our objective is to design the $\mathbf{T}_m$ and $\mathbf{R}_r$ $(m, r = 1, \cdots, M)$ to achieve MAI and IBI free detection.

Once the data of each user are separated, the subsequent processing for the rth user data block is identical to the single user case as in Chapter 2, where equalization is performed in the frequency domain to eliminate ISI within the individual transmission blocks. The equalized signal is then transformed back into the time domain, which can be expressed as

$$\mathbf{z}_r(i) = \mathbf{F}^H\mathbf{C}_r\mathbf{F}\mathbf{v}_r(i) \tag{4.4}$$

where $\mathbf{C}_r$ is the diagonal $N \times N$ equalization matrix for the rth user, with frequency-domain equalizer taps $C_r(k)$ on its kth diagonal entry. Supposing the noise samples in $\mathbf{v}_r(i)$ are uncorrelated, the frequency-domain MMSE equalizer taps are given by $C_r(k) = \frac{H_r^*(k)}{|H_r(k)|^2 + N_0/E_b}$ [11], where $H_r(k)$ is the kth frequency-domain channel attenuation factor of the rth propagation channel, and E_b is the average energy per transmitted bit. Moreover, N_0 is the variance of the effective noise before the FFT, which is doubled after the matrix mul-

tiplication, as will be illustrated in Section 4.3. Signal detection is then performed in the time domain and the decision variable for the BPSK transmitted symbol becomes $\hat{\mathbf{x}}_r(i) = \text{sgn}(\text{Re}\{\mathbf{z}_r(i)\})$.

The block diagram in Fig. 4.1 describes the investigated multiple access SC-FDE system, where only the mth user is shown. Note that although a similar transceiver structure is employed as in the block spread CDMA system [33], our scheme does not use the orthogonal spreading code to separate different users. Instead, we manipulate the transmit and receiver matrices $\mathbf{T}_m$ and $\mathbf{R}_r$, $(m, r = 1, \cdots, M)$ to achieve an MAI free and IBI free reception without CP insertion between blocks, which essentially results in a TDMA transmission scheme, as will be shown in the next section.

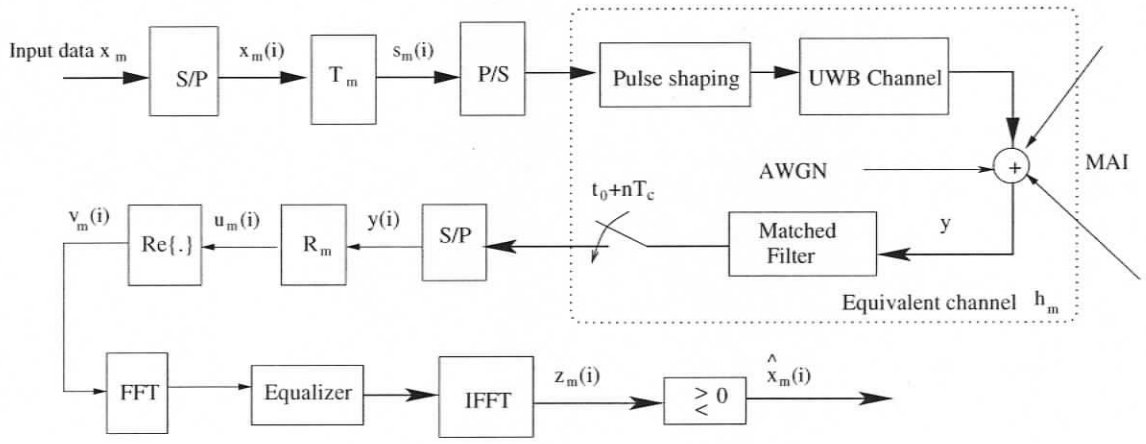

Figure 4.1. *Proposed multiple access SC-FDE system of the mth user*

4.3 TDMA Transceiver Design

In this section, we present the proposed TDMA transceiver design for BPSK modulated SC-FDE transmission in UWB channels. We first take the 4 user case as an example to illustrate how the matrix manipulation is performed to obtain the MAI-free and IBI-free communication. In the second part of this section, we will present the general method on how to design the transmitter and receiver matrix for arbitrary number of users. The third

subsection will introduce the oversampling diversity scheme into the proposed multiple access system.

4.3.1 Transceiver Design

The scheme follows the block diagram of system model in Fig. 4.1. The BPSK modulated data block of the mth user is multiplied by the transmitter matrix $\mathbf{T}_m$, which can be decomposed as $\mathbf{T}_m = \boldsymbol{\alpha}_m \otimes \mathbf{I}_N$, where $\boldsymbol{\alpha}_m$ is a length $M+1$ column vector unique for the mth user. Unlike the block spreading in [33] where a matrix of dimension $M(N+L_m) \times N$ is utilized as the transmitter matrix to insert CP, the Kronecker's product in our scheme is applied to the column vector $\boldsymbol{\alpha}_m$ and an $N \times N$ identity matrix $\mathbf{I}_N$, resulting in an $(M+1)N \times N$ transmitter matrix. Therefore no CP is inserted between blocks, resulting in a reduced complexity and an increased throughput. It is known that when the block size is larger than the number of channel multipath components, the relationship between the transmitted and received data can be expressed as [34]

$$\mathbf{y}(i) = \sum_{m=1}^{M} [\mathbf{H}_{m,L}\mathbf{T}_m\mathbf{x}_m(i) + \mathbf{H}_{m,U}\mathbf{T}_m\mathbf{x}_m(i-1)] + \mathbf{n}(i) \tag{4.5}$$

where $\mathbf{n}(i)$ is the length $(M+1)N$ noise vector of the ith received superblock, and each element in $\mathbf{n}(i)$ is a zero mean Gaussian RV with variance σ_n^2. Furthermore, $\mathbf{H}_{m,L}$ is the $(M+1)N \times (M+1)N$ lower triangular Toeplitz matrix of the mth propagation channel, with the first column being $[h_m(0), h_m(1), \cdots, h_m(L_m-1), 0, \cdots, 0]^T$; $\mathbf{H}_{m,U}$ is the $(M+1)N \times (M+1)N$ upper triangular Toeplitz matrix of the mth propagation channel, with the first row being $[0, \cdots, 0, h_m(L_m-1), \cdots, h_m(1)]$.

The second additional term in (4.5) accounts for the IBI effects. General methods to suppress IBI include inserting CP with a length up to the number of channel taps between blocks. When CP is long enough to cover the channel delay spread, a circulant matrix of the multipath channel is formed by the insertion and removal of CP at the transmitter and receiver, respectively. From a single user perspective, the subsequent FFT and

frequency-domain equalization can be carried out properly when the multipath channel effect is expressed as a circulant matrix, that is $\mathbf{v}_r(i) = \tilde{\mathbf{H}}_r \mathbf{x}_r(i) + \boldsymbol{\eta}_r(i)$ where $\mathbf{v}_r(i)$ is the ith received block before the FFT operation, $\tilde{\mathbf{H}}_r$ is an $N \times N$ circulant Toeplitz matrix with the first column being $[h_r(0), \cdots, h_r(L_r - 1), 0, \cdots, 0]^T$, and $\boldsymbol{\eta}_r(i)$ is the equivalent noise term. The reason lies in the fact that the circulant matrix can be decomposed as

$$\tilde{\mathbf{H}}_r = \mathbf{F}^H \Lambda_r \mathbf{F} \tag{4.6}$$

where Λ_r is an $N \times N$ diagonal matrix with $H_r(k)$ on the kth diagonal entry.

The method of inserting CP invokes penalty in bandwidth efficiency in the multiple access UWB communications since the required CP length increases with the system data rate and the number of accommodated users. Applying insufficient CP between blocks gives rise to performance degradation due to the following two aspects. First, the IBI effects cannot be eliminated since the second additional term in (4.5) is no longer zero. Furthermore, the multipath channel matrix can no longer be formed as a circulant matrix with the insertion and removal of insufficient CP. Hence, the decomposition in (4.6) cannot be applied and the subsequent FFT and frequency-domain equalization cannot be performed as desired.

If, instead of utilizing CP, the transmitter and receiver matrices are manipulated to obtain a circulant matrix $\tilde{\mathbf{H}}_r$, the IBI effects within each user can be eliminated. At the same time, these matrix manipulations gather all the MAI interference into the quadrature component of the received data block. Since the in-phase BPSK data are not distorted by MAI, MAI-free reception can be achieved. This basically forms our idea of the MAI-free and IBI-free multiple access system in block BPSK transmission. Next, we illustrate the matrix manipulation in detail.

Following (4.5), at the receiver, the data block of each user is obtained by multiplying the received signal $\mathbf{y}(i)$ with a user-specific $N \times (M+1)N$ receiver matrix $\mathbf{R}_r (r = 1, \cdots, M)$

$$\mathbf{u}_r(i) = \mathbf{R}_r \sum_{m=1}^{M} [\mathbf{H}_{m,L} \mathbf{T}_m \mathbf{x}_m(i) + \mathbf{H}_{m,U} \mathbf{T}_m \mathbf{x}_m(i-1)] + \mathbf{R}_r \mathbf{n}(i) \tag{4.7}$$

where $\mathbf{R}_r$ can be expressed as $\mathbf{R}_r = \boldsymbol{\beta}_r \otimes \mathbf{I}_N$ and $\boldsymbol{\beta}_r$ is a length $M+1$ row vector. Using the Kronecker's product, the $(M+1)N \times (M+1)N$ matrix $\mathbf{H}_{m,L}$ can be rewritten as [34]

$$\mathbf{H}_{m,L} = \mathbf{I}_{M+1} \otimes \overline{\mathbf{H}}_{m,L} + \mathbf{J}_{M+1} \otimes \overline{\mathbf{H}}_{m,U} \tag{4.8}$$

where $\overline{\mathbf{H}}_{m,L}$ is an $N \times N$ lower triangular Toeplitz matrix, with the first column being $[h_m(0), h_m(1), \cdots, h_m(L_m-1), 0, \cdots, 0]^T$, and $\overline{\mathbf{H}}_{m,U}$ is an $N \times N$ upper triangular Toeplitz matrix with the first row being $[0, \cdots, 0, h_m(L_m-1), \cdots, h_m(1)]$. Matrix $\mathbf{J}_{M+1}$ is an $(M+1) \times (M+1)$ lower triangular Toeplitz matrix with the first column being $[0,\ 1,\ 0,\ \cdots 0]^T$. Similarly, the $(M+1)N \times (M+1)N$ Toeplitz matrix $\mathbf{H}_{m,U}$ can be written as

$$\mathbf{H}_{m,U} = \mathbf{L}_{M+1} \otimes \overline{\mathbf{H}}_{m,U} \tag{4.9}$$

where $\mathbf{L}_{M+1}$ is an $(M+1) \times (M+1)$ matrix with the $(1, M+1)$th entry being 1, and zero elsewhere.

Applying (4.8) and (4.9) to (4.7), the received data block of the rth user can be rewritten as

$$\begin{aligned}
\mathbf{u}_r(i) &= \mathbf{R}_r \sum_{m=1}^{M} \left[\mathbf{I}_{M+1} \otimes \overline{\mathbf{H}}_{m,L} + \mathbf{J}_{M+1} \otimes \overline{\mathbf{H}}_{m,U}\right] \mathbf{T}_m \mathbf{x}_m(i) \\
&\quad + \mathbf{R}_r \sum_{m=1}^{M} \left[\mathbf{L}_{M+1} \otimes \overline{\mathbf{H}}_{m,U}\right] \mathbf{T}_m \mathbf{x}_m(i-1) + \mathbf{R}_r \mathbf{n}(i) \\
&= \left[\sum_{m=1}^{M} \boldsymbol{\beta}_r \boldsymbol{\alpha}_m \otimes \overline{\mathbf{H}}_{m,L} + \sum_{m=1}^{M} \boldsymbol{\beta}_r \mathbf{J}_{M+1} \boldsymbol{\alpha}_m \otimes \overline{\mathbf{H}}_{m,U}\right] \mathbf{x}_m(i) \\
&\quad + \sum_{m=1}^{M} \boldsymbol{\beta}_r \mathbf{L}_{M+1} \boldsymbol{\alpha}_m \otimes \overline{\mathbf{H}}_{m,U} \mathbf{x}_m(i-1) + \boldsymbol{\xi}_r(i)
\end{aligned} \tag{4.10}$$

where $\boldsymbol{\xi}_r(i) = \mathbf{R}_r \mathbf{n}(i)$ is the equivalent noise term for the rth user at the ith block. The last equality in (4.10) is obtained by applying the property of the Kronecker's product [35], i.e.,

$$(\mathbf{A} \otimes \mathbf{B})(\mathbf{D} \otimes \mathbf{G}) = (\mathbf{AD}) \otimes (\mathbf{BG}). \tag{4.11}$$

We take the case of 4 multiple access users as an example. Define $\boldsymbol{\alpha}_1 = [1,0,0,0,0]^T$, $\boldsymbol{\alpha}_2 = [0,j,0,0,0]^T$, $\boldsymbol{\alpha}_3 = [0,0,1,0,0]^T$ and $\boldsymbol{\alpha}_4 = [0,0,0,j,0]^T$. Moreover, $\boldsymbol{\beta}_1 = [1,1,0,0,0]$,

$\boldsymbol{\beta}_2 = [0,-j,-j,0,0]$, $\boldsymbol{\beta}_3 = [0,0,1,1,0]$ and $\boldsymbol{\beta}_4 = [0,0,0,-j,-j]$. Note that with the definition of vector $\boldsymbol{\alpha}$, the multiplication of the transmission matrix $\mathbf{T}_m, m = 1,\cdots,M$ with the mth user's transmitted data block $\mathbf{x}_m(i)$ effectively shifts the transmitted data block of the mth user to the corresponding mth position in the superblock, which essentially leads to a TDMA transmission scheme, where each user occupies a different block interval in the composite superblock, as shown in Fig. 4.2. The last block in a superblock is always zero, which is equivalent to padding zeros at the end of the Mth user data.

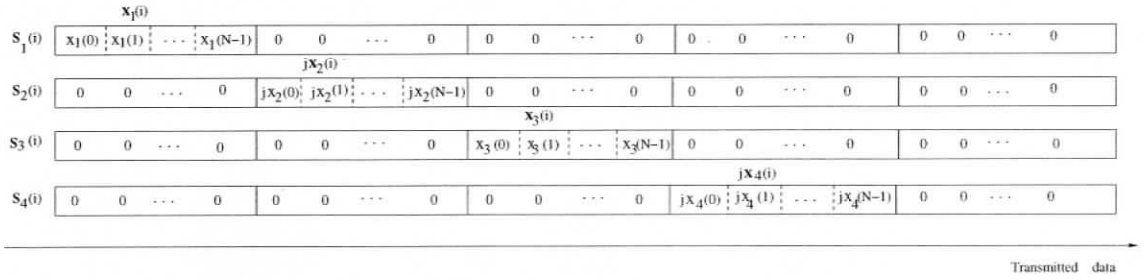

Figure 4.2. *superblock structure*

From the definitions of $\boldsymbol{\alpha}_m$ and $\boldsymbol{\beta}_r (m, r = 1,\cdots,M)$, it is straightforward to show that the following results apply

$$\mathrm{Re}\{\boldsymbol{\beta}_r \boldsymbol{\alpha}_m\} = \begin{cases} 1 & \text{for } r = m \\ 0 & \text{for } r \neq m \end{cases}. \tag{4.12}$$

Furthermore, we have

$$\mathrm{Re}\{\boldsymbol{\beta}_r \mathbf{J}_{M+1} \boldsymbol{\alpha}_m\} = \begin{cases} 1 & \text{for } r = m \\ 0 & \text{for } r \neq m \end{cases} \tag{4.13}$$

and

$$\boldsymbol{\beta}_r \mathbf{L}_{M+1} \boldsymbol{\alpha}_m = 0 \quad \text{for all } r \text{ and } m \in \{1,\cdots,M\}. \tag{4.14}$$

Taking the real part of $\mathbf{u}_r(i)$, MAI free reception is achieved by (4.12) and (4.13), and (4.14) guarantees IBI free. Applying (4.12)-(4.14) to (4.10), we have

$$\begin{aligned} \mathbf{v}_r(i) &= \left[\overline{\mathbf{H}}_{r,L} + \overline{\mathbf{H}}_{r,U}\right] \mathbf{x}_r(i) + \mathrm{Re}\{\boldsymbol{\xi}_r(i)\} \\ &= \tilde{\mathbf{H}}_r \mathbf{x}_r(i) + \boldsymbol{\eta}_r(i) \qquad r = 1,\cdots,M \end{aligned} \tag{4.15}$$

where $\boldsymbol{\eta}_r(i) = \mathrm{Re}\{\boldsymbol{\xi}_r(i)\}$ is the equivalent white Gaussian noise term before FFT. Eqn. (4.15) shows how MAI free and IBI free reception is achieved by separating multiple users from the superposition of the received signals without inserting CP.

Since multiple users are determinately separated at the receiver, the subsequent data detection follows that of the single user, where frequency-domain equalization are performed to remove ISI within each block. After FFT, frequency-domain equalization and IFFT, the detected data becomes

$$\begin{aligned} \hat{\mathbf{x}}_r(i) &= \mathrm{sgn}(\mathrm{Re}\{\mathbf{z}_r(i)\}) \\ &= \mathrm{sgn}\left(\mathrm{Re}\{\mathbf{F}^H\mathbf{C}_r\Lambda_r\mathbf{F}\mathbf{x}_r(i) + \mathbf{F}^H\mathbf{C}_r\mathbf{F}\boldsymbol{\eta}_r(i)\}\right) \end{aligned} \tag{4.16}$$

where the last equality comes from (4.15) and the decomposition of the circulant matrix in (4.6). For each user, the error probability of the proposed BPSK modulated SC-FDE system can be obtained by using exactly the same method as in the single user case, since multiple users are completely separated at the receiver. The error probability of the proposed SC-FDE TDMA over UWB channels is simply the error probability of each user averaged over the total number of users. Note that the receiver matrix multiplication in (4.10) results in an enhanced noise variance in the effective noise term compared to the single user case, where each element in $\boldsymbol{\eta}_r(i) = \mathrm{Re}\{\mathbf{R}_r\mathbf{n}(i)\}$ is a white Gaussian R.V. with variance N_0, due to the fact that each element in $\boldsymbol{\eta}_r(i)$ is the real part of the addition of two complex white Gaussian noise with variance $\frac{N_0}{2}$ in both real and imaginary part. Therefore, the proposed TDMA system will suffer around 3 dB performance degradation compared to the BER performance of the ideal single user transmission with no IBI and perfect channel estimation.

4.3.2 Transmitter and Receiver Matrix Design

In this subsection, we illustrate how the transmitter and receiver matrices are designed for an arbitrary number of users, which is equivalent to designing the vectors $\boldsymbol{\alpha}_m$ and $\boldsymbol{\beta}_m$ $(m = 1, \cdots, M)$. To achieve the MAI-free and IBI-free communication, $\boldsymbol{\alpha}$ and $\boldsymbol{\beta}$ must

satisfy the properties listed in (4.12)-(4.14), which can be designed iteratively as follows. First, we define $\boldsymbol{\alpha}_1$ as a length $M+1$ column vector, with its first element being 1 and the others being zero. To satisfy (4.12), the first element in $\boldsymbol{\beta}_1$ has to be 1. The second element in $\boldsymbol{\beta}_1$ has to be assigned as 1 too since the product of the left shifted version of $\boldsymbol{\beta}_1$ and $\boldsymbol{\alpha}_1$ is also 1, as stated in (4.13).

Now, since the second element of $\boldsymbol{\beta}_1$ is 1, the second element in other $\boldsymbol{\alpha}_i$, $i = 2, \cdots, M$ can only be either an imaginary number as j, $-j$ or 0. Otherwise, MAI will occur. Choose the second element in $\boldsymbol{\alpha}_2$ as j. In order for $\boldsymbol{\beta}_2$ and $\boldsymbol{\alpha}_2$ to satisfy (4.12) and (4.13), the second and third element in $\boldsymbol{\beta}_2$ should be assigned as $-j$. To avoid MAI from the second user, the third element in other $\boldsymbol{\alpha}$ should be a real number either 1 or 0. Choose $\boldsymbol{\alpha}_3$ as $[0,0,1,0,\cdots,0]^T$ to satisfy (4.12) and (4.13) and the third and fourth element in $\boldsymbol{\beta}_3$ have to be 1. Therefore vector $\boldsymbol{\beta}_3$ is obtained, and so on.

The vector is designed iteratively until the Mth $\boldsymbol{\alpha}$ vector, where the second to last element in $\boldsymbol{\alpha}_M$ is either j or 1, and the last two elements in $\boldsymbol{\beta}_M$ is $-j$ or 1, correspondingly. If we choose $\boldsymbol{\alpha}_{M+1}$ as the column vector with its last element as j or 1, it is impossible to find the corresponding $\boldsymbol{\beta}_{M+1}$ with its left shifted version yielding a non-zero component with $\boldsymbol{\alpha}_{M+1}$. This explains why a length $M+1$ vector has to be utilized to accommodate M users and achieve the MAI free reception. The penalty in bandwidth efficiency, however, is still less than the insertion of CP in the block spread CDMA [33], which will be discussed in Section 4.4.

We further notice that since the last element in all $\boldsymbol{\alpha}_m$, $m = 1, \cdots, M$ is zero, the third requirement (4.14) for vector design is automatically satisfied. Therefore, the vectors that satisfy (4.12)-(4.14) are obtained iteratively. Or, they can simply be chosen as

$$\boldsymbol{\alpha}_m = \begin{cases} \mathbf{q}_m & \text{for odd } m,\ m = 1, \cdots, M \\ j\mathbf{q}_m & \text{for even } m,\ m = 1, \cdots, M \end{cases} \tag{4.17}$$

where $\mathbf{q}_m$ denotes the length $M+1$ column vector with its mth element being 1 and 0

elsewhere. Similarly,

$$\boldsymbol{\beta}_m = \begin{cases} \mathbf{p}_m & \text{for odd } m,\ m = 1,\cdots,M \\ (-j)\mathbf{p}_m & \text{for even } m,\ m = 1,\cdots,M \end{cases} \tag{4.18}$$

where $\mathbf{p}_m$ denotes the length $M+1$ row vector with its mth and $(m+1)$th element being 1, and 0s elsewhere.

Following the definition of $\boldsymbol{\alpha}$ and the transmitter matrix $\mathbf{T}_m$, an intuitive way to illustrate the proposed multiple access system is to regard it as a TDMA system, where the received block data of each user occupies an individual block in the received superblock.

4.3.3 TDMA SC-FDE with Diversity Combining

It has been shown in Chapter 2 that performance gain can be obtained by utilizing the oversampling diversity scheme. The matched filter output of each user can be oversampled at time instants $kT_c + t_d,\ d = 0,1,\cdots,D-1, k = 0,1,\cdots,N-1$ and $0 < t_d < T_c$, where T_c is the chip duration and D is the number of oversampling diversity branches. Assume timing offsets t_d are chosen to yield the best possible performance. Multiple branches of the received signal in one symbol are hence obtained. The performance of the TDMA SC-FDE under UWB channels applying the oversampling diversity is simulated in Section 4.4, where a performance gain of around 4 dB relative to that without oversampling diversity can be obtained in the multiple access UWB system.

4.4 Simulation Results and Discussions

4.4.1 Performance Comparison between the Proposed TDMA Scheme and CDMA in UWB Communications

The performance of the proposed time division multiple access system for the BPSK modulated block transmission over UWB channels is presented in this section, compared with

that of the CDMA scheme in [33]. For details of the block spreading CDMA scheme, please refer to [33] and [34]. The proposed multiple access SC-FDE system is illustrated in Fig. 4.1, where the RRC pulse with roll off factor of 0.5 is used as the pulse shaping filter. The composite received data is then fed to the receiver of each user and sampled at the optimal timing, respectively. After separated from other users, the subsequent signal processing is identical for all users in both the TDMA and CDMA system, where FFT, frequency-domain MMSE equalization and IFFT are employed.

The UWB channels used are CM1-CM4 channel models proposed by the IEEE 802.15.3a study group [2], where the channel delay spread varies from 30 ns to 120 ns for CM1 to CM4. Same as in Chapter 2, the transmitted pulse shaping filter, the receiver matched filter and one of the 100 channel realizations for a particular UWB channel model are convolved to form 100 different equivalent channel realizations over which the BERs are averaged. The BER performance of the multiple access system is then obtained by averaging the BER of each user over the number of users. In the simulation, we assume that each user experiences different propagation channels. For example, in the 4 user case, users 1 to 4 undergo channels CM1 to CM4, respectively.

We present the performance of the proposed TDMA scheme with different number of users in Figs. 4.3-4.4, compared with that of the CDMA system [33] at an effective data rate of 100 Mbps for each user over the UWB propagation environment, with and without 3-branch oversampling diversity. For fair comparison, both the TDMA and CDMA systems have the same system complexity by using an FFT size of 128. The simulation results are obtained by using 32 CP for the CDMA system, while no CP is inserted between blocks for the proposed TDMA system. At the low SNR range and with smaller number of users, CDMA outperforms TDMA because our TDMA scheme doubles the noise variance as discussed in Section 4.3.1. At high SNR, it can be observed that error floors occur in the CDMA scheme due to insufficient CP, while the proposed TDMA scheme does not suffer from IBI induced error floors. The performance advantage of the TDMA scheme over CDMA becomes more obvious with larger number of users. With an increasing number

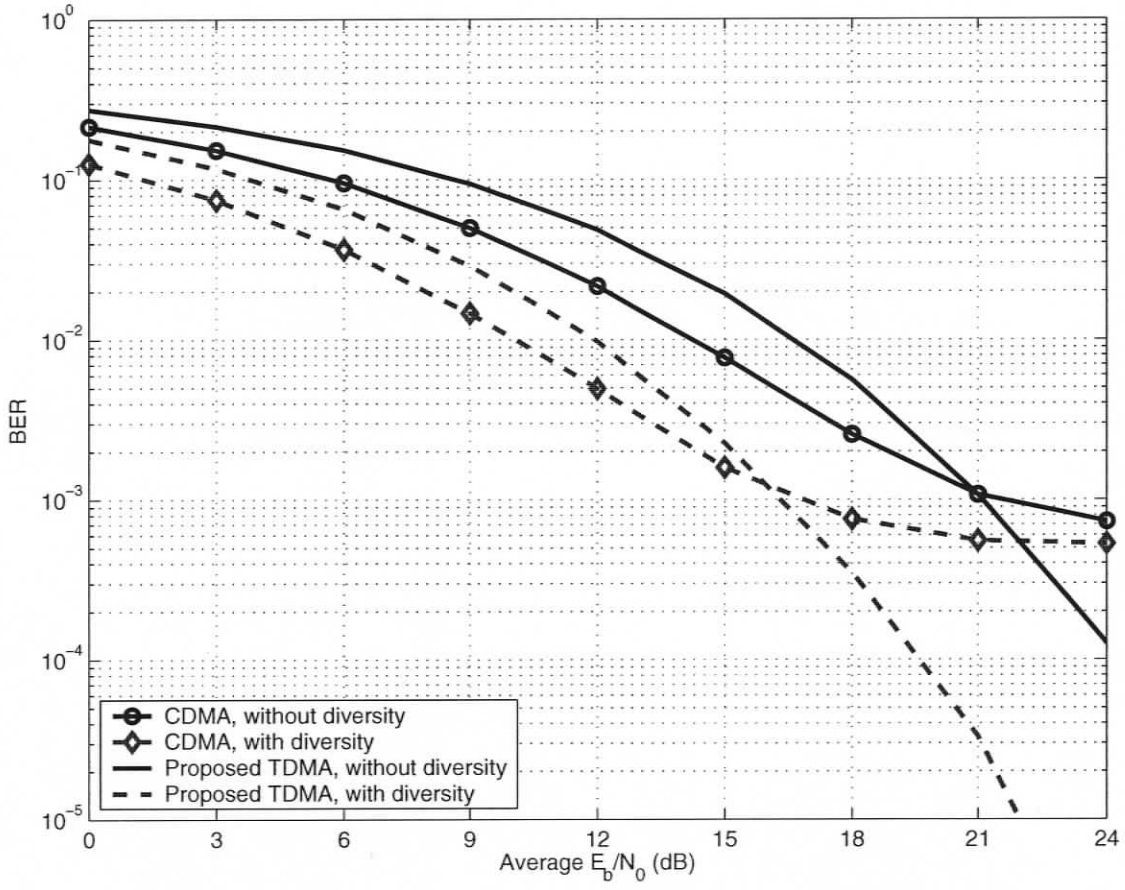

Figure 4.3. *BER Performance of the proposed TDMA system with 4 users at an effective data rate of* 100 *Mbps for each user, where CM1, CM2, CM3, CM4 are assigned to users 1-4, respectively.*

of the accommodated users higher than 4, severe performance degradation occurs in the CDMA scheme due to the increased chip rate. The performance gap between CDMA and TDMA at low SNR is reduced and the proposed TDMA system shows less performance degradation when the number of users increases. This is due to the IBI-free reception and higher bandwidth efficiency of TDMA, which will be explained in the next subsection. Furthermore, although both systems demonstrate pronounced performance gains by utilizing the oversampling diversity scheme, the error floor at high SNRs in the CDMA scheme cannot be suppressed.

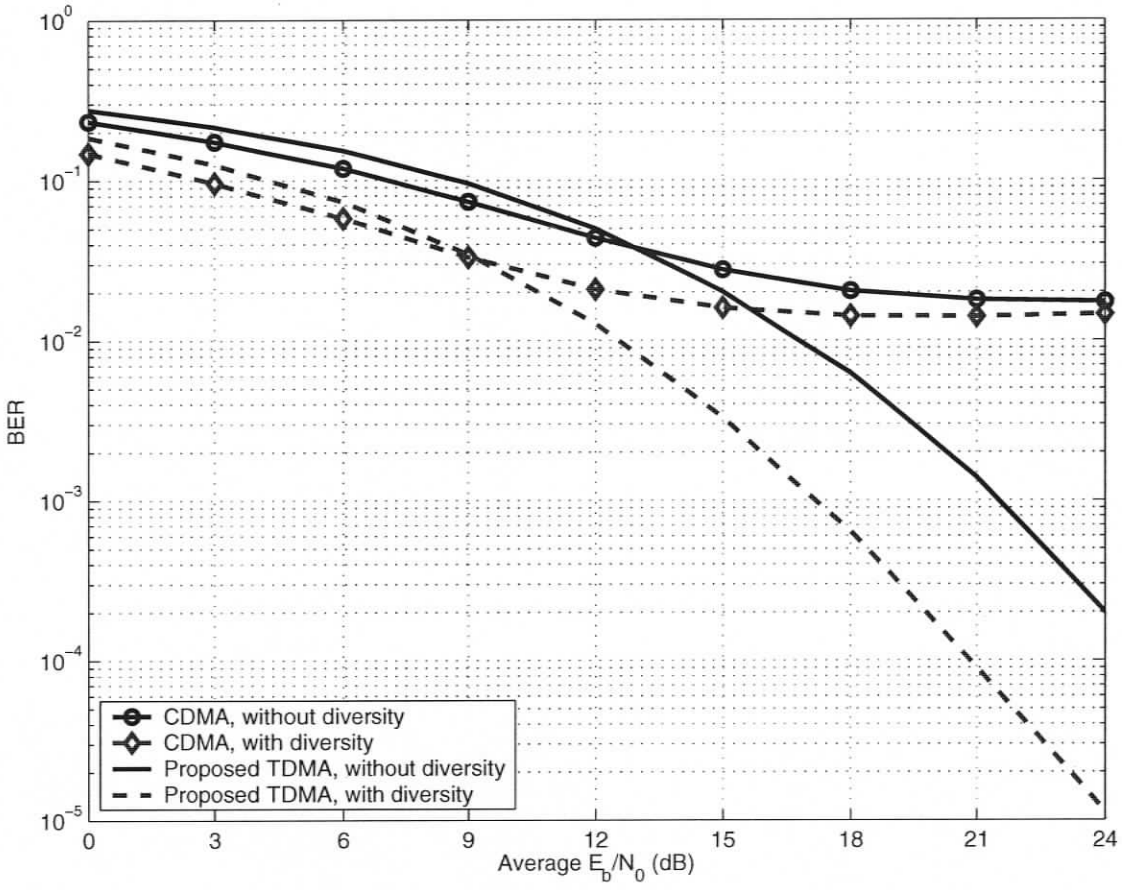

Figure 4.4. *BER Performance of the proposed TDMA system with 7 users at an effective data rate of* 100 *Mbps for each user, where CM1, CM2, CM3, CM4, CM4, CM3, CM2 are assigned to users 1-7, respectively.*

In Fig. 4.5, the impact of imperfect channel estimation on the performance of the proposed TDMA scheme with 4 users is presented, where the low complexity LMMSE frequency-domain channel estimation in Chapter 3 is employed. The generation of optimal and non-optimal pilots also follows that in Chapter 3, where ideal flat spectrum of constant ones are used for the optimal pilots and the non-optimal pilots are randomly generated BPSK signals. Using 2 optimal pilot blocks or 3 non-optimal blocks, the estimation of channel attenuation factors are obtained from the averaged pilot blocks. It can be seen that for 4 users with imperfect channel estimation, a performance degradation of less than 1 dB

can be observed by using 2 optimal pilots while the performance degradation of around 2 dB occurs when 3 non-optimal pilots are utilized. Furthermore, similar performance degradation due to imperfect channel estimation has been observed for other numbers of users in our simulation.

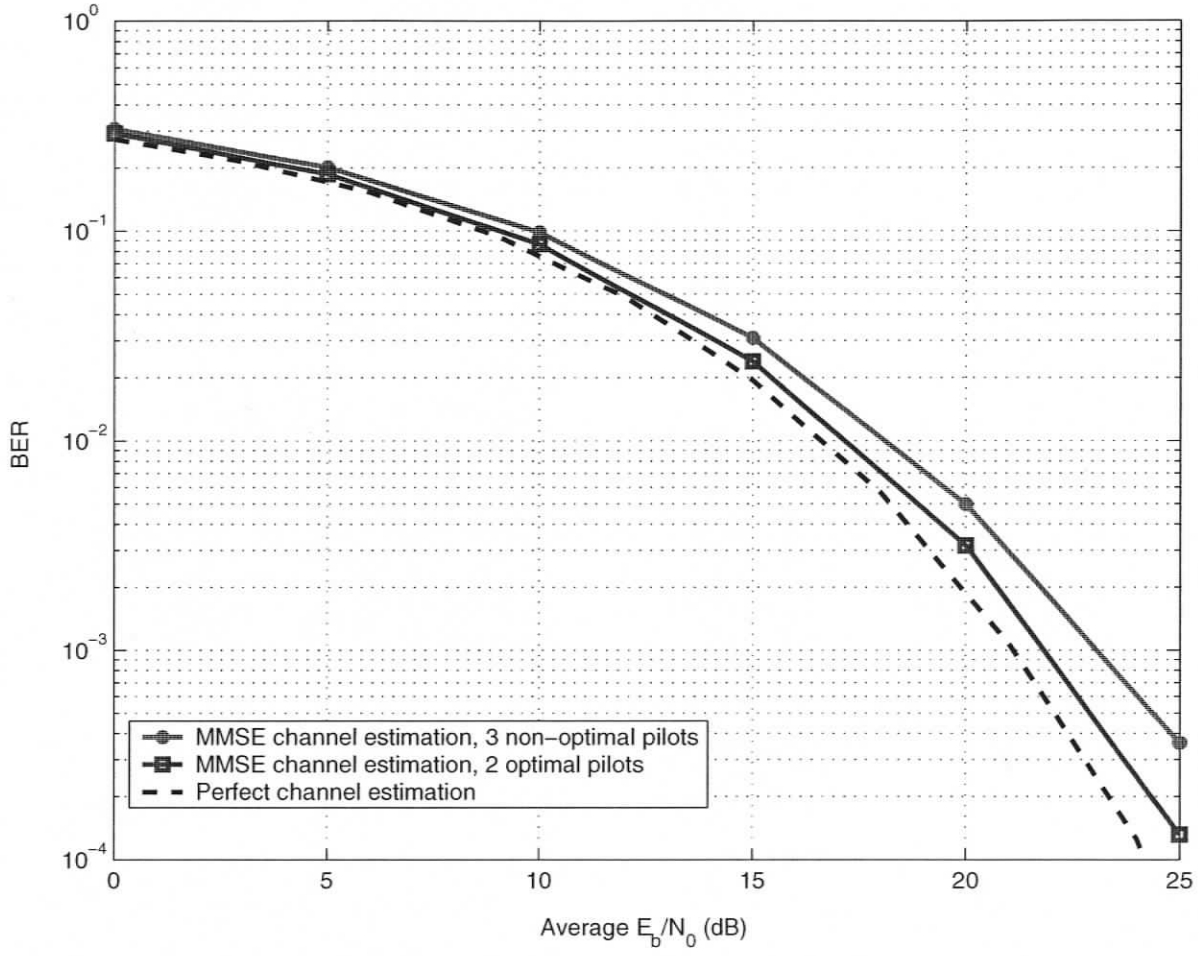

Figure 4.5. *Impact of imperfect channel estimation on the performance of the proposed TDMA system with 4 users at an effective data rate of* 100 *Mbps for each user.*

4.4.2 Data Rate and Bandwidth Efficiency

Considering the block spread CDMA system with 4 users, to achieve an effective data rate of 200 Mbps for each user, a corresponding chip rate of 1 Gbps is required (the CP length is assumed to be $1/4$ of the block length, as in most practical cases). The recommended CP length of 32 is therefore a lot shorter than required to combat the channel delay spread for UWB channels CM3 or CM4, where the channel impulse response spreads for more than 120 ns, thus resulting in severe performance degradation. The proposed TDMA system, at an effective data rate of 200 Mbps and chip rate of 1000 Mbps (since a vector length of 5 is required to accommodate 4 users), can still yield reasonable BER performance without obvious error floors, as in Fig. 4.6.

When bandwidth efficiency of the proposed TDMA system is considered, a length $(M+1)N$ data stream is needed to transmit data for M users, each of which contains N information bits. The bandwidth efficiency of the proposed multiple access system can therefore be obtained as $E_1 = \frac{MN}{(M+1)N} = \frac{M}{M+1}$. The block spread CDMA system, however, has a bandwidth efficiency of $E_2 = \frac{N}{N+L}$ [33], where L is the required length of CP. Again taking the 4 user case as an example, when the length of L is chosen as $1/4$ of the block length, $E_1 = E_2 = 4/5$. Note that for both systems, chip rate has to be increased to accommodate an increased number of users. In the CDMA system, to maintain the same BER performance for more users, a larger number of CP has to be utilized as chip rate increases, and therefore bandwidth efficiency E_2 decreases. For the proposed TDMA system, however, the bandwidth efficiency E_1 increases with the number of users. Therefore, the proposed multiple access SC-FDE system is more suitable to accommodating larger number of users at a high system data rate.

4.5 Summary

A novel MAI-free IBI-free TDMA scheme for BPSK modulated, SC-FDE block transmission over IEEE 802.15.3a UWB channels has been proposed. Relying on matrix manip-

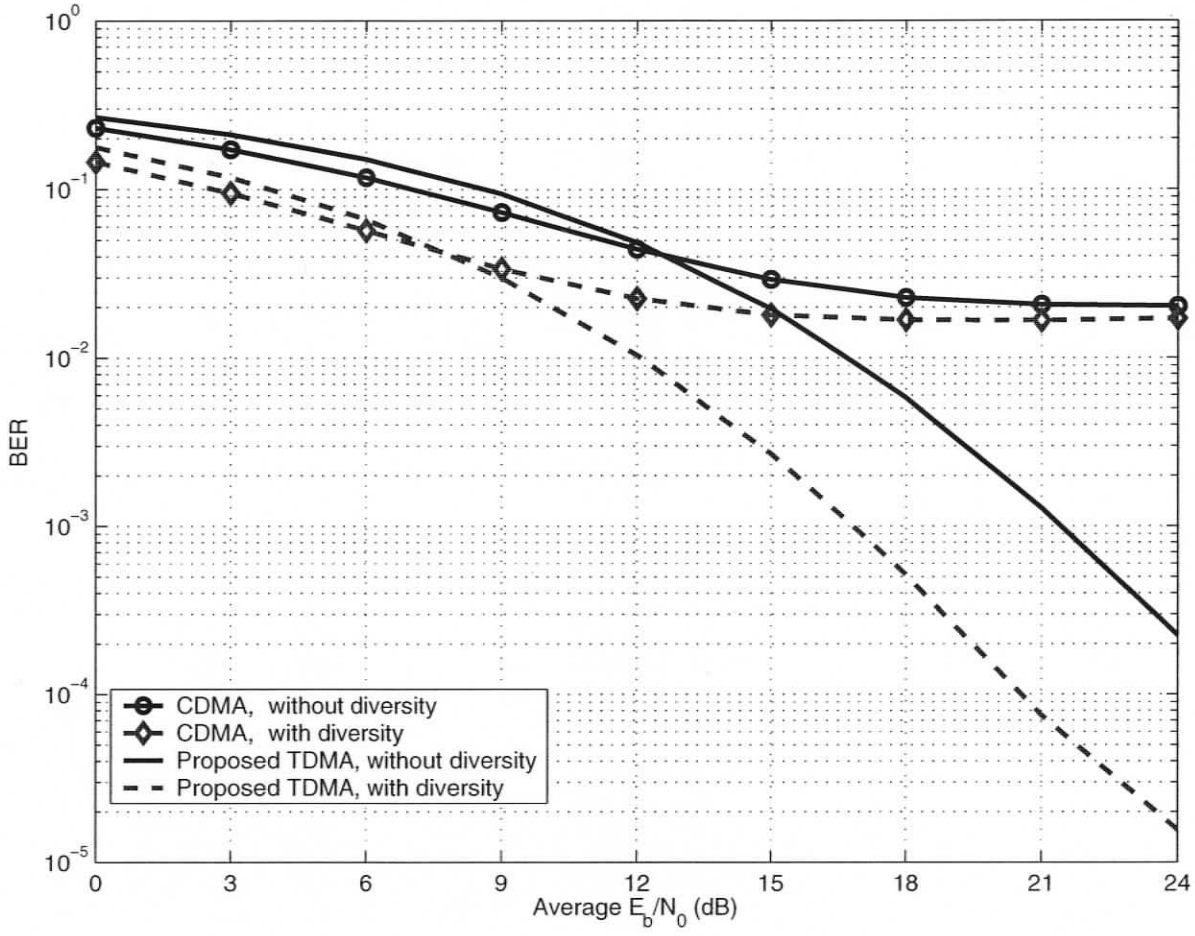

Figure 4.6. *BER Performance of the proposed TDMA system with 4 users at an effective data rate of* 200 *Mbps for each user.*

ulation, in addition to MAI free reception, the proposed TDMA scheme does not require the insertion of CP between blocks to eliminate IBI. Therefore higher bandwidth efficiency can be achieved with possibly smaller FFT size. Simulation results of the performance of the proposed TDMA scheme for BPSK modulated SC-FDE system under IEEE 802.15.3a UWB channel models CM1-CM4 have been presented and compared with that of the block spread CDMA system [33]. The impact of imperfect channel estimation on the performance of the proposed multiple access scheme has also been investigated, where both the optimal and non-optimal pilot blocks are considered. Effective data rate and bandwidth

efficiency of the proposed TDMA scheme have been discussed and compared with that of the block spread CDMA. Our results show that the proposed TDMA scheme is more effective in high speed UWB communications to accommodate larger number of users, while keeping a low system complexity.

Chapter 5

Spectrum Shaping and NBI Suppression in UWB Communications

5.1 Background

In order to avoid interfering with existing narrowband or wideband devices, FCC has restricted the power emission of a UWB transmission to a maximum PSD of -41.3 dBm/MHz in the range of 3.1 GHz to 10.6 GHz [1]. Although this PSD mask can effectively suppress UWB interference to most existing systems operating at frequencies lower than 3 GHz (GPRS, GSM 900, GPS, W-CDMA and bluetooth), there still exist devices which operate in the ultra-wide spectrum allocated for UWB communications, resulting in mutual interference to both systems. For example, it has been shown that UWB systems that meet the FCC guidelines can greatly impact the performance of an IEEE 802.11a WLAN system working in NLOS environments [36]. On the other hand, the 802.11a WLAN system, operating at the 5.2 GHz frequency band, will also impact the performance of the UWB system [36]. Therefore, it is of great importance to consider the coexistence of UWB systems and existing narrowband or wideband systems in an attempt to limit interference between these systems.

This problem is addressed in the current UWB proposals to the IEEE 802.15.3a by simply avoiding use of the 802.11a WLAN frequency band. MB-OFDM divides the UWB spectrum into subbands of 528 MHz each and deactivates the subband around 5.2GHz [6],

while DS-UWB uses the portion below 5.2 GHz as the preliminary step and the upper portion above 5.2 GHz as the second step [5].

In addition to the above mentioned schemes to address coexistence problems, spectral notching is another method that can be used to limit the interference between a UWB system and existing narrowband devices. This approach potentially provides greater flexibility regarding the generation of spectral nulls at interfering frequencies, which has become even more important in view of the recently proposed "detect and avoid" mandate of Japanese frequency regulators [37]. In this method, UWB pulses are designed such that their spectra have a null at the operating frequency of the victim device [38, 39]. In [38], eigenvalue decomposition was used and was shown to effectively generate spectral nulls at the required frequency band. However, this method involves formation and eigenvalue decomposition of a matrix with dimension as high as 128. In [39], the problem was formulated as finding a pulse with a spectrum that meets the FCC mask with maximum energy while also having a null at the required frequency band. The resulting transmitted pulse is a filtered monocycle, where the impulse response of the FIR filter is the sum of delta functions with different time delays and different weighting factors. Although this approach yields an accurate approximation to the pre-defined spectrum shaping, the spectrum fitting algorithm involves a nonlinear optimization process using neural networks algorithms. In [40], a digital FIR filter approach to synthesizing UWB pulses that satisfy the spectral mask were proposed. In this chapter, we propose a different method to address the UWB spectrum shaping issue. The design scheme avoids the complications of nonlinear optimization in [39] and the large number of coefficients in [40], with only a small loss in the admissible transmission power. For example, the gain of the transmission power from nonlinear optimization is around 0.7 dB compared to the 5th derivative Gaussian monocycle pulse without spectral nulls [39].

In this chapter, we address the UWB spectrum shaping issue from a different perspective by applying the general approach to code and pulse construction outlined in [41]. We view the transmitted pulse as a "coded" basic Gaussian monocycle pulse, where the value of each code bit gives the weighting coefficient of each monocycle pulse, and where the

code bit interval is a uniform delay equal to $\frac{1}{f_1}$ where f_1 is the desired frequency of the null. The resulting pulse is the sum of weighted and overlapping Gaussian monocycles, and therefore the shape of the resulting spectrum is determined by both the Fourier transform of the basic Gaussian monocycle and the spectrum of the designed codeword. We choose the 7th derivative of the Gaussian pulse as the basic pulse to meet the FCC outdoor mask, and leave spectrum notching to the codeword design. We design codewords such that their spectra approximates the Fourier series representation of a passband brickwall filter with a spectral null, or other filters such as Butterworth, Chebyshev, elliptical, or a spectral shape we refer to as linear. The resulting pulses have a spectral null at $f = f_1$, a frequency whose selection addresses the coexistence issue between the UWB system and narrowband devices operating within the 3-10 GHz frequency range.

We also investigate the inverse problem, the impact of the NBI at IEEE 802.11a WLAN frequency band on the performance of UWB systems. We take SC-FDE UWB systems as an example. Other than using the root raised cosine pulse as the transmitter pulse shaping filter as in Chapter 2, we use the coded Gaussian monocycle with frequency null at 5.2 GHz, developed by the code design scheme in this chapter. However, the transmitter pulse shaping design and spectrum notching scheme outlined in this chapter can also be applied to other UWB systems including DS-UWB.

The chapter is organized as follows. Section 5.2 derives the PSD of a transmitted signal and elaborates on the codeword design method which introduces spectral nulls at predefined frequencies. Section 5.3 presents the spectral results for pulses designed to have spectral nulls at one or more interference frequency bands. In addition, the performance of the SC-FDE UWB system using the monocycle coded pulse in the presence of NBI at 802.11a band is simulated and compared with that of an uncoded SC-FDE UWB system using a single Gaussian monocycle. Our results demonstrate that the SC-FDE system using our coded pulse design can effectively suppress NBI and yield improved BER performance compared to the uncoded system. Section 5.4 concludes this chapter.

5.2 Pulse Spectrum and Codeword Design

Consider a BPSK modulated system for UWB communications where the serial transmitted data $\mathbf{x} = [x_0, x_1, \cdots, \cdots]^T$ are shaped by the transmitter pulse shaping filter, and transmitted over the UWB channel.

In this system, the transmitter pulse shaping filter is a weighted sum of the basic Gaussian monocycle pulse $p(t)$, which we express as

$$c_p(t) = \sum_{m=0}^{M-1} c_m p(t - m\tau_c) \tag{5.1}$$

where the c_m are the weighting coefficients and τ_c is a delay which is uniform for each c_m. Values of c_m and τ_c must be pre-determined to achieve the designed spectral shaping. After BPSK modulation, the transmitted signal becomes

$$v(t) = \sum_{n=-\infty}^{\infty} x_n \sum_{m=0}^{M-1} c_m p(t - m\tau_c - nT_s) \tag{5.2}$$

where T_s is the duration of each symbol which is an integer multiple of τ_c. It can be written

$$T_s = (M-1)\tau_c + T_p + T_z \tag{5.3}$$

where T_p is the duration of the basic Gaussian monocycle pulse and T_z, $0 \leq T_z < \tau_c$, is the length of time the coded pulse has value zero at the end of each symbol interval in order to ensure that T_s is a multiple of τ_c.

Our objective in this chapter is to design the transmitted UWB pulse to meet the FCC spectrum mask and at the same time ensure the presence of spectral nulls at specified frequency bands in order to suppress mutual interference between this UWB system and existing narrowband devices.

In the following, we present an expression for the spectrum of the transmitted signal and the methodology for designing the codeword weights c_m ($m = 0, 1 \cdots, M-1$) to ensure that the transmitted signal fits the FCC mask and has spectral nulls at interference frequency bands. From a coding perspective, the transmitter pulse shaping filter in eq. (5.1) can be

considered a "coded" version of the basic Gaussian monocycle pulse, where the codeword is $\mathbf{c} = [c_0, c_1, \cdots, c_{M-1}]$ of length M. Each code bit interval τ_c is uniform and can be any pre-defined length. In this chapter, we use τ_c with length less than the duration of the basic Gaussian monocycle T_p, therefore, the transmitted pulse is composed of overlapping Gaussian monocycles weighted by the code coefficients. In the text that follows, we refer to this transmitted pulse with spectral nulls introduced through codeword design as the monocycle coded pulse, and the corresponding UWB system as the monocycle coded UWB system. Following derivation of the PSD of a cyclostationary process as outlined in [20], we present the PSD expression of the coded transmitted signal for the completeness of the chapter and convenience of later illustration.

5.2.1 Spectrum of the Monocycle Coded UWB Pulse

The auto-correlation function of $v(t)$ in (5.2) can be written as

$$\begin{aligned}
\Phi_{vv}(t, t+\tau) &= \mathbb{E}\{v(t)v^*(t+\tau)\} \\
&= \sum_{n_1=-\infty}^{\infty} \sum_{n_2=-\infty}^{\infty} \mathbb{E}\{x_{n_1} x_{n_2}^*\} \sum_{m_1=0}^{M-1} \sum_{m_2=0}^{M-1} c_{m_1} c_{m_2} p(t - m_1\tau_c - n_1 T_s) p(t + \tau - m_2\tau_c - n_2 T_s) \\
&= \sum_{n_1=-\infty}^{\infty} \sum_{u=-\infty}^{\infty} \Phi_{xx}(u) \sum_{m_1=0}^{M-1} \sum_{m_2=0}^{M-1} c_{m_1} c_{m_2} p(t - m_1\tau_c - n_1 T_s) p(t + \tau - m_2\tau_c - n_1 T - u T_s)
\end{aligned} \tag{5.4}$$

where Φ_{xx} is the autocorrelation of $\mathbf{x}$ and a change of variable $u = n_2 - n_1$ is made in the last equality. This summation is periodic in t with period T_s, therefore, $\Phi_v v(t, t+\tau)$ is also periodic in t with period T_s. Furthermore, since v(t) has zero mean and periodic auto-correlation function $\Phi_v v(t, t+\tau)$, it is a wide-sense cyclostationary stochastic process. The

averaged auto-correlation function $\overline{\Phi}_{vv}(\tau)$ can then be calculated as

$$\begin{aligned}\overline{\Phi}_{vv}(\tau) &= \frac{1}{T_s}\int_0^{T_s}\Phi_{vv}(t,t+\tau)dt \\ &= \frac{1}{T_s}\int_0^{T_s}\sum_{m_1=0}^{M-1}\sum_{m_2=0}^{M-1}c_{m_1}c_{m_2}\sum_{n_1=-\infty}^{\infty}\sum_{u=-\infty}^{\infty}\Phi_{xx}(u) \\ &\quad p(t-m_1\tau_c-n_1T_s)p(t+\tau-m_2\tau_c-n_1T_s-uT_s)dt.\end{aligned} \tag{5.5}$$

The PSD of $v(t)$ can be obtained by evaluating the Fourier transform of $\overline{\Phi}_{vv}(\tau)$ as

$$\begin{aligned}P_v(f) &= \int_{-\infty}^{\infty}\overline{\Phi}_{vv}(\tau)e^{-j2\pi f\tau}d\tau \\ &= \frac{1}{T_s}\sum_{m_1=0}^{M-1}\sum_{m_2=0}^{M-1}c_{m_1}c_{m_2}\int_{-\infty}^{\infty}e^{-j2\pi f\tau}\sum_{u=-\infty}^{\infty}\Phi_{xx}(u) \\ &\quad \times\sum_{n_1=-\infty}^{\infty}\int_0^{T_s}p(t-m_1\tau_c-n_1T_s)p(t+\tau-m_2\tau_c-n_1T_s-uT_s)dtd\tau \\ &= \frac{1}{T_s}\sum_{m_1=0}^{M-1}\sum_{m_2=0}^{M-1}c_{m_1}c_{m_2}\int_{-\infty}^{\infty}e^{-j2\pi f\tau}\sum_{u=-\infty}^{\infty}\Phi_{xx}(u) \\ &\quad \sum_{n_1=-\infty}^{\infty}\int_{n_1T_s}^{(n_1+1)T_s}p(t-m_1\tau_c)p(t+\tau-m_2\tau_c-uT_s)dtd\tau \\ &= \frac{1}{T_s}\sum_{m_1=0}^{M-1}\sum_{m_2=0}^{M-1}c_{m_1}c_{m_2}\int_{-\infty}^{\infty}e^{-j2\pi f\tau}\sum_{u=-\infty}^{\infty}\Phi_{xx}(u)\int_{-\infty}^{\infty}p(t-m_1\tau_c)p(t+\tau-m_2\tau_c-uT_s)dtd\tau \\ &= \frac{1}{T_s}\sum_{m_1=0}^{M-1}\sum_{m_2=0}^{M-1}c_{m_1}c_{m_2}e^{j2\pi f(m_1-m_2)\tau_c}\sum_{u=-\infty}^{\infty}\Phi_{xx}(u)e^{-j2\pi fuT_s} \\ &\quad \int_{-\infty}^{\infty}p(t-m_1\tau_c)e^{-j2\pi f(t-m_1\tau_c)}dt\int_{-\infty}^{\infty}p(t+\tau-m_2\tau_c-uT_s)e^{-j2\pi f(t+\tau-m_2\tau_c-uT_s)}d\tau \\ &= \frac{1}{T_s}\sum_{m_1=0}^{M-1}\sum_{m_2=0}^{M-1}c_{m_1}c_{m_2}e^{j2\pi f(m_1-m_2)\tau_c}|P(f)|^2P_x(f) \\ &= \frac{1}{T_s}P_c(f)|P(f)|^2P_x(f)\end{aligned} \tag{5.6}$$

where $|P(f)|^2$ is the energy spectral density (ESD) of the basic Gaussian monocycle $p(t)$, $P_x(f)=\sum_{u=-\infty}^{\infty}\Phi_{xx}(u)\exp(-j2\pi fuT_s)$ is a Fourier transform of $\Phi_{xx}(u)$, and $P_c(f)$ is the

spectrum of the codeword **c**, written as

$$\begin{aligned} P_c(f) &= \sum_{m_1=0}^{M-1}\sum_{m_2=0}^{M-1} c_{m_1}c_{m_2}e^{j2\pi f(m_1-m_2)\tau_c} \\ &= \mathbf{V}\mathbf{c}^H\mathbf{c}\mathbf{V}^H \\ &= (c_0^2+\cdots+c_{M-1}^2)+2(c_0c_1+\cdots+c_{M-2}c_{M-1})\cos(2\pi f\tau_c) \\ &\quad +\cdots+2c_0c_{M-1}\cos(2(M-1)\pi f\tau_c) \end{aligned} \tag{5.7}$$

where $\mathbf{V}=\left[1,e^{-j2\pi f\tau_c},e^{-j4\pi f\tau_c},\cdots,e^{-j2(M-1)\pi f\tau_c}\right]$. The second equality is an expression for the spectrum of the codeword **c** which agrees with the result for the spectrum of a block coded digital signal in [42]. The spectrum $P_c(f)$ is periodic with period $f_c=\frac{1}{\tau_c}$, and for real-valued c_m, is symmetric about $f=0$ and is therefore symmetric about multiples of $\frac{f_c}{2}=\frac{1}{2\tau_c}$. Since $P_c(f)$ is a PSD, it is also non-negative.

The PSD of the transmitted UWB signal $v(t)$ can therefore be considered as the product of three parts: the spectrum of the codeword $P_c(f)$, the ESD of the analog Gaussian monocycle $p(t)$, and the PSD of the transmitted sequence **x**. Note that when the transmitted symbols are equiprobable and independent RV, $P_x(f)=E_b$. Our methodology in this chapter is to choose a $p(t)$ that fits the FCC spectrum mask, and design $P_c(f)$ to generate nulls in $P_v(f)$ at specified frequencies.

5.2.2 Codeword Design to Generate a Spectral Null at One Particular Frequency

Our objective in this subsection is to design a codeword **c** that will result in a spectral null at a desired frequency f_1, as shown in Fig. 5.1. In this figure, the solid line is the ideal brickwall spectral shape and the dashed line is a "linear" spectral shape that will be elaborated upon below.

As outlined in [41], these ideal spectral shapes can serve as desired prototype shapes which $P_c(f)$ is designed to approximate. It follows from (5.7) that $P_c(f)$ can be represented

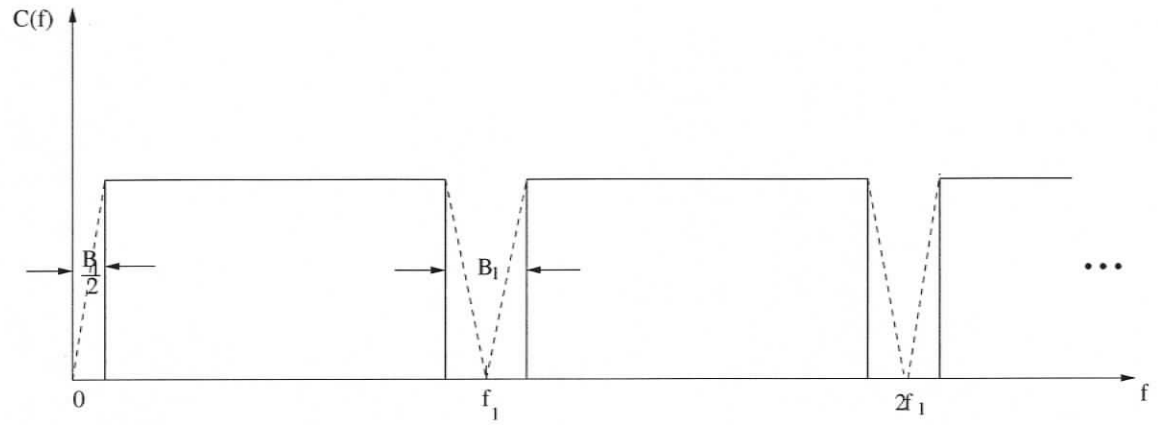

Figure 5.1. *Desired codeword spectra*

by M terms of a cosine Fourier series, that is,

$$P_c(f) = a_0 + 2\sum_{n=1}^{M-1} a_n \cos(2\pi n f \tau_c) \tag{5.8}$$

where a_n are the Fourier coefficients of $P_c(f)$, given by

$$a_n = \tau_c \int_f P_c(f)\cos(2\pi n f \tau_c) df \quad \text{for } n = 0, \cdots, M-1, \tag{5.9}$$

and integration is over any period of $P_c(f)$. We wish to obtain a codeword $\mathbf{c}$ such that $P_c(f)$ has a spectral null at the frequency f_1. Since $P_c(f)$ is periodic with period $1/\tau_c$, introducing a null at frequency f_1 will lead to nulls at frequencies $f_1 + k/\tau_c$, where $k \in \mathbb{I}$. Assume that the codeword $\mathbf{c}$ is real valued, the even symmetry of $P_c(f)$ will also result in nulls at frequencies $-f_1 + k/\tau_c$, $k \in \mathbb{I}$. For example, if we choose the period of $P_c(f)$ to be 5 GHz, introducing a null at 5.2 GHz will also yield nulls at 4.8 GHz, 9.8 GHz and 10.2 GHz within the UWB operating frequency of 3.1-10.6 GHz. However, if we choose the code bit interval τ_c such that $1/\tau_c = f_1$, where f_1 is the center frequency of the null, there will be nulls only at frequencies kf_1, $k \in \mathbb{I}$. Designing $P_c(f)$ to have a null at DC ($f = 0$) with (one-sided) bandwidth $\frac{B_1}{2}$ will also yield a null with bandwidth B_1 at frequencies kf_1, which includes the designed frequency f_1. For example, to generate a spectral null at the IEEE 802.11a WLAN operating frequency of 5.2 GHz, we choose the code bit interval to be $\tau_c = 1/(5.2 \times 10^9) = 0.1923$ ns. Designing $P_c(f)$ to have a spectral null at DC will yield

a spectrum with a null occurring at $f_1 = 5.2$ GHz and one extra null in the UWB frequency band at $2f_1 = 10.4$ GHz.

Following the general approach in [41], we now illustrate the design of the codeword in detail. We first consider design of the codeword to approximate the ideal passband brickwall filter as an example to illustrate the idea of codeword design; subsequent practical filter responses are arrived at by attempting to approximate the brickwall characteristic. As discussed above, to generate a null at f_1 with bandwidth B_1, the bandwidth of the null at $f = 0$ should be $\frac{B_1}{2}$. Substituting $P_c(f)$ in (5.9) with the brickwall spectrum, the Fourier coefficients of $P_c(f)$ that approximates the brickwall spectrum with $M-1$ coefficients can be easily calculated as

$$a_n = -\frac{1}{\pi n}\sin(\pi n \tau_c B_1) \text{ for } n = 1, 2, \cdots, M-1, \tag{5.10}$$

and in order to ensure that the DC value is as small as possible while also ensuring that $P_c(f)$ is non-negative, a_0 can be evaluated as the minimum value such that the sum in (5.8) is non-negative.

By equating the coefficients in (5.7) and (5.8), we have the following set of equations:

$$c_0^2 + c_1^2 + \cdots + c_{M-1}^2 = a_0 \tag{5.11}$$

$$c_0 c_1 + c_1 c_2 + \cdots + c_{M-2} c_{M-1} = a_1 \tag{5.12}$$

$$c_0 c_2 + c_1 c_3 + \cdots + c_{M-3} c_{M-1} = a_2 \tag{5.13}$$

$$\vdots$$

$$c_0 c_{M-1} = a_{M-1}. \tag{5.14}$$

Given the values of a_n, $n = 1, 2, \cdots, M-1$, instead of evaluating a_0 separately as noted above, it is possible to minimize (5.11) under the constraint of (5.12)-(5.14). To do so, define the function $g(\mathbf{c})$ as

$$\begin{aligned} g(\mathbf{c}) \;=\; & c_0^2 + c_1^2 + \cdots + c_{M-1}^2 + \lambda_1 (c_0 c_1 + c_1 c_2 + \cdots + c_{M-2} c_{M-1} - a_1) \\ & + \lambda_2 (c_0 c_2 + c_1 c_3 + \cdots + c_{M-3} c_{M-1} - a_2) + \cdots \\ & + \lambda_{M-1} (c_0 c_{M-1} - a_{M-1}) \end{aligned} \tag{5.15}$$

where $\lambda_1, \lambda_2, \cdots, \lambda_{M-1}$ are the Lagrange multipliers. The following set of equations then applies:

$$\frac{\partial g(\mathbf{c})}{\partial c_0} = 2c_0 + \lambda_1 c_1 + \lambda_2 c_2 + \cdots + \lambda_{M-1} c_{M-1} = 0 \tag{5.16}$$

$$\frac{\partial g(\mathbf{c})}{\partial c_1} = 2c_1 + \lambda_1 c_0 + \lambda_1 c_2 + \cdots + \lambda_{M-2} c_{M-2} = 0 \tag{5.17}$$

$$\vdots$$

$$\frac{\partial g(\mathbf{c})}{\partial c_{M-1}} = 2c_{M-1} + \lambda_1 c_{M-2} + \lambda_2 c_{M-3} + \cdots + \lambda_{M-1} c_0 = 0. \tag{5.18}$$

The coefficients of the required codeword $\mathbf{c}$ can be obtained by solving $\lambda_1, \cdots, \lambda_{M-1}$ and $c_0, \cdots, c_{M-1}$ from (5.12)-(5.14) and (5.16)-(5.18).

5.2.3 Codeword Design for Different Spectrum Shapings

It is known that using an insufficient number of Fourier coefficients to represent a continuous function leads to distortions, including in this case ripples in the passband and a larger than desired transition band. Using additional Fourier coefficients will yield a more accurate approximation of the desired spectrum, at the expense of a longer codeword and increased complexity in evaluation of the codeword coefficients. Alternatively, to obtain a better approximation of the desired spectrum, instead of increasing the number of Fourier coefficients, we consider approximation of different bandpass spectrum shapes with a larger transition band, including shapes given by the Butterworth, Chebyshev and elliptical filters. The codeword design method follows the steps outlined above, except that the Fourier coefficients vary with different spectrum shapes. The codeword coefficients which generate a spectral null at the IEEE 802.11a frequency band of 5.2 GHz are obtained numerically by solving eqs. (5.12)-(5.14) and (5.16)-(5.18). In addition to the DC term a_0, we use four Fourier coefficients a_1-a_4 when approximating the desired spectrum, therefore $P_c(f)$ includes the DC, 1^{st}, 2^{nd}, 3^{rd} and 4^{th} harmonic components, resulting in a code length of $M = 5$. The normalized codeword coefficients are tabulated in Table 5.1, where f_o denotes

the normalized cutoff frequency of the corresponding lowpass filter and n denotes the order of the Butterworth, Chebyshev and elliptical filters. In this design, the Chebyshev and elliptical filters have $R_p = 0.5$ dB peak-to-peak ripple in the passband and R_s denotes the stopband attenuation (in dB) from the peak passband value for the elliptical filters. The resulting spectra are plotted and discussed in Section 5.3.

We also consider a simple design in which the prototype spectrum falls linearly to zero at f_1 (referred to as "linear" in Table 5.1 and plotted as the dashed line in Fig. 5.1). It can be verified that the Fourier coefficients for this prototype spectrum are given by

$$a'_n = \frac{1}{\pi n}\sin(\pi n \tau_c B_1) + \frac{1}{B_1 \pi^2 n^2 \tau_c}\cos(\pi n \tau_c B_1) - \frac{1}{B_1 \pi^2 n^2 \tau_c} - \frac{1}{\pi n}\sin(\pi n \tau_c B_1). \tag{5.19}$$

Applying these coefficients to eqs. (5.12)-(5.14) and (5.16)-(5.18), the required codeword can be obtained. The codeword coefficients obtained when $B_1 = 0.2$ GHz are given in Table 5.1.

5.2.4 Pulse Design to Generate Spectral Nulls at Multiple Interference Frequency Bands

The pulse design scheme presented above is focused on the generation of a spectral null at one particular frequency band. Here we extend the design method to the generation of UWB pulses with spectral nulls at multiple interference bands. Suppose we want to design a UWB pulse with spectral nulls at interference frequencies f_1 and f_2. We could attempt to approximate a spectrum with nulls at these frequencies and evaluate codeword coefficients as outlined above. Alternatively, using the methodology in subsection 5.2.2, we can design two codewords $\mathbf{c_1}$ and $\mathbf{c_2}$ with spectral nulls at f_1 and f_2, respectively, using code bit intervals $\tau_1 = \frac{1}{f_1}$ and $\tau_2 = \frac{1}{f_2}$. The effect of convolving these two monocycle coded pulses in the time domain is the multiplication of their spectra in the frequency domain, which will yield spectral nulls at f_1 and f_2 simultaneously. In Section 5.3 we present a spectrum with two spectral nulls designed by this approach.

5.3 Simulation Results and Discussion

Spectra with a null at the IEEE 802.11a frequency of 5.2 GHz are presented in this section, based on the codeword design scheme discussed in the previous section. A spectrum with nulls at multiple interference frequencies is also presented. The BER performance of one example UWB system, SC-FDE UWB, using the monocycle coded Gaussian pulse in the presence of narrowband interference at 802.11a frequency band is simulated and compared with that of uncoded system utilizing a single basic Gaussian monocycle.

5.3.1 Spectra of Monocycle Coded UWB Pulses

We choose the basic monocycle as the 7th derivative of the Gaussian pulse, given by

$$p(t) = \left(\frac{105t}{\sigma^9} - \frac{105t^3}{\sigma^{11}} + \frac{21t^5}{\sigma^{13}} - \frac{t^7}{\sigma^{15}} \right) \exp\left(-\frac{t^2}{2\sigma^2} \right) \tag{5.20}$$

where σ is chosen as 0.064 ns to meet the FCC spectrum mask; any other pulse which meets the FCC spectrum mask could also be used. In Fig. 5.2, we present the transmitter pulse generated by coding this monocycle with the $M = 5$ codeword $\mathbf{c} = [0.461, 0.487, -0.691, 0.014, -0.270]$, obtained by approximating the brickwall filter when $B_1 = 0.1$ GHz. In this example, the duration of the basic Gaussian monocycle, $p(t)$, is designed as 0.7692 ns and τ_c is selected to be 0.1923 ns, resulting in a symbol duration T_s of 1.5384 ns. Note that values of τ_c, T_p and T_s that contain some approximation or quantization errors can be adopted for easy implementation. For example, $\tau_c = 0.19$ ns will result in a null centered at 5.263 GHz which, given the width of the null, will limit interference with 802.11 devices. Furthermore, if we allow for the case when a symbol has value zero for some duration of time (T_z) following the last monocycle pulse as shown in eq. (5.3), the selection of T_p and T_s can be more flexible and not require as high accuracy as the values provided above. For example, we can use $T_p = 0.8$ ns, $T_s = 1.71$ ns and $T_z = 0.15$ ns.

The normalized PSD of the designed coded monocycle pulse is presented in Fig. 5.3, based on the assumption that the transmitted symbols are equiprobable and independent

of each other. For comparison, the PSD that results when $B_1 = 1$ GHz is also shown, as is the FCC outdoor mask and the ESD of the basic Gaussian monocycle $|P(f)|^2$. It can be observed that the coded monocycle transmitter pulses meet the FCC outdoor mask and that a null is present at the specified interference frequency of 5.2 GHz. As a result of the periodicity of $P_c(f)$, a null is also present at 10.4 GHz. Also, passband ripples can be observed due to an insufficient number of Fourier coefficients, which can be suppressed by approximating bandpass filter types other than the brickwall spectrum shape.

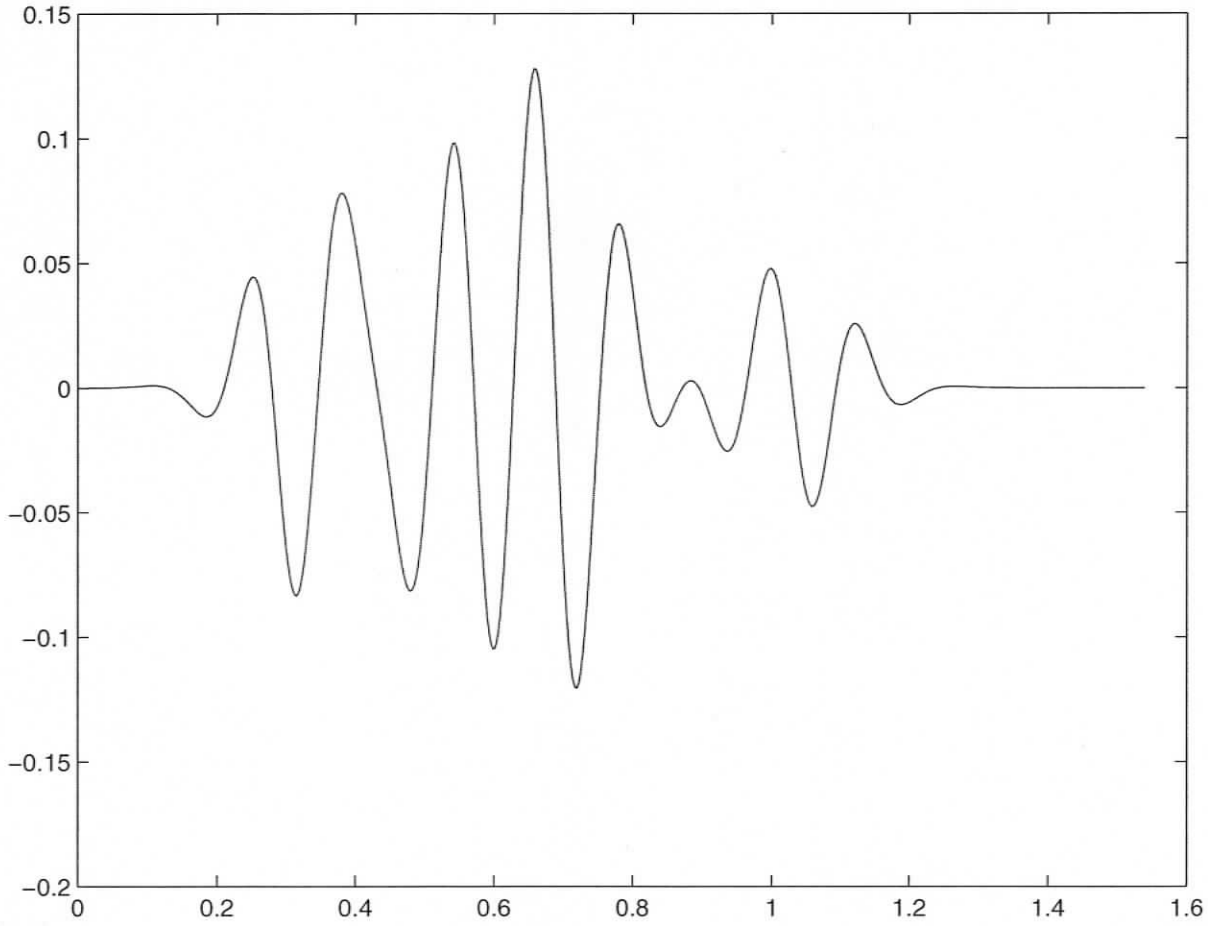

Figure 5.2. *The transmitted pulse for coded monocycle UWB with codeword* $\mathbf{c} = [0.461, 0.487, -0.691, 0.014, -0.270]$.

To illustrate the effects of different filter types, in Fig. 5.4 we plot the spectra generated

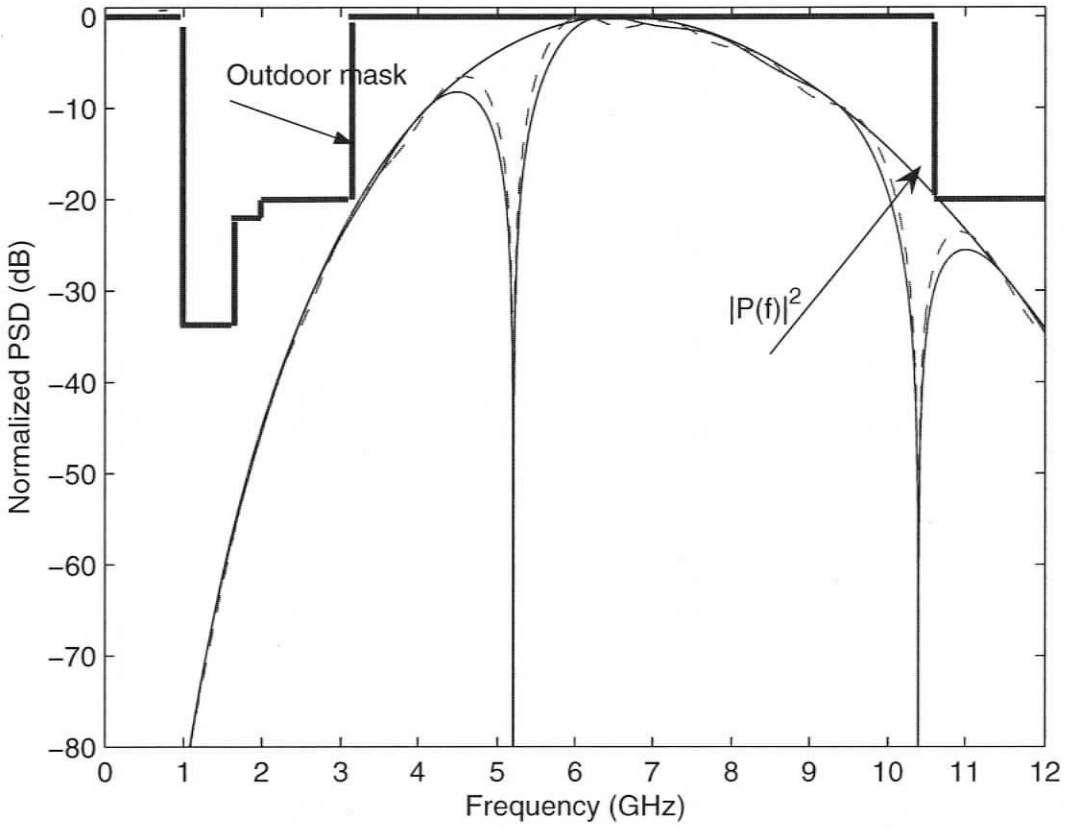

Figure 5.3. *FCC outdoor spectrum mask, the ESD of the basic Gaussian monocycle* $|P(f)|^2$ *and the normalized PSD of the coded monocycle UWB pulse with codeword* $\mathbf{c} = [0.461, 0.487, -0.691, 0.014, -0.2700]$ *(*B_1*=0.1 GHz, dashed line) and* $\mathbf{c} = [0.093, 1.075, -0.683, -0.322, -0.168]$ *(*B_1*=1 GHz, solid line), respectively.*

using codewords tabulated in Table 5.1. It can be observed that among these spectra, approximating the linear and the Chebyshev filters yields less passband ripple. Note that the spectrum shaping of the Chebyshev and elliptical filters varies with the parameters R_p and R_s. Furthermore, although the passband ripple differs significantly with different bandpass filter types, the width and depth of the null does not. Our results also show that, due to the limited degree of freedom provided by five codeword coefficients, the different values of B_1 considered when generating the results for this figure have little effect on the resulting

spectrum.

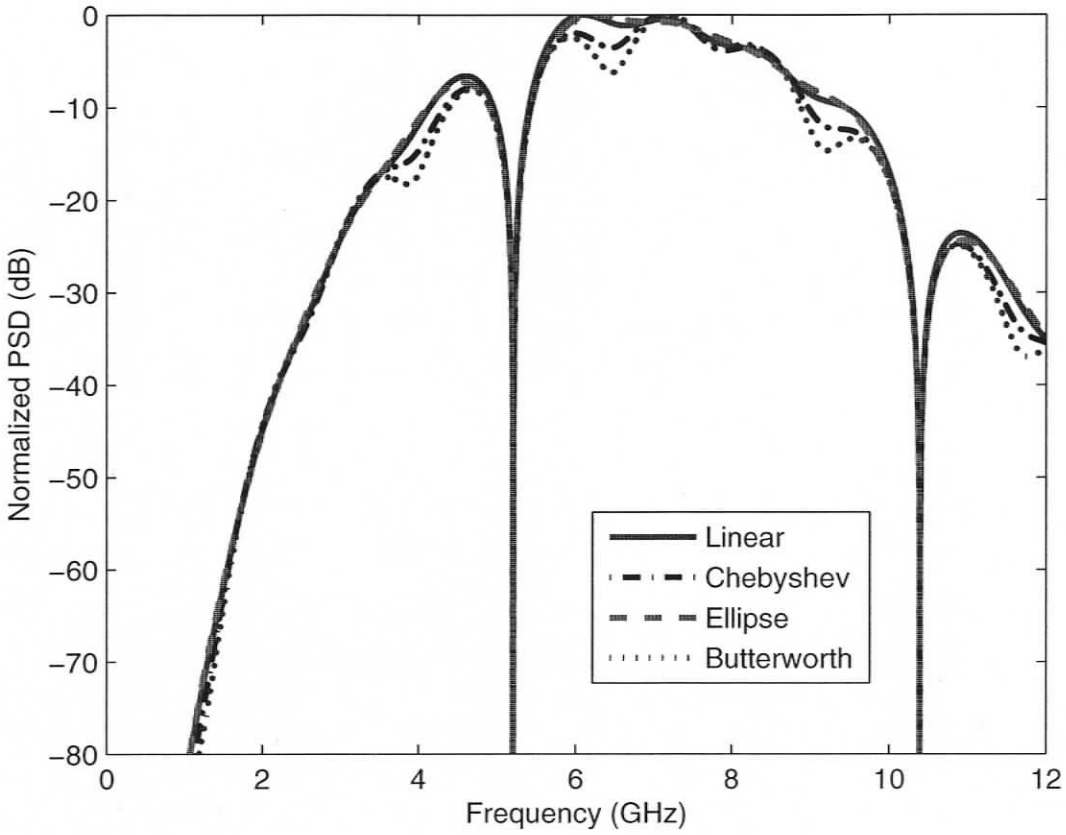

Figure 5.4. *Spectra of the coded monocycle pulses obtained by approximating different filter types.*

In Fig. 5.5, we present a spectrum with nulls at two interference frequencies by using the method discussed in subsection 5.2.4. The nulls are designed to be at frequencies $f_1 = 5.2$ GHz and $f_2 = 6.8$ GHz, with $\mathbf{c}_1 = [0.461, 0.487, -0.691, 0.014, -0.270]$ for 5.2 GHz and $\mathbf{c}_2 = [0.304, -0.106, -0.084, -0.065, -0.048]$ for 6.8 GHz, respectively. It can be observed that the convolution of the two coded monocycle pulses, each with a single null at one particular frequency, can effectively generate a transmitter pulse shape with nulls at both interference frequency bands. Note that the resulting transmitter pulse shape obtained by convolution will have a longer pulse duration, leading to a reduced system data rate.

Table 5.1. *codewords for different spectrum shapes*

Filter Shape	c_0	c_1	c_2	c_3	c_4
Brickwall $B_1 = 0.1$ GHz	0.461	0.487	-0.691	0.014	-0.270
Brickwall $B_1 = 1.0$ GHz	0.093	1.075	-0.683	-0.322	-0.168
Butterworth $B_1 = 0.2$ GHz, $n = 5$ and $f_0 = 0.981$	0.858	-0.401	-0.018	-0.159	-0.279
Chebyshev $B_1 = 0.1$ GHz, $n = 5$ and $f_0 = 0.990$	0.340	0.601	-0.699	-0.063	-0.179
Ellipse $B_1 = 0.1$ GHz, $n = 5$, $f_0 = 0.990$ and $R_s = 100$ dB	0.529	0.321	-0.666	0.188	-0.373
Linear $B_1 = 0.2$ GHz	0.887	-0.311	-0.247	-0.190	-0.140

This effect, however, can be compensated by reducing the codeword length or the duration of the basic Gaussian monocycle.

5.3.2 Performance of coded monocycle SC-FDE UWB

In this subsection, SC-FDE UWB is taken as an example to evaluate the performance of a UWB system using the proposed coded monocycle pulse in the presence of NBI. SC-FDE is a communication scheme where data are transmitted block-by-block in the time domain while equalization is performed in the frequency domain. After pulse shaping and matched filtering the transmitted blocks of data, the SC-FDE system evaluates an FFT to transform the received signal into the frequency domain. Frequency domain equalization is then performed to suppress inter-symbol interference. The equalized signal is transformed back into the time domain by an IFFT operator, and finally detection is carried out in the time domain. For a detailed description of SC-FDE, please refer to Chapter 2.

To demonstrate the advantage of using a coded monocycle pulse, the performance of this SC-FDE system in the presence of NBI is simulated and compared to that of the SC-FDE system using a single Gaussian pulse. The performance of both systems is evaluated for a block length of 256 and a CP length of 64. The coded monocycle SC-FDE utilizes the coded monocycle pulse shown in Fig. 5.2 with $T_s = 1.5384$ ns and code-

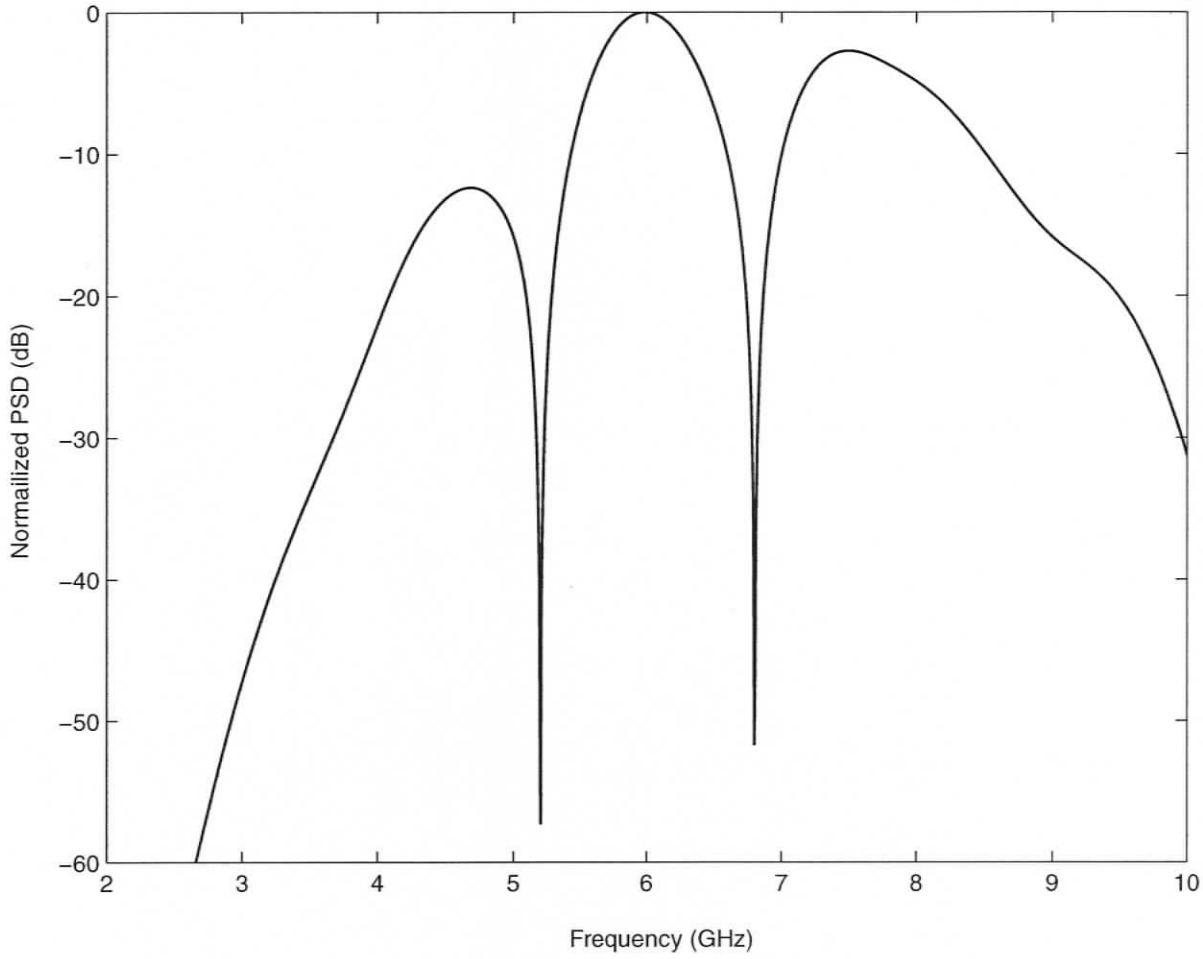

Figure 5.5. *Normalized PSD of the coded monocycle UWB pulse with spectral nulls at frequencies* 5.2 *GHz and* 6.8 *GHz, resulting from the convolution of pulses generated by* $\mathbf{c}_1 = [0.461, 0.487, -0.691, 0.014, -0.270]$ *for 5.2 GHz and* $\mathbf{c}_2 = [0.304, -0.1063, -0.084, -0.065, -0.048]$ *for 6.8 GHz, respectively.*

word $\mathbf{c} = [0.461, 0.487, -0.691, 0.014, -0.270]$, where these codeword coefficients were obtained by approximating the brickwall filter. Very similar performance was obtained with all the codewords in Table 5.1. The uncoded SC-FDE system uses the single 7th derivative of the Gaussian monocycle $p(t)$ given in (5.20) as the transmit pulse, with a pulse duration of 0.7692 ns and a symbol duration of 1.5384 ns. The UWB channels used are the CM1-CM4 channel models proposed by the IEEE 802.15.3a study group [2], where

the channel will spread more than 100 symbol durations with a delay spread from 25 ns to 150 ns in CM1 to CM4, respectively. Severe ISI will therefore be introduced, which can be combated by the frequency domain equalization scheme in the SC-FDE system. At the receiver, the received signal is fed into the demodulator that is matched to the transmitter pulse shaping filter. After sampling with optimal timing, the subsequent signal processing is identical for both systems. Since the designed coded monocycle pulse has a spectral null at the interference frequency, its convolution with the matched filter also results in a spectral null at this frequency, therefore NBI is effectively suppressed.

In Figs. 5.6-5.9, we consider the effects of NBI on the coded monocycle SC-FDE system at an effective system data rate of 520 Mbps, compared with the performance of the uncoded SC-FDE system utilizing a single Gaussian monocycle pulse in the UWB channel models CM1-CM4. The NBI is added at the IEEE 802.11a WLAN operating frequency of 5.2 GHz, with a bandwidth of 16.56 MHz [43] and signal-to-interference ratios of SIR $= -10$ dB, -20 dB and -30 dB. It can be observed that for the uncoded SC-FDE UWB system without spectral nulls, interference in the 802.11a frequency band can lead to a performance degradation of over 2 dB, 3 dB and 5 dB at a BER of 10^{-3} for SIR$= -10$ dB, -20 dB and -30 dB, respectively. The coded monocycle SC-FDE UWB system with a spectral null at 5.2 GHz, however, effectively suppresses the interference at 5.2 GHz such that the performance with SIR$= -10$ dB is very close to that in NBI free channels. Comparing the performance of the coded and uncoded systems in the presence of NBI reveals increased performance gains for the coded monocycle system as interference power increases, with an SNR improvement in most UWB channel models considered of over 2 dB for SIR$= -20$ dB and over 4 dB for SIR$=-30$ dB when BER$= 10^{-3}$. Also, with the same SIR value in each channel model, the performance gains of the coded monocycle system increase with increasing SNR, since NBI instead of noise dominates the performance degradation of SC-FDE systems at high SNRs. Furthermore, the coded monocycle pulse tends to yield higher performance gains in the NLOS channel with larger delay spread and multipath components (i.e., channel models CM2 and CM3) than in the line of sight (LOS)

channel condition (CM1). The reason for this lies in the fact that in NLOS channel conditions where the channel is more frequency selective, frequency domain equalizer taps typically have greater values than in less frequency selective channel conditions, resulting in enhanced NBI.

By suppressing the UWB signal in the interference band, the UWB signal will not have a detrimental effect on the performance of the narrowband system.

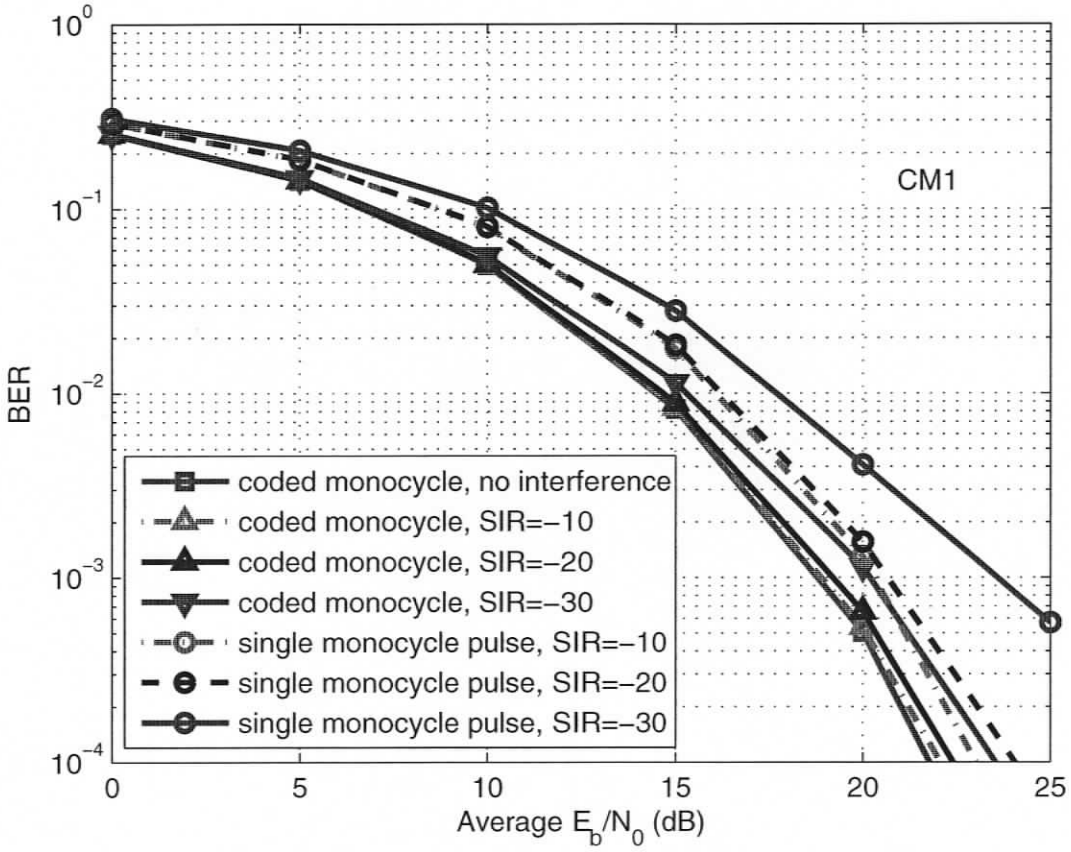

Figure 5.6. *BER of coded monocycle SC-FDE UWB and uncoded SC-FDE UWB in the presence of NBI in UWB channel model CM1.*

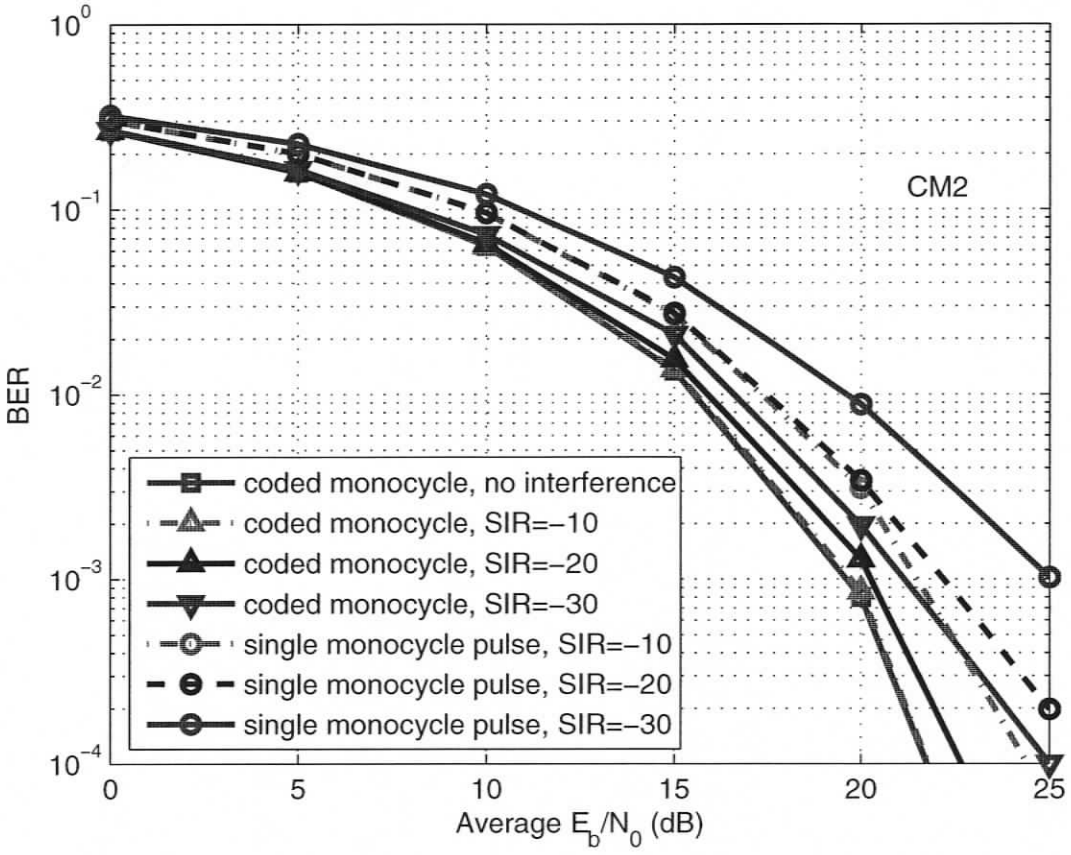

Figure 5.7. *BER of coded monocycle SC-FDE UWB and uncoded SC-FDE UWB in the presence of NBI in UWB channel model CM2.*

5.4 Summary

In this chapter, a UWB spectrum shaping scheme has been introduced and investigated. The transmitted pulse is formed as a "coded" Gaussian monocycle pulse where the codeword is obtained by approximating the Fourier series representation of the desired spectrum shaping. The resulting spectrum has been shown to fit the FCC spectrum mask and at the same time contain a spectral null at the frequency of potential NBI to effectively avoid interference at the IEEE 802.11a frequency band. Simulation results presented in this chapter show significant performance benefits of SC-FDE UWB systems using this pulse design in

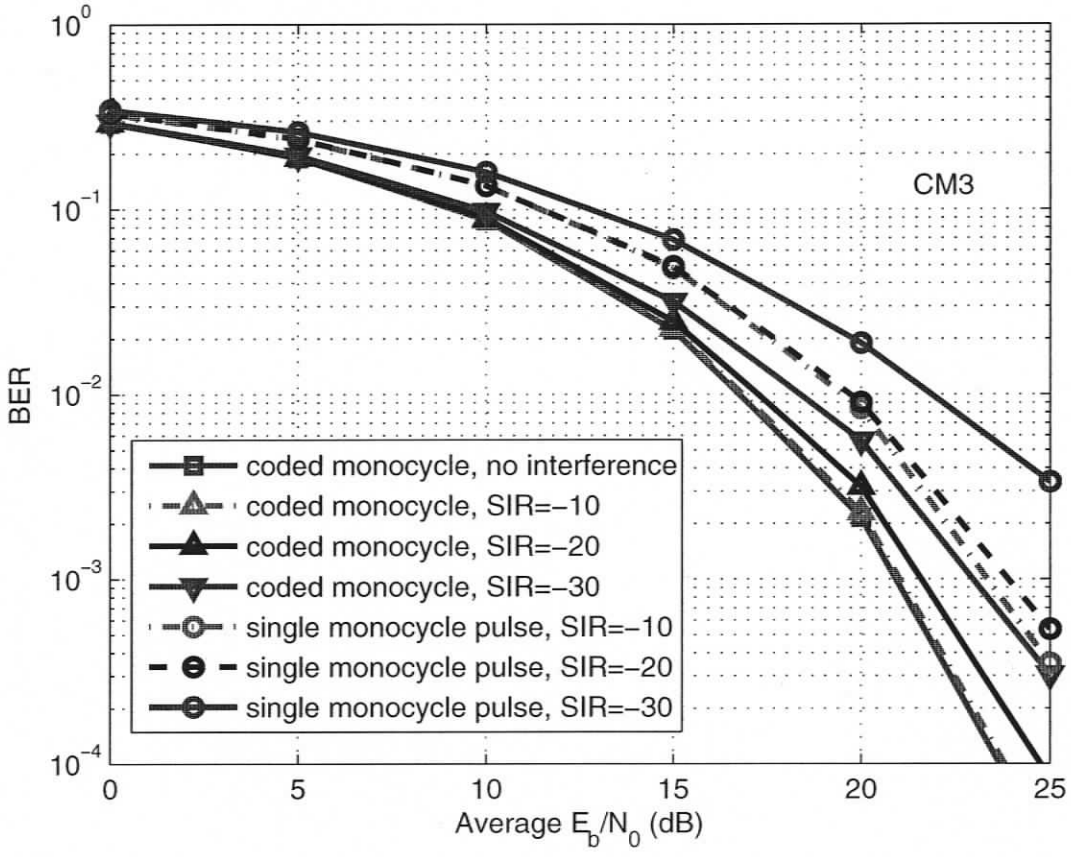

Figure 5.8. *BER of coded monocycle SC-FDE UWB and uncoded SC-FDE UWB in the presence of NBI in UWB channel model CM3.*

the presence of NBI. The code design methodology is flexible and programmable, and can generate spectral nulls at different or multiple frequencies. It can be applied to different modulation schemes including pulse position modulation, and different UWB systems including DS-UWB.

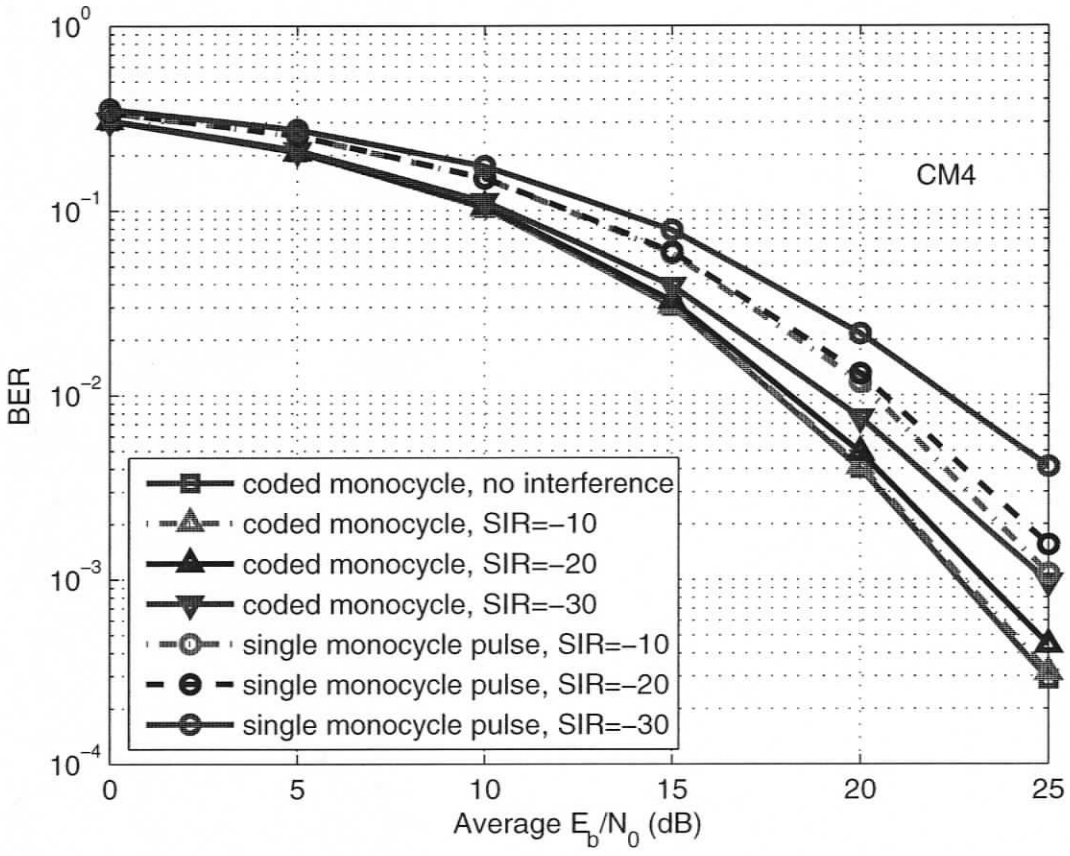

Figure 5.9. *BER of coded monocycle SC-FDE UWB and uncoded SC-FDE UWB in the presence of NBI in UWB channel model CM4.*

Chapter 6

Performance of SC-FDE System in UWB Communications with Imperfect Channel Estimation

6.1 Background

We presented the performance of SC-FDE system in Chapter 2, based on the assumption that perfect CSI can be obtained at the receiver. However, in practical cases, CSI is only available through estimation algorithms with inherent channel estimation error. Despite the practical interest and importance of evaluating the effect of channel estimation error, the BER of the SC-FDE system over UWB channels in the presence of channel estimation error has not been investigated. In this chapter, we study the BER performance of single carrier block transmission with frequency-domain MMSE equalization over UWB channels, with imperfect channel state information obtained from frequency-domain LS channel estimation algorithm.

Performance analysis of communication systems with channel estimation error is a subject of plenty research interests [44–47]. These analyses, however, were based on ISI free transmission, which cannot be applied to the SC-FDE system with frequency-domain MMSE equalization. When MMSE equalization is performed in the frequency domain while signal detection is carried out in the time domain, all the other transmitted bits within

one block will affect the detection of the current bit, resulting in complicated sums of decision variables and therefore it is not ISI free. Assuming perfect CSI, ISI was approximated as a Gaussian RV, which led to a simple and accurate analysis as in Chapter 2. In this chapter, we study the more complicated performance problem for SC-FDE systems with imperfect channel estimation in UWB channels. Our analysis starts with the derivation of the PDF of frequency-domain MMSE equalizer with channel estimation error. The BER performance of SC-FDE over UWB communications with imperfect channel estimation is then derived by employing the central limit theorem (CLT).

This chapter is organized as follows. Section 6.2 derives the PDF of the frequency-domain equalizer taps. In Section 6.3, the newly derived PDF is applied to the BER analysis of the SC-FDE system over UWB communications with channel estimation error. Numerical results and discussions are presented in Section 6.4. Section 6.5 concludes this chapter.

6.2 Probability Density Functions of the Frequency-Domain Equalizer Taps

In this section, we present the PDF of the frequency-domain MMSE channel equalizer taps with imperfect CSI, where the estimated channel attenuation factors $\hat{H}_k$ $(k = 0, \cdots, N-1)$ are obtained by frequency-domain LS channel estimation algorithms. Suppose one block of pilot symbols $\mathbf{p}$ is transmitted for channel estimation purposes. The investigated system follows that of Fig. 3.1. Following (2.4), the frequency-domain received pilot block can be rewritten as

$$\mathbf{Y} = \mathbf{PH} + \mathbf{N}_p \tag{6.1}$$

where $\mathbf{P}$ is a diagonal matrix with its kth diagonal element P_k as the kth FFT coefficient of the pilot sequences $\mathbf{p}$, and $\mathbf{N}_p = \mathbf{Fn}_p$ is a $N \times 1$ column vector with its kth element N_{p_k} being the kth FFT coefficient of the sampled noise vector of the pilot block.

The channel attenuation factors estimated by the LS algorithm can be obtained as

$$\hat{H}_k = \frac{Y_k}{P_k} = H_k + \frac{N_{p_k}}{P_k} \tag{6.2}$$

for $k = 0, 1, \cdots N-1$, and

$$N_{p_k} = \frac{1}{\sqrt{N}} \sum_{l=0}^{N-1} n_{p_l} \exp\left(-\frac{j2\pi lk}{N}\right). \tag{6.3}$$

Hence N_{p_k} is a complex Gaussian RV with zero mean and variance $\sigma_n^2 = \frac{N_0}{2}$. Furthermore, the real and imaginary parts of N_{p_k} are uncorrelated Gaussian RV with zero mean and variance $\frac{\sigma_n^2}{2} = \frac{N_0}{4}$. Denote the real and imaginary part of $\hat{H}_k$ as R_k and I_k, respectively. We have from (6.2) that R_k and I_k are uncorrelated Gaussian R.V. and $R_k \sim \mathbb{N}(H_{kr}, \frac{N_0}{4|P_k|^2})$, $I_k \sim \mathbb{N}(H_{ki}, \frac{N_0}{4|P_k|^2})$, where $\mathbb{N}(\mu, \sigma^2)$ denotes the normal distribution with mean μ and variance σ^2, and H_{kr} and H_{ki} denote the real and imaginary part of H_k, respectively.

Note that since the $\hat{H}_k$ $(k = 0, \cdots, N-1)$ are independent random variables, the C_k, $(k = 0, \cdots, N-1)$ are also independent. In the derivation that follows, we use the notation $\mu_k = \mathbb{E}[\hat{H}_k] = \mu_{kr} + j\mu_{kr}$ and $\sigma_k^2 = \mathbb{E}\left[\left|\hat{H}_k - \mu_k\right|^2\right]$. Therefore, for LS channel estimation, we have $\mu_{kr} = H_{kr}$, $\mu_{ki} = H_{ki}$ and $\sigma_k^2 = \frac{N_0}{4|P_k|^2}$.

Since the real and imaginary part of $\hat{H}_k$ are uncorrelated Gaussian, the joint PDF of R_k and I_k is given by [48]

$$f_{R_k,I_k}(R_k, I_k) = \frac{1}{2\pi\sigma_k^2} e^{-\frac{(R_k-\mu_{kr})^2+(I_k-\mu_{ki})^2}{2\sigma_k^2}}. \tag{6.4}$$

The MMSE frequency-domain equalizer taps $C_k = \frac{H_k^*}{|H_k|^2+E_b/2N_0}$ can be rewritten in polar coordinates as

$$\begin{aligned} C_k &= \frac{R_k - jI_k}{R_k^2 + I_k^2 + B} \\ &= r_k e^{j\theta_k} \end{aligned} \tag{6.5}$$

where

$$r_k = \frac{\sqrt{R_k^2 + I_k^2}}{R_k^2 + I_k^2 + B} \tag{6.6}$$

$$\theta_k = -\tan^{-1}\frac{I_k}{R_k}. \tag{6.7}$$

Or equivalently,

$$r_k \cos\theta_k = \frac{R_k}{R_k^2 + I_k^2 + B} \tag{6.8}$$

and

$$r_k \sin\theta_k = -\frac{I_k}{R_k^2 + I_k^2 + B}. \tag{6.9}$$

The joint PDF of (r_k, θ_k) can be obtained as [48]

$$f_{r_k,\theta_k}(r_k,\theta_k) = \sum_i \frac{1}{|\mathbf{J}_i|} f_{R_k,I_k}(R_{k_i}, I_{k_i}) \tag{6.10}$$

where R_{k_i} and I_{k_i} are the ith solution of (6.6) and (6.7), $|\cdot|$ denotes absolute value of the determinant $\mathbf{J}_i$ and

$$\begin{aligned}\mathbf{J}_i &= \left.\begin{vmatrix} \frac{\partial r_k}{\partial R_k} & \frac{\partial r_k}{\partial I_k} \\ \frac{\partial \theta_k}{\partial R_k} & \frac{\partial \theta_k}{\partial I_k} \end{vmatrix}\right|_{R_k=R_{k_i}, I_k=I_{k_i}} \\ &= \left.\frac{B - R_k^2 - I_k^2}{(R_k^2+I_k^2)^{1/2}(R_k^2+I_k^2+B)^2}\right|_{R_k=R_{k_i}, I_k=I_{k_i}}.\end{aligned} \tag{6.11}$$

By mathematical derivations, we solve $R_{k_i}^2 + I_{k_i}^2$ from (6.6) and (6.7) as

$$R_{k_i}^2 + I_{k_i}^2 = \frac{1 - 2Br_k^2 + (-1)^{i-1}\sqrt{1-4Br_k^2}}{2r_k^2} \tag{6.12}$$

where $i = 1, 2$, respectively. Converting to the polar coordinate form, (6.11) and (6.12) result in

$$\frac{1}{|\mathbf{J}_i|} = \frac{1}{2r_k^3\sqrt{1-4Br_k^2}}\left(1 - 2Br_k^2 \pm \sqrt{1-4Br_k^2}\right). \tag{6.13}$$

Therefore, the PDF of the kth frequency-domain channel equalizer tap can be obtained as

$$\begin{aligned} f_{r_k,\theta_k}(r_k,\theta_k) &= \frac{1}{2r_k^3\sqrt{1-4Br_k^2}}\left[1 - 2Br_k^2 + \sqrt{1-4Br_k^2}\right] f_{R_k,I_k}(R_{k_1}, I_{k_1}) \\ &\quad + \frac{1}{2r_k^3\sqrt{1-4Br_k^2}}\left[1 - 2Br_k^2 - \sqrt{1-4Br_k^2}\right] f_{R_k,I_k}(R_{k_2}, I_{k_2}) \end{aligned} \tag{6.14}$$

where $f_{R_k,I_k}(\cdot)$ is the joint PDF of the kth estimated channel attenuation factor $\hat{H}_k$ given by (6.4), which can be rewritten in the polar coordinate form as

$$f_{R_k,I_k}(r_{k_i},\theta_{k_i}) = \frac{1}{2\pi\sigma_k^2} e^{-\frac{|\mu_k|^2-B}{2\sigma_k^2}} e^{-\frac{\left(1\pm\sqrt{1-4Br_k^2}\right)\left(1-2|\mu_k|r_k\cos(\theta_k+\varphi_k)\right)}{4\sigma_k^2 r_k^2}} \tag{6.15}$$

where $|\mu_k|$ and φ_k are the norm and phase of μ_k, respectively.

Applying (6.15) to (6.14), the joint density of (r_k,θ_k) can be obtained in closed-form as

$$\begin{aligned} f_{r_k,\theta_k}(r_k,\theta_k) &= \frac{1}{4\pi\sigma_k^2} e^{-\frac{|\mu_k|^2-B}{2\sigma_k^2}} \times \frac{1}{r_k^3\sqrt{1-4Br_k^2}} \\ &\left[\left(1-2Br_k^2+\sqrt{1-4Br_k^2}\right) e^{-\frac{\left(1+\sqrt{1-4Br_k^2}\right)\left(1-2|\mu_k|r_k\cos(\theta_k+\varphi_k)\right)}{4\sigma_k^2 r_k^2}}\right. \\ &\left.+\left(1-2Br_k^2-\sqrt{1-4Br_k^2}\right) e^{-\frac{\left(1-\sqrt{1-4Br_k^2}\right)\left(1-2|\mu_k|r_k\cos(\theta_k+\varphi_k)\right)}{4\sigma_k^2 r_k^2}}\right] \end{aligned} \tag{6.16}$$

6.3 Performance Analysis

In this section, we apply the PDF of the MMSE frequency-domain channel equalizer taps to the derivation of the BER performance. Following (2.5), the detection variable can be expressed as

$$z_m = \frac{1}{N}\sum_{k=0}^{N-1} C_k H_k x_m + \frac{1}{N}\sum_{\substack{l=0\\ l\neq m}}^{N-1}\left(\sum_{k=0}^{N-1} H_k C_k \mathrm{e}^{-\frac{j2\pi(l-m)k}{N}}\right)x_l + \frac{1}{N}\sum_{l=0}^{N-1}\left(\sum_{k=0}^{N-1} C_k \mathrm{e}^{-\frac{j2\pi(l-m)k}{N}}\right)n_l. \tag{6.17}$$

Conditional on the channel impulse response $\mathbf{h}$, the probability of error for the detection of the mth bit is given by

$$\mathrm{P}_m(e|\mathbf{h}) = \Pr(z_m > 0 | x_m = -1, \mathbf{h}) \tag{6.18}$$

Given $x_m = -1$, we obtain from eqn. (6.17) that

$$\begin{aligned}
L &= z_m | x_m = -1 \\
&= -\frac{1}{N}\sum_{k=0}^{N-1} C_k H_k + \frac{1}{N}\sum_{\substack{l=0 \\ l\neq m}}^{N-1}\left(\sum_{k=0}^{N-1} H_k C_k \mathrm{e}^{-\frac{j2\pi(l-m)k}{N}}\right)x_l + \frac{1}{N}\sum_{l=0}^{N-1}\left(\sum_{k=0}^{N-1} C_k \mathrm{e}^{-\frac{j2\pi(l-m)k}{N}}\right)n_l \\
&= -\frac{1}{N}\sum_{k=0}^{N-1} C_k H_k + \frac{1}{N}\sum_{k=0}^{N-1} C_k H_k \mathrm{e}^{\frac{j2\pi mk}{N}} \sum_{\substack{l=0 \\ l\neq m}}^{N-1} \mathrm{e}^{-\frac{j2\pi lk}{N}} x_l + \frac{1}{\sqrt{N}}\sum_{k=0}^{N-1} C_k N_k \mathrm{e}^{\frac{j2\pi mk}{N}} \\
&= \frac{1}{\sqrt{N}}\sum_{k=0}^{N-1} C_k H_k X_k \mathrm{e}^{\frac{j2\pi mk}{N}} + \frac{1}{\sqrt{N}}\sum_{k=0}^{N-1} C_k N_k \mathrm{e}^{\frac{j2\pi mk}{N}} \\
&= \frac{1}{\sqrt{N}}\sum_{k=0}^{N-1} C_k (H_k X_k + N_k)\mathrm{e}^{\frac{j2\pi mk}{N}} \qquad (6.19)
\end{aligned}$$

where X_k is the Fourier coefficients of one transmitted block x_i, $i = 0, 1, \cdots, N-1$, independent of C_k and N_k. The second to last equality in (6.19) is obtained by applying

$$X_k = \frac{1}{\sqrt{N}}\sum_{\substack{n=0 \\ n\neq m}}^{N-1} x_n \mathrm{e}^{-\frac{j2\pi nk}{N}} - \frac{1}{\sqrt{N}}\mathrm{e}^{-\frac{j2\pi mk}{N}}. \qquad (6.20)$$

6.3.1 Mean and Variance of L

Denote $L_k = C_k(H_k X_k + N_k)\mathrm{e}^{\frac{j2\pi mk}{N}}$. Note that since the $\hat{H}_k$, $k = 0, \cdots, N-1$ are independent RVs, the $\{C_k\}$ are also independent of one another. The RVs $\{X_k\}$ and $\{N_k\}$ are also independent for different ks. As the sum of N independent RVs $\{L_k\}$, L can be modeled as a Gaussian RV with mean μ_L and variance σ_L^2. Since the noise sample N_{p_k} in C_k comes from the pilot block which is independent of N_k, C_k is independent of N_k. Therefore, it is straightforward to show that

$$\begin{aligned}
\mu_L &= \frac{1}{\sqrt{N}}\sum_{k=0}^{N-1} \mathbb{E}\left[C_k(H_k X_k + N_k)\right]\mathrm{e}^{\frac{j2\pi mk}{N}} \\
&= \frac{1}{\sqrt{N}}\sum_{k=0}^{N-1} \mathbb{E}\left[C_k\right]\left\{H_k \mathbb{E}\left[X_k\right] + \mathbb{E}\left[N_k\right]\right\}\mathrm{e}^{\frac{j2\pi mk}{N}} \\
&= -\frac{1}{N}\sum_{k=0}^{N-1} H_k \mathbb{E}\left[C_k\right] \qquad (6.21)
\end{aligned}$$

where

$$\mathbb{E}[X_k] = -\frac{1}{\sqrt{N}} \mathrm{e}^{-\frac{j2\pi mk}{N}} \tag{6.22}$$

is utilized in the last equality.

The variance of L can be obtained as

$$\sigma_L^2 = \mathbb{E}\left[|L|^2\right] - |\mu_L|^2 \tag{6.23}$$

where

$$\begin{aligned}
\mathbb{E}\left[|L|^2\right] &= \frac{1}{N} \sum_{p=0}^{N-1} \sum_{q=0}^{N-1} \mathbb{E}\left[[C_p(H_p X_p + N_p)][C_q^*(H_q^* X_q^* + N_q^*)]\right] \mathrm{e}^{\frac{j2\pi m(p-q)}{N}} \\
&= \frac{1}{N} \sum_{p=0}^{N-1} \sum_{q=0}^{N-1} \mathbb{E}\left[C_p C_q^*\right] \mathbb{E}\left[(H_p X_p + N_p)(H_q^* X_q^* + N_q^*)\right] \mathrm{e}^{\frac{j2\pi m(p-q)}{N}} \\
&= \frac{1}{N} \sum_{p=0}^{N-1} \sum_{q=0}^{N-1} \mathbb{E}\left[C_p C_q^*\right] \left[H_p H_q^* \mathbb{E}\left[X_p X_q^*\right] + \mathbb{E}\left[N_p N_q^*\right]\right] \mathrm{e}^{\frac{j2\pi m(p-q)}{N}}.
\end{aligned}$$

Since

$$\mathbb{E}\left[X_p X_q^*\right] = \begin{cases} 1 & p = q \\ 0 & p \neq q \end{cases}$$

and

$$\mathbb{E}\left[N_p N_q^*\right] = \begin{cases} \sigma_n^2 & p = q \\ 0 & p \neq q \end{cases}$$

we have

$$\mathbb{E}\left[C_p C_q^*\right] \left[H_p H_q^* \mathbb{E}\left[X_p X_q^*\right] + \mathbb{E}(N_p N_q^*)\right] = \begin{cases} \mathbb{E}\left[|C_p|^2\right] \left[|H_p|^2 + \sigma_n^2\right] & p = q \\ 0 & p \neq q \end{cases}$$

and

$$\mathbb{E}\left[|L|^2\right] = \frac{1}{N} \sum_{p=0}^{N-1} \mathbb{E}\left[|C_p|^2\right] \left[|H_p|^2 + \sigma_n^2\right] \tag{6.24}$$

Applying (6.21) and (6.24) to (6.23), the variance of L can be obtained.

6.3.2 Error Probabilities

Having obtained the mean and variance of L, the conditional error probability on $\mathbf{h}$ for the detection of the mth bit within a block can be calculated from (6.18) as

$$\mathrm{P}_m(e|\mathbf{h}) = \mathbf{Q}\left(-\frac{\mu_L}{\sigma_L}\right). \tag{6.25}$$

To calculate (6.25), we need to calculate the values of $\mathbb{E}[C_k]$ and $\mathbb{E}\left[|C_k|^2\right]$. Applying the PDF of C_k obtained in Section 6.2, we show in Appendix E the detailed derivation of $\mathbb{E}[C_k]$ as an example. The calculation of $\mathbb{E}\left[|C_k|^2\right]$ follows the same procedure as in Appendix E. In summary,

$$\mathbb{E}[C_k] = \frac{1}{\sqrt{2}\sigma_k}\mathrm{e}^{-j\phi_k}\mathrm{e}^{-\frac{|\mu_k|^2}{2\sigma_k^2}}\Psi_k(\frac{1}{2},1,1) \tag{6.26}$$

and

$$\mathbb{E}\left[|C_k|^2\right] = \frac{1}{2\sigma_k^2}\mathrm{e}^{-\frac{|\mu_k|^2}{2\sigma_k^2}}\Psi_k(1,2,0) \tag{6.27}$$

where

$$\Psi_k(\varsigma,\tau,\upsilon) = \int_0^\infty \frac{u^\varsigma}{\left(u+\frac{|P_k|^2}{\sigma_b^2}\right)^\tau}\mathrm{e}^{-u}\mathrm{I}_\upsilon(\eta_k\sqrt{u})du \tag{6.28}$$

with $\eta_k = \frac{\sqrt{2}|\mu_k|}{\sigma_k}$ and $\mathrm{I}_\upsilon(\cdot)$ is the υth order modified Bessel function of the first kind.

The conditional error probability (6.25) for the detection of a certain bit x_m within a block can therefore be evaluated with (6.21), (6.23), (6.24), (6.26) and (6.27). The bit error rate of one block conditional on channel gains is then calculated by averaging $\mathrm{P}_m(e|\mathbf{h})$ over the block, and the unconditional probability of error for SC-FDE is obtained by averaging the conditional error probability over 100 UWB channel realizations for a particular channel model.

6.4 Numerical Examples and Discussions

In this section, the error probabilities of SC-FDE system with frequency-domain LS channel estimation error over various UWB channel models are evaluated numerically and compared with the simulation results. The investigated SC-FDE system follows that in Chapter

2, where a data block length $N = 256$ is used, with CP length of 64 and the effective data rate of 400 Mbps.

The semi-analytical results of BER performance of SC-FDE over UWB channels with frequency-domain LS channel estimations are shown in Figs. 6.1-6.4, where one block of an optimal pilot sequence is utilized as in Chapter 3. That is, the pilot sequence has a flat spectrum with its FFT coefficients being constant ones, $|P_k| = 1$ for $k = 0, 1, \cdots, N-1$. Our results show that, compared to the simulation results, Gaussian approximation yields fairly close BER performance to that of the SC-FDE system with frequency-domain MMSE equalization under imperfect channel estimation, thus validating its use. Furthermore, a performance degradation of around 3 dB can be observed compared to the performance of SC-FDE with perfect channel state information.

6.5 Summary

The impact of channel estimation error on the performance of SC-FDE system over UWB channels has been investigated in this chapter. A general analysis method for the BER performance of SC-FDE with channel estimation error has been presented. The BER expression for the SC-FDE system conditioned on the UWB channel has been derived and evaluated numerically. Our results have been validated by utilizing of the Gaussian approximation method in the performance evaluation for the single carrier block transmission with frequency-domain MMSE equalizations and LS channel estimation error over UWB channels.

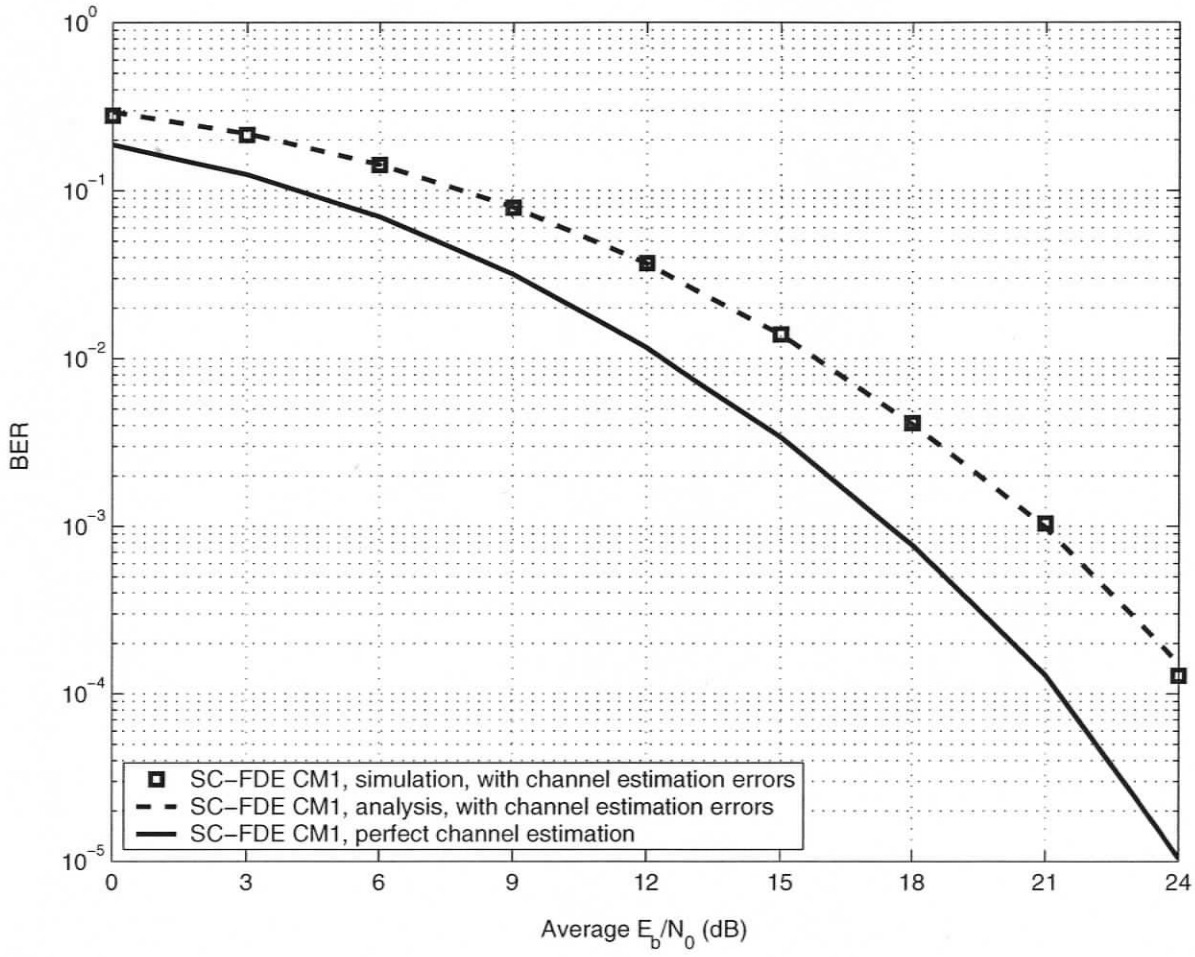

Figure 6.1. *Average BER performance of SC-FDE with channel estimation error over the UWB channel CM1.*

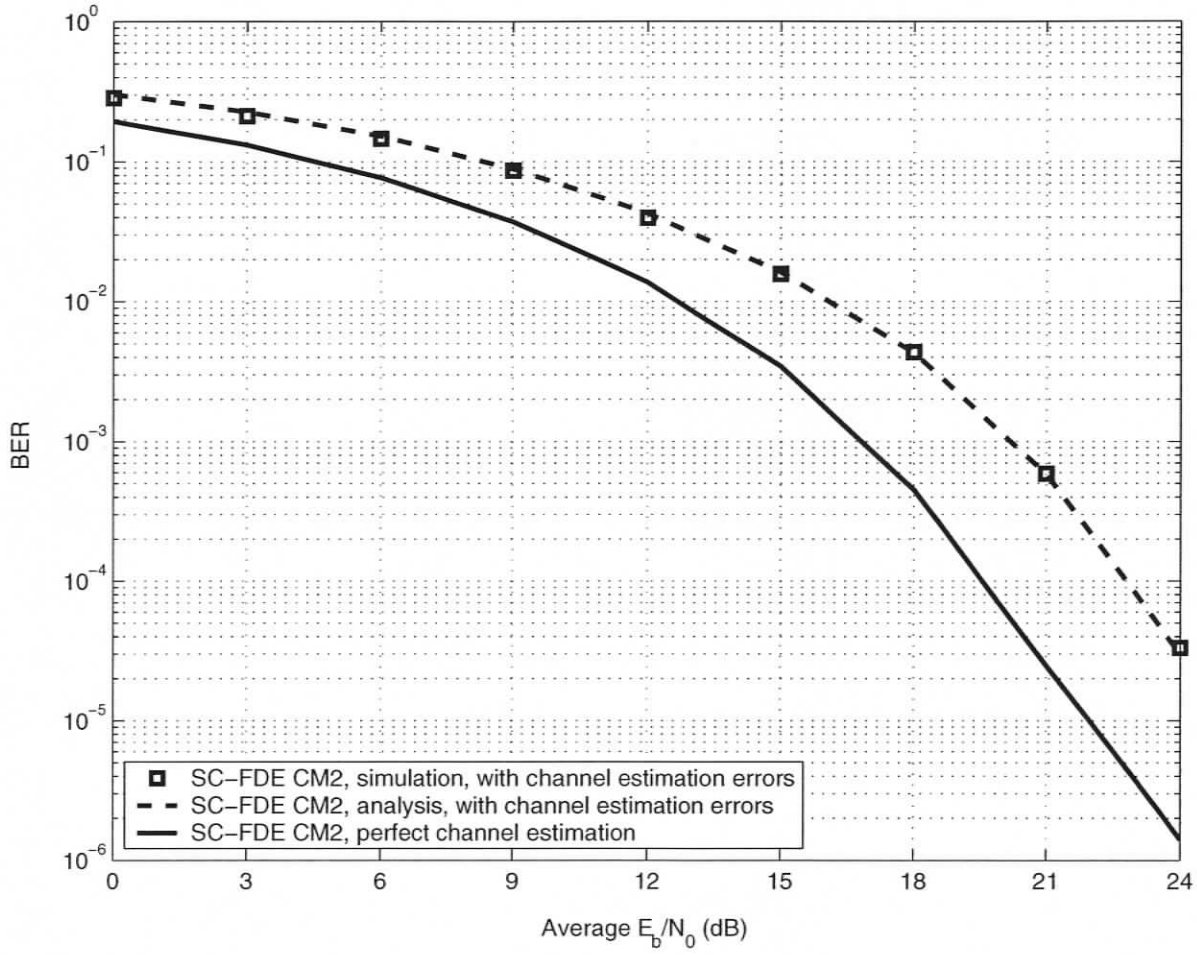

Figure 6.2. *Average BER performance of SC-FDE with channel estimation error over the UWB channel CM2.*

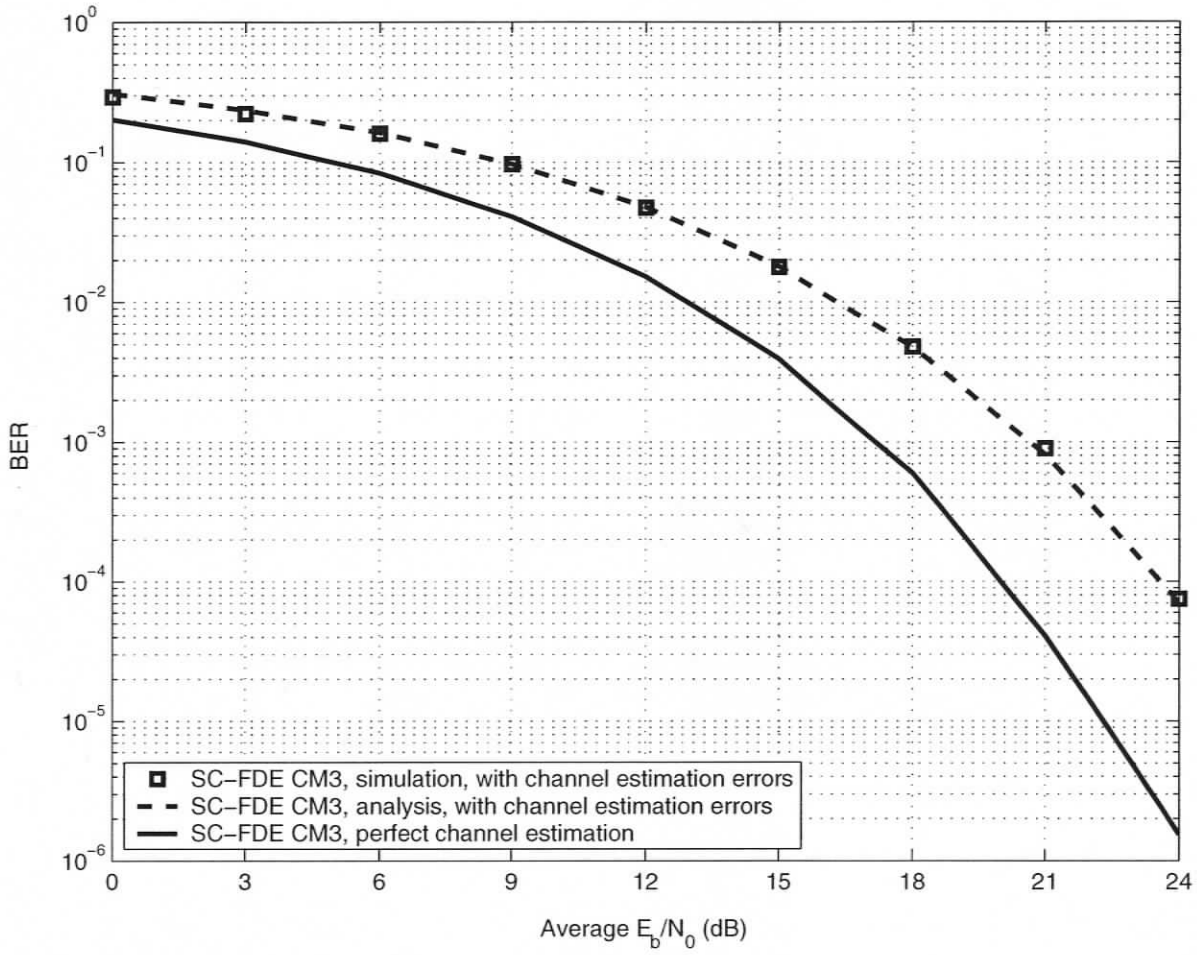

Figure 6.3. *Average BER performance of SC-FDE with channel estimation error over the UWB channel CM3.*

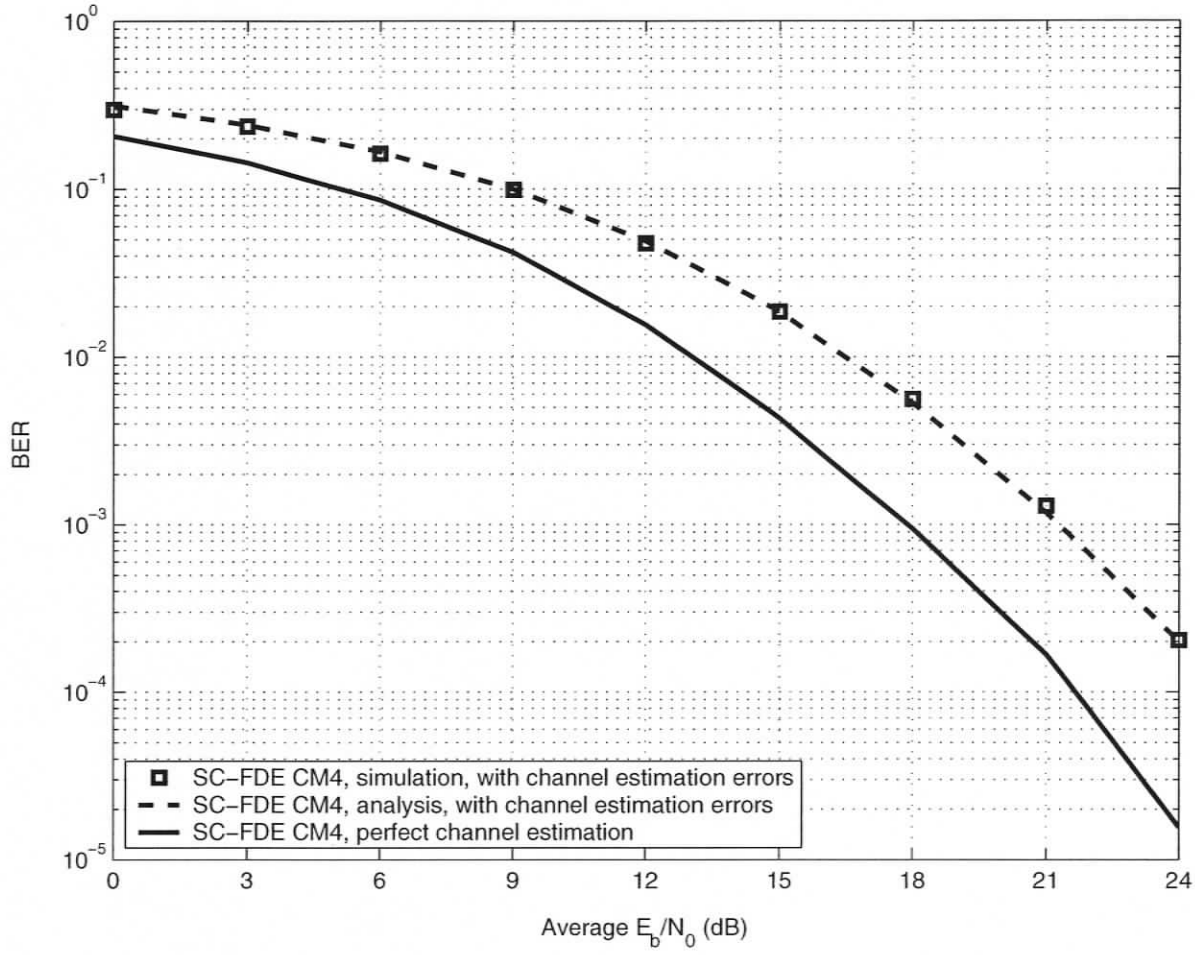

Figure 6.4. *Average BER performance of SC-FDE with channel estimation error over the UWB channel CM4.*

Chapter 7

Effects of Carrier Frequency Offset and Sampling Time Offset at the Performance of SC-FDE UWB

7.1 Background

The performance of SC-FDE system was presented in Chapter 2 and compared to OFDM, based on the assumption of perfect carrier frequency alignment between the transmitter and receiver and optimal sampling time instant can be obtained. However, carrier frequency offset and sampling time offset are usually present in practical systems, resulting in performance degradation in both SC-FDE and OFDM.

The effects of CFO in an OFDM system were extensively investigated in the literature [15, 49–53] and compared with that of single carrier systems [15, 49, 51–53]. Performance studies in [15] and [49] consider the signal-to-noise (SNR) degradation in an AWGN channel only, where the presence of CFO introduces ICI for OFDM and ISI for a single carrier system. In [50], a general analytical method was derived for the BER performance of OFDM systems only in the presence of CFO over AWGN channels. The analysis method was also applied to SC-FDE in [51]. In [52], approximated BER degradations of OFDM and single carrier systems due to CFO over flat Rayleigh fading channels were presented. The BER performance of OFDM over flat fading channels in the presence of CFO

was analyzed in [53], while SC-FDE was studied only by simulation. None of these papers included frequency domain equalization in their analyses. In this paper, we investigate the CFO effect on the performance of SC-FDE with MMSE equalization in terms of SINR and compare with OFDM for frequency selective UWB channels. The BER performance of both systems are also investigated and presented.

STO is another important factor that may degrade system performance, especially in high speed UWB communications where high sampling rates over one narrow pulse make timing requirements fairly stringent. The impact of distorted sampling rate on the performance of multi-carrier code division multiple access (MC-CDMA) was studied in [54], while the impact of a constant STO on OFDM systems was investigated in [55]. However, there were no analytical studies on SC-FDE systems with timing offset. In this paper, we investigate the impact of a constant STO on the performance of the SC-FDE system over UWB channels. Two forms of STO are considered, i.e., the effect of a shifted sampling timing point other than the optimal sampling timing and the effect of a distorted sampling rate other than the symbol rate. In a more general scenario, timing offset is usually modeled as a random variable rather than a constant value, referred to as timing jitter. The effect of random timing jitter on the performance of OFDM-UWB was analyzed in [56], where timing jitter was shown to introduce ICI and become a major degradation factor on the performance of OFDM. In this paper, modeling the sampling timing offset as a uniformly distributed random variable, we simulate the performance of SC-FDE over UWB channels in the presence of timing jitter and compare with OFDM. Other distributions such as Gaussian may be more appropriate to model the random timing jitter.

This chapter is organized as follows. Section 7.2 presents the SC-FDE system model with CFO and STO. In Section 7.3, we derive the SINR of the SC-FDE system over UWB channels in the presence of CFO, compare to that of OFDM. The BER expression for SC-FDE is also presented. Section 7.4 investigates the impact of sampling timing offset on the performance of SC-FDE over UWB channels. Simulation results and discussions are presented in Section 7.5. Section 7.6 concludes this chapter.

7.2 System Model

Fig 7.1 illustrates the system model of an SC-FDE UWB system in the presence of a carrier frequency offset. As in Chapter 2, the SC-FDE system transmits a block of data $\mathbf{x} = [x_{(i-1)N}, \cdots, x_{(i-1)N+N-1}]^T$, where CP is inserted at the beginning of each block.

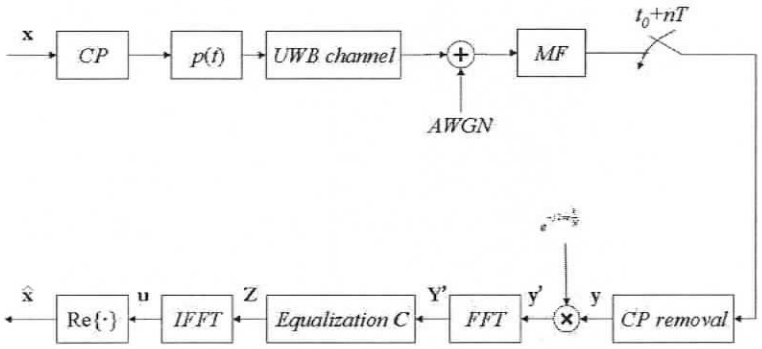

Figure 7.1. *SC-FDE system in the presence of frequency offset*

At the receiver, the presence of a constant STO shifts the sampling point to $\tau\Delta t + n(T_s + \delta\Delta t)$ where $n = 1, 2, \cdots$, $\tau = 0, 1, \cdots, M-1$, and $\frac{1}{\Delta t} = \frac{M}{T_s}$ is the oversampling rate of one pulse, with M being the total number of samples within one symbol duration T_s. Moreover, $\delta = k$, where k is an integer and $0 \leq |k| \leq M-1$ indicates a distorted sampling rate other than the symbol rate. In a more general case where STO is not a constant over each symbol, we model τ_n as a uniformly distributed random variable and refer to $\tau_n \Delta t$ as the timing jitter, where $\tau_n = 0, 1, \cdots, M-1$.

After sampling at the matched filter output, the serial received data is converted to parallel blocks. CP within each block is then removed. The mismatch between transmitter and receiver oscillator causes the CFO. Denoting the normalized CFO by ε, the kth received symbol within a block is distorted by a factor of $e^{-j2\pi\frac{k\varepsilon}{N}}$. The distorted received signal is then converted to the frequency domain using DFT. Frequency domain MMSE equalization is performed to suppress ISI, with equalizer taps given by $C_k = \frac{H_k^*}{|H_k|^2 + N_0/(2E_b)}$ as in Chapter 2. A block of sequence $\mathbf{z}$ is then obtained after frequency domain equalization and an IDFT. When BPSK modulation is used, the decision variable is simply $\hat{\mathbf{x}} = \text{sgn}(\text{Re}\{\mathbf{z}\})$.

7.3 SC-FDE UWB with Frequency Offset

In this section, we present the performance of SC-FDE in terms of SINR in the presence of CFO over UWB channels. The SINR of an OFDM system with CFO is first presented for comparison purpose.

7.3.1 OFDM

It is known that when a block of BPSK modulated signals $\mathbf{x} = [x_0, x_1, \cdots, x_{N-1}]^T$ are transmitted, the received signal after CP removal can be expressed as [15]

$$\mathbf{Y} = \tilde{\mathbf{H}}\mathbf{F}^H\mathbf{x} + \mathbf{n} = \mathbf{F}^H \wedge \mathbf{x} + \mathbf{n}. \tag{7.1}$$

In the presence of frequency offset, the received signal on the kth subcarrier is distorted by $e^{-j\frac{2\pi}{N}k\varepsilon}$, and the received signal $\mathbf{Y}'$ becomes

$$\mathbf{Y}' = \boldsymbol{\varepsilon}\mathbf{Y} = \boldsymbol{\varepsilon}\mathbf{F}^H \wedge \mathbf{x} + \boldsymbol{\varepsilon}\mathbf{n} \tag{7.2}$$

where $\boldsymbol{\varepsilon}$ is a diagonal matrix with $e^{-j\frac{2\pi}{N}k\varepsilon}$ as its kth diagonal element. The received signal after FFT can then be expressed as

$$\mathbf{Z} = \mathbf{F}\mathbf{Y}' = \mathbf{F}\boldsymbol{\varepsilon}\mathbf{F}^H \wedge \mathbf{x} + \mathbf{F}\boldsymbol{\varepsilon}\mathbf{n}. \tag{7.3}$$

One-tap frequency domain equalization is then performed, where the signal after equalization can be obtained as

$$\mathbf{u} = \mathbf{G}\mathbf{Z} = \mathbf{G}\mathbf{F}\boldsymbol{\varepsilon}\mathbf{F}^H \wedge \mathbf{x} + \mathbf{G}\mathbf{F}\boldsymbol{\varepsilon}\mathbf{n} \tag{7.4}$$

where $\mathbf{G}$ is a diagonal matrix with its kth diagonal element being the equalizer taps G_k. Assuming no frequency offset presents, for zero-forcing equalization, we have $G_k = \frac{1}{H_k}$; for MMSE equalization, we have $G_k = \frac{H_k^*}{|H_k|^2 + \frac{N_0}{2E_b}}$.

Signal detection is then performed by taking the real part of $\mathbf{u}$, where the decision variable can be written as $\hat{\mathbf{x}} = \mathrm{Re}\{\mathbf{u}\}$. Following (E.16), the mth decision variable of the

received bit can be written as

$$\begin{aligned}
\mathrm{Re}\{u_m\} &= \frac{1}{N}\mathrm{Re}\left\{\sum_{l=0}^{N-1}\sum_{k=0}^{N-1} H_l G_m e^{-j\frac{2\pi}{N}k(\varepsilon+m-l)}\right\} x_l + \frac{1}{\sqrt{N}}\mathrm{Re}\left\{\sum_{l=0}^{N-1} G_m e^{-j\frac{2\pi}{N}l(\varepsilon+m)} n_l\right\} \\
&= \frac{1}{N}\mathrm{Re}\left\{\sum_{k=0}^{N-1} G_m H_m e^{-j\frac{2\pi}{N}k\varepsilon}\right\} x_m + \frac{1}{N}\mathrm{Re}\left\{\sum_{\substack{l=0\\ l\neq m}}^{N-1}\sum_{k=0}^{N-1} G_m H_l e^{-j\frac{2\pi}{N}k(\varepsilon+m-l)}\right\} x_l + \tilde{n}_m \\
&= G_m H_m \frac{\cos\left(\pi\varepsilon\left(1-\frac{1}{N}\right)\right)\sin(\pi\varepsilon)}{N\sin(\frac{\pi}{N}\varepsilon)} x_m \\
&\quad + \frac{1}{N}\mathrm{Re}\left\{\sum_{\substack{l=0\\ l\neq m}}^{N-1} G_m H_l e^{-j\pi(\varepsilon+m-l)(1-\frac{1}{N})} \frac{\sin(\pi(\varepsilon+m-l))}{\sin\left(\frac{\pi}{N}(\varepsilon+m-l)\right)}\right\} x_l + \tilde{n}_m \\
&= S + I_m + \tilde{n}_m
\end{aligned} \tag{7.5}$$

where the first additional term S contains the desired signal, the second additional term I_m accounts for the resulting ICI due to frequency offset and $\tilde{n}_m = \frac{1}{\sqrt{N}}\mathrm{Re}\left\{\sum_{l=0}^{N-1} G_m e^{-j\frac{2\pi}{N}l(\varepsilon+m)} n_l\right\}$ is the equivalent noise with variance

$$\mathbb{E}\left[\tilde{n}_m^2\right] = \frac{N_0|G_m|^2}{2}. \tag{7.6}$$

Denote E_b as the energy per transmitted bit, the received signal power can be calculated as

$$\mathbb{E}\left[S^2\right] = \frac{E_b|G_m H_m|^2}{N^2}\left|\frac{\sin\pi\varepsilon}{\sin\frac{\pi}{N}\varepsilon}\right|^2\left|\cos\left(\pi\varepsilon\left(1-\frac{1}{N}\right)\right)\right|^2. \tag{7.7}$$

Similarly, the power of ICI can be written as

$$\mathbb{E}\left[I_m^2\right] = \frac{E_b}{2N^2}\sum_{\substack{l=0\\ l\neq m}}^{N-1}|H_l|^2|G_m|^2\left|\frac{\sin\pi(\varepsilon+m-l)}{\sin\frac{\pi}{N}(\varepsilon+m-l)}\right|^2. \tag{7.8}$$

SINR of the received signal can therefore be written as

$$\mathrm{SINR}_{OFDM} = \frac{\mathbb{E}\left[S^2\right]}{\mathbb{E}\left[I_m^2\right]+\mathbb{E}\left[\tilde{n}_m^2\right]} = \frac{\frac{|H_m|^2}{N^2}\left|\frac{\sin\pi\varepsilon}{\sin\frac{\pi}{N}\varepsilon}\right|^2\left|\cos\left(\pi\varepsilon\left(1-\frac{1}{N}\right)\right)\right|^2}{\sum_{\substack{l=0\\ l\neq m}}^{N-1}\frac{|H_l|^2}{2N^2}\left|\frac{\sin\pi(\varepsilon+m-l)}{\sin\frac{\pi}{N}(\varepsilon+m-l)}\right|^2 + \frac{N_0}{2E_b}}. \tag{7.9}$$

Following the derivation above, it is straightforward to show that the SINR of OFDM with frequency domain MMSE equalization in the presence of carrier frequency offset has the same expression as that using zero forcing equalization.

7.3.2 SC-FDE

This subsection calculates the SINR of single carrier transmission with frequency domain MMSE equalization over UWB channels, in the presence of frequency offset. The received signal after matched filtering and CP removal can be expressed as in Chapter 2 by

$$\mathbf{y} = \tilde{\mathbf{H}}\mathbf{x} + \mathbf{n}. \tag{7.10}$$

Signal distorted by the frequency offset can be written as

$$\mathbf{y}' = \boldsymbol{\varepsilon}\mathbf{F}^H \wedge \mathbf{F}\mathbf{x} + \boldsymbol{\varepsilon}\mathbf{n}. \tag{7.11}$$

After performing FFT and frequency domain equalization, the received signal becomes

$$\begin{aligned} \mathbf{Z} &= \mathbf{C}\mathbf{F}\mathbf{y}' \\ &= \mathbf{C}\mathbf{F}\boldsymbol{\varepsilon}\mathbf{F}^H \wedge \mathbf{F}\mathbf{x} + \mathbf{C}\mathbf{F}\boldsymbol{\varepsilon}\mathbf{n} \end{aligned} \tag{7.12}$$

where matrix $\mathbf{C}$ is a diagonal equalization matrix as in Chapter 2. Signal detection is then performed in the time domain as

$$\mathbf{z} = \mathbf{F}^H\mathbf{C}\mathbf{F}\boldsymbol{\varepsilon}\mathbf{F}^H \wedge \mathbf{F}\mathbf{x} + \mathbf{F}^H\mathbf{C}\mathbf{F}\boldsymbol{\varepsilon}\mathbf{n}. \tag{7.13}$$

Taking the real part of $\mathbf{z}$, the decision variable becomes

$$\hat{\mathbf{x}} = \mathrm{Re}\{\mathbf{z}\}. \tag{7.14}$$

The mth detected bit can therefore be written as

$$\begin{aligned} \hat{x}_m &= \frac{1}{N^2}\mathrm{Re}\left\{\sum_{p=0}^{N-1}\sum_{n=0}^{N-1}\sum_{k=0}^{N-1}\sum_{l=0}^{N-1} H_k C_l e^{-j\frac{2\pi}{N}l(n-m)} e^{-j\frac{2\pi}{N}n\varepsilon} e^{j\frac{2\pi}{N}(n-p)k}\right\} x_p \\ &\quad + \frac{1}{N}\mathrm{Re}\left\{\sum_{l=0}^{N-1}\sum_{k=0}^{N-1} C_k e^{-j\frac{2\pi}{N}(l-m)k} e^{-j\frac{2\pi}{N}l\varepsilon} n_l\right\} \\ &= \frac{1}{N^2}\mathrm{Re}\left\{\sum_{k=0}^{N-1}\sum_{l=0}^{N-1} H_k C_l e^{-j\frac{2\pi}{N}m(k-l)} e^{-j\pi(1-\frac{1}{N})(\varepsilon-k+l)} \frac{\sin\pi(\varepsilon-k+l)}{\sin\frac{\pi}{N}(\varepsilon-k+1)}\right\} x_m \\ &\quad + \frac{1}{N^2}\mathrm{Re}\left\{\sum_{\substack{p=0 \\ p\neq m}}^{N-1}\sum_{k=0}^{N-1}\sum_{l=0}^{N-1} H_k C_l e^{j\frac{2\pi}{N}lm} e^{-j\frac{2\pi}{N}pk} e^{-j\pi(1-\frac{1}{N})(\varepsilon-k+l)} \frac{\sin\pi(\varepsilon-k+l)}{\sin\frac{\pi}{N}(\varepsilon-k+l)}\right\} x_p + \tilde{n}_m \\ &= S + I_m + \tilde{n}_m \end{aligned} \tag{7.15}$$

where

$$S = \frac{1}{N^2}\mathrm{Re}\left\{\sum_{k=0}^{N-1}\sum_{l=0}^{N-1} H_k C_l e^{-j\frac{2\pi}{N}m(k-l)} e^{-j\pi(1-\frac{1}{N})(\varepsilon-k+l)} \frac{\sin\pi(\varepsilon-k+l)}{\sin\frac{\pi}{N}(\varepsilon-k+1)}\right\} x_m \tag{7.16}$$

is the desired signal with variance

$$\mathbb{E}\left[S^2\right] = \frac{E_b}{2N^4}\left|\sum_{k=0}^{N-1}\sum_{l=0}^{N-1} H_k C_l e^{-j\frac{2\pi}{N}m(k-l)} e^{-j\pi(1-\frac{1}{N})(\varepsilon-k+l)} \frac{\sin\pi(\varepsilon-k+l)}{\sin\frac{\pi}{N}(\varepsilon-k+1)}\right|^2. \tag{7.17}$$

Moreover, $\tilde{n}_m = \frac{1}{N}\mathrm{Re}\left\{\sum_{l=0}^{N-1}\sum_{k=0}^{N-1} C_k e^{-j\frac{2\pi}{N}(l-m)k} e^{-j\frac{2\pi}{N}l\varepsilon} n_l\right\}$ is the equivalent noise with variance

$$\sigma^2_{\tilde{n}_m} = \mathbb{E}\left[\tilde{n}_m^2\right] = \frac{N_0}{2N^2}\sum_{l=0}^{N-1}\left|\sum_{k=0}^{N-1} C_k e^{-j\frac{2\pi}{N}(l-m)k}\right|^2. \tag{7.18}$$

The second additional term in (7.15) is the enhanced inter-symbol interference in the presence of the carrier frequency offset. Since the desired term S is independent of the interference term I_m, the interference power can be calculated as

$$\mathbb{E}\left[I_m^2\right] = \mathbb{E}\left[(S+I_m)^2\right] - \mathbb{E}\left[S^2\right] \tag{7.19}$$

where

$$\begin{aligned}
\mathbb{E}\left[(S+I_m)^2\right] &= \frac{1}{2N^4}\mathbb{E}\left|\sum_{p=0}^{N-1}\sum_{k=0}^{N-1}\sum_{l=0}^{N-1} H_k C_l e^{j\frac{2\pi}{N}lm} e^{-j\frac{2\pi}{N}pk} e^{-j\pi(1-\frac{1}{N})(\varepsilon-k+l)} \frac{\sin\pi(\varepsilon-k+l)}{\sin\frac{\pi}{N}(\varepsilon-k+l)} x_p\right|^2 \\
&= \frac{1}{2N^4}\sum_{k_1=0}^{N-1}\sum_{k_2=0}^{N-1}\sum_{l_1=0}^{N-1}\sum_{l_2=0}^{N-1} H_{k_1} H_{k_2}^* C_{l_1} C_{l_2}^* e^{j\frac{2\pi}{N}l_1 m} e^{-j\frac{2\pi}{N}l_2 m} e^{-j\pi(1-\frac{1}{N})(\varepsilon-k_1+l_1)} \\
&\quad e^{j\pi(1-\frac{1}{N})(\varepsilon-k_2+l_2)} \frac{\sin\pi(\varepsilon-k_1+l_1)}{\sin\frac{\pi}{N}(\varepsilon-k_1+l_1)} \frac{\sin\pi(\varepsilon-k_2+l_2)}{\sin\frac{\pi}{N}(\varepsilon-k_2+l_2)} \\
&\quad \sum_{p_1=0}^{N-1}\sum_{p_2=0}^{N-1} e^{-j\frac{2\pi}{N}p_1 k_1} e^{j\frac{2\pi}{N}p_2 k_2} \mathbb{E}\{x_{p_1} x_{p_2}^*\} \\
&= \frac{E_b}{2N^4}\sum_{k_1=0}^{N-1}\sum_{k_2=0}^{N-1}\sum_{l_1=0}^{N-1}\sum_{l_2=0}^{N-1} H_{k_1} H_{k_2}^* C_{l_1} C_{l_2}^* e^{j\frac{2\pi}{N}l_1 m} e^{-j\frac{2\pi}{N}l_2 m} e^{-j\pi(1-\frac{1}{N})(l_1-k_1)} e^{j\pi(1-\frac{1}{N})(l_2-k_2)} \\
&\quad \frac{\sin\pi(\varepsilon-k_1+l_1)}{\sin\frac{\pi}{N}(\varepsilon-k_1+l_1)} \frac{\sin\pi(\varepsilon-k_2+l_2)}{\sin\frac{\pi}{N}(\varepsilon-k_2+l_2)} \sum_{p=0}^{N-1} e^{-j\frac{2\pi}{N}p(k_1-k_2)} \\
&= \frac{E_b}{2N^3}\sum_{k=0}^{N-1}|H_k|^2\left|\sum_{l=0}^{N-1} C_l e^{j\frac{2\pi}{N}lm} e^{-j\pi(1-\frac{1}{N})l} \frac{\sin\pi(\varepsilon-k+l)}{\sin\frac{\pi}{N}(\varepsilon-k+l)}\right|^2.
\end{aligned} \tag{7.20}$$

Therefore,

$$\mathbb{E}\left[I_m^2\right] = \frac{E_b}{2N^3}\sum_{k=0}^{N-1}|H_k|^2\left|\sum_{l=0}^{N-1}C_l e^{j\frac{2\pi}{N}lm}e^{-j\pi(1-\frac{1}{N})l}\frac{\sin\pi(\varepsilon-k+l)}{\sin\frac{\pi}{N}(\varepsilon-k+l)}\right|^2 - \mathbb{E}\left[S^2\right]. \tag{7.21}$$

The SINR of SC-FDE in the presence of frequency offset can therefore be obtained as

$$\mathrm{SINR}_{SCFDE} = \frac{\mathbb{E}[S^2]}{\mathbb{E}\left[I_m^2\right]+\mathbb{E}\left[\tilde{n}_m^2\right]}. \tag{7.22}$$

Having obtained (7.15), the bit error rate analysis follows as in Chapter 2, where the error probability of the mth bit in the presence of frequency offset conditional on the channel impulse response $\mathbf{h}$ can be written as

$$\mathrm{P}_m(e|\mathbf{h}) = \frac{1}{2} - \frac{2}{\pi}\sum_{\substack{u=1\\ u\,odd}}^{U}\left[\frac{\exp(-u^2\omega^2/2)\sin(u\omega q_0)}{u}\prod_{\substack{p=0\\ p\neq m}}^{N-1}\cos(u\omega q_p)\right] + \varepsilon_0 \tag{7.23}$$

where

$$q_0 = \frac{1}{N^2\sigma_{\tilde{n}_m}^2}\mathrm{Re}\left\{\sum_{k=0}^{N-1}\sum_{l=0}^{N-1}H_k C_l e^{-j\frac{2\pi}{N}m(k-l)}e^{-j\pi(1-\frac{1}{N})(\varepsilon-k+l)}\frac{\sin\pi(\varepsilon-k+l)}{\sin\frac{\pi}{N}(\varepsilon-k+1)}\right\} \tag{7.24}$$

and

$$q_p = \frac{1}{N^2\sigma_{\tilde{n}_m}^2}\mathrm{Re}\left\{\sum_{k=0}^{N-1}\sum_{l=0}^{N-1}H_k C_l e^{j\frac{2\pi}{N}lm}e^{-j\frac{2\pi}{N}pk}e^{-j\pi(1-\frac{1}{N})(\varepsilon-k+l)}\frac{\sin\pi(\varepsilon-k+l)}{\sin\frac{\pi}{N}(\varepsilon-k+l)}\right\}. \tag{7.25}$$

The definitions of ω, U and ε_0 can be found in Chapter 2 and the reference therein. The average BER performance of SC-FDE over UWB channels in the presence of frequency offset is simply an average of (7.23) over the evaluated channel realizations.

7.4 Timing Offset

In this section, we study the impact of STO on the performance of SC-FDE over UWB channels. As illustrated in Section 7.2, instead of sampling at the optimal time instant with symbol rate, the matched filter output is sampled at point $\tau\Delta t + n(T_s + \delta\Delta t)$. Since there is

minimal effect of timing offset on the noise sampling, we discard the Gaussian noise term in the following analysis for simplicity.

We consider the case $\delta = 0$ first, i.e., the output matched filter samples at the desired symbol rate. Denote the BPSK transmitted block of signal as $\mathbf{x} = [x_0, x_1, \cdots, x_{N-1}]^T$. The transmitted block after inserting CP of length L can be expressed as $\bar{\mathbf{x}} = \mathbf{T}_{cp}\mathbf{x}$, where $\mathbf{T}_{cp}$ of dimension $(N+L) \times N$ matrix is a concatenation of the last L rows of an $N \times N$ identity matrix $\mathbf{I}_N$ and $\mathbf{I}_N$ [57]. Pulse shaping and oversampling the transmitted pulse at a rate of $\frac{M}{T_s}$ is equivalent to first padding $(M-1)$ zeros to the end of each transmitted bit and then convolving the serial of the zero-padded bits to the transmitter pulse shaping filter $p(t)$. The transmitted block with oversampled resolution can be expressed as $\bar{\mathbf{x}}_o = \mathbf{O}\mathbf{T}_{cp}\mathbf{x}$, where the oversampling matrix $\mathbf{O} = \mathbf{I}_{N+L} \otimes \boldsymbol{\alpha}$ is an $(N+L)M \times (N+L)$ matrix, and $\boldsymbol{\alpha}$ is an $M \times 1$ column vector with its first element being 1 and 0's elsewhere.

The oversampled transmitted data sequence is then pulse shaped and fed into the UWB channel. Convolving the received signal with the receiver matched filter, the signal before downsampling can be expressed as

$$\bar{\mathbf{y}}_o = \mathbf{H}\bar{\mathbf{x}}_o. \tag{7.26}$$

The $(N+L)M \times (N+L)M$ matrix $\mathbf{H}$ is an upper triangular toeplitz matrix with its first column being the equivalent channel taps $\mathbf{h}$ zero-padded to length $(N+L)M$, where $\mathbf{h} = [h(0), h(1), \cdots]^T$, and $h(n) = h(t)\big|_{t=n\frac{T_s}{M}}$. Suppose the receiver samples the received signal at the sampling point $\tau\Delta t + nT_s$, the sampled received signal can then be expressed as

$$\bar{\mathbf{y}}_\tau = \mathbf{D}_\tau \bar{\mathbf{y}}_o. \tag{7.27}$$

Matrix $\mathbf{D}_\tau$ denotes the $(N+L)M \times (N+L)$ downsampling matrix and $\mathbf{D}_\tau = \mathbf{I}_{N+L} \otimes \boldsymbol{\beta}_\tau$, where $\boldsymbol{\beta}_\tau$ is the length M row vector with its τth element being 1 and 0's elsewhere.

Following (7.26) and (7.27), the τth sampled version of the received signal can be obtained as $\bar{\mathbf{y}}_\tau = \mathbf{D}_\tau\mathbf{H}\mathbf{O}\mathbf{T}_{cp}\mathbf{x}$. The received signal after CP removal can then be written as

$$\mathbf{y}_\tau = \mathbf{R}_{cp}\mathbf{D}_\tau\mathbf{H}\mathbf{O}\mathbf{T}_{cp}\mathbf{x} = \mathbf{R}_{cp}(\mathbf{I}_{N+L} \otimes \boldsymbol{\beta})\mathbf{H}(\mathbf{I}_{N+L} \otimes \boldsymbol{\alpha})\mathbf{T}_{cp}\mathbf{x} \tag{7.28}$$

where $\mathbf{R}_{cp}$ is an $N \times (N+L)$ matrix which is a concatenation of an $N \times L$ zero matrix and an $N \times N$ identity matrix [57].

Left multiplication of $\mathbf{D}_\tau$ to $\mathbf{H}$ is equivalent to downsampling rows of matrix $\mathbf{H}$ starting at its τth row by every M rows. In addition, right multiplication of $\mathbf{O}$ to $\mathbf{H}$ is equivalent to downsampling columns of matrix $\mathbf{H}$ starting from the 0th column by every M columns. The multiplication of $\mathbf{D}_\tau\mathbf{HO}$ can therefore be expressed as $\mathbf{D}_\tau\overline{\mathbf{H}}\mathbf{O}$, where $\overline{\mathbf{H}}$ is the modified toeplitz matrix of the equivalent channel, with its $(\tau+nM, nM)$th element unchanged as that in the original toeplitz matrix $\mathbf{H}$, while the other elements being replaced by 0's. The modified channel toeplitz matrix $\overline{\mathbf{H}}$ can therefore be expressed as $\overline{\mathbf{H}} = \overline{\mathbf{H}}_\tau \otimes \mathbf{J}_\tau$, where $\overline{\mathbf{H}}_\tau$ is the $(N+L) \times (N+L)$ upper triangular toeplitz matrix with its first column $\overline{\mathbf{h}}_\tau = [\overline{h}_{\tau_0}, \overline{h}_{\tau_1}, \cdots, \overline{h}_{\tau_{N+L-1}}]^T$ being the τth downsampled version of $\mathbf{h}$ by every M samples. That is, the first column of $\overline{\mathbf{H}}_\tau$ contains the τth, $(\tau+M)$th, $\cdots$ samples of $\mathbf{h}$. Moreover, $\mathbf{J}_\tau$ is the $M \times M$ matrix with the first column being $\boldsymbol{\beta}_\tau^T$ and zeros elsewhere. The received signal after CP removal can therefore be expressed as

$$\begin{aligned} \mathbf{y}_\tau &= \mathbf{R}_{cp}(\mathbf{I}_{N+L} \otimes \boldsymbol{\beta}_\tau)(\overline{\mathbf{H}}_\tau \otimes \mathbf{J}_\tau)(\mathbf{I}_{N+L} \otimes \boldsymbol{\alpha})\mathbf{T}_{cp}\mathbf{x} \\ &= \mathbf{R}_{cp}\overline{\mathbf{H}}_\tau\mathbf{T}_{cp}\mathbf{x} \end{aligned} \tag{7.29}$$

where the property of the Kronecker's product $(\mathbf{A} \otimes \mathbf{B})(\mathbf{C} \otimes \mathbf{D}) = \mathbf{AC} \otimes \mathbf{BD}$ [35] has been applied. Since the insertion and removal of the CP at the transmitter and receiver can still form the toeplitz matrix $\overline{\mathbf{H}}_\tau$ to a circulant matrix $\tilde{\mathbf{H}}_\tau$, the received signal before FFT can be obtained as $\mathbf{y}_\tau = \tilde{\mathbf{H}}_\tau\mathbf{x} = \mathbf{F}^H \wedge_\tau \mathbf{F}\mathbf{x}$ where $\wedge_\tau$ is a diagonal matrix with its kth diagonal element being $H_{\tau_k} = \sum_{m=0}^{N-1} \overline{h}_{\tau_m} e^{-j\frac{2\pi}{N}\tau_m\tau_k}$. The τth sampled version of the received signal is only affected by the frequency-domain channel attenuation factors resulting from the Fourier transform of $\overline{\mathbf{h}}_\tau$. The BER performance due to timing offset can therefore be obtained in the same way as in [58], except that a different timing sampling point is now utilized to downsample the channel, resulting in a different symbol spaced equivalent channel.

For the case where the matched filter output is sampled at a sampling rate other than the

symbol rate $1/T_s$, i.e., instead of sampling at the timing instant $\tau\Delta t + nT_s$, the matched filter output is sampled at the timing instant $\tau\Delta t + n(T_s + \delta\Delta t)$, where $\tau = \pm 1, \cdots, \pm(M-1)$. We take the case of $\delta > 0$ as an example to illustrate the effect of distorted sampling rate on the performance of SC-FDE over UWB channels. Different from the $\delta = 0$ case, although right multiplication of the upsampling matrix to channel matrix $\mathbf{H}$ is equivalent to downsampling channel matrix $\mathbf{H}$ from the 0th column by every M columns, the left multiplication of downsampling matrix to channel matrix $\mathbf{H}$ is now equivalent to downsampling channel matrix $\mathbf{H}$ from the τth row by every $(M+\delta)$ rows. The resulting matrix is therefore no longer a toeplitz matrix. As a consequence of mismatched symbol sampling rate at the transmitter and the receiver, severe performance degradation will occur since the desired circulant matrix cannot be formed by insertion and removal of CP at the transmitter and receiver, and the subsequent FFT and frequency-domain equalization cannot be carried out properly.

7.5 Simulation Results

The effects of CFO and STO on the performance of SC-FDE with MMSE equalization are presented in this section, compared with that of an OFDM system adopting one tap zero-forcing equalization. The UWB channels used are the CM1-CM4 channel models proposed by the IEEE 802.15.3a Working Group [2]. Also plotted is the average BERs of both systems over 100 UWB channel realizations with a constant sampling timing offset $\tau = 5$ (0.33 ns), a uniformly distributed timing jitter between 0 to $2\Delta t = 0.12$ ns and 0 to $5\Delta t = 0.33$ ns.

For both the investigated SC-FDE and OFDM system, we use the data block of length $N = 256$, a CP length of 64 and a bit duration of 2 ns, indicating a data rate of 400 Mbps. The transmitter pulse shaping filter and the channels follows that in Chapter 2.

Figs. 7.2-7.5 show the average SINR of SC-FDE and OFDM over 100 UWB channels from CM1-CM4 calculated by the formulas derived in Section 7.3. It can be observed

that for each investigated channel model, the degradation of SINR in an OFDM system due to CFO is much higher than that in an SC-FDE system, especially at high SNRs. For example, at SNR= 25 dB in CM1, an SINR degradation of around 3 dB can be observed with an increased CFO from 0.02 to 0.05, and around 4 dB for an increased CFO from 0.05 to 0.1 in an OFDM system due to ICI, while SC-FDE only suffers less than 1 dB SINR degradation, due to an enhanced ISI.

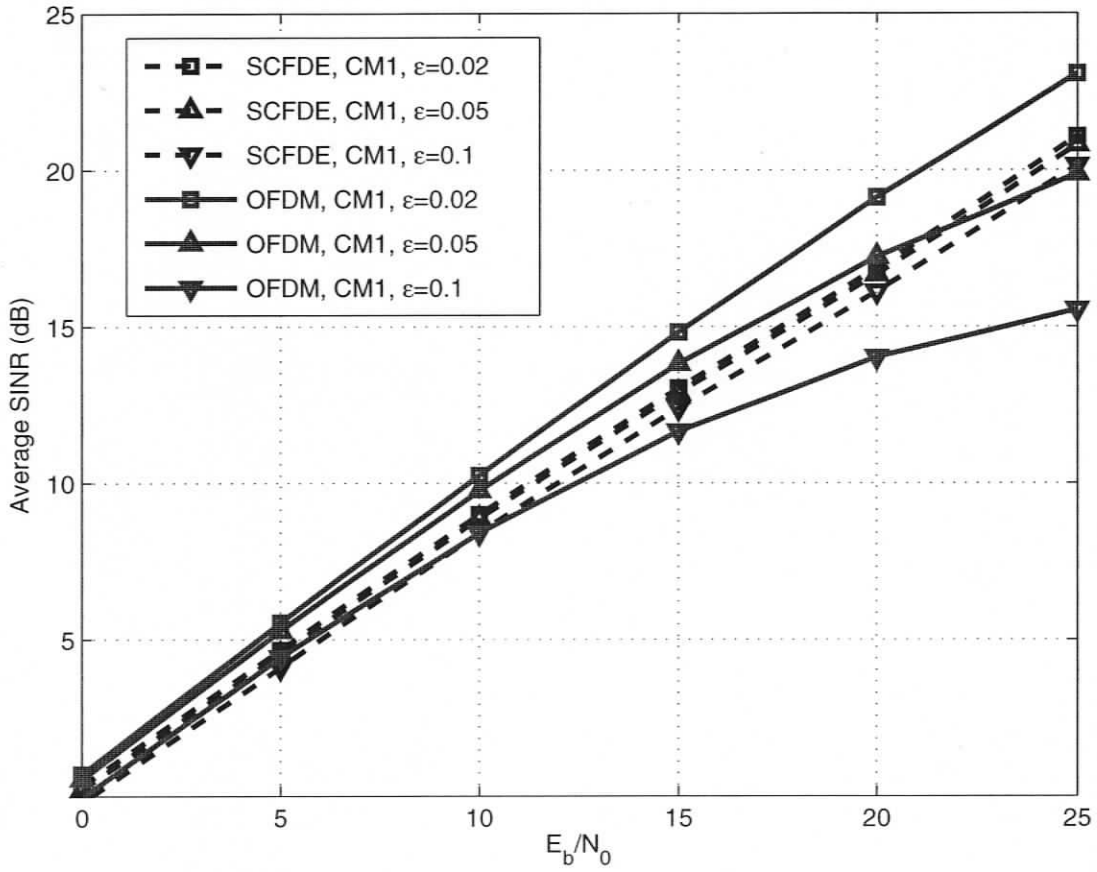

Figure 7.2. *SINR comparison of SC-FDE and OFDM over UWB channel CM1 in the presence of CFO* $\varepsilon = 0.02$, $\varepsilon = 0.05$ *and* $\varepsilon = 0.1$.

Note that the SINR values are averaged results over all the subcarriers and 100 channel realizations. Although OFDM yields a larger SINR value than SC-FDE at $\varepsilon = 0.02$

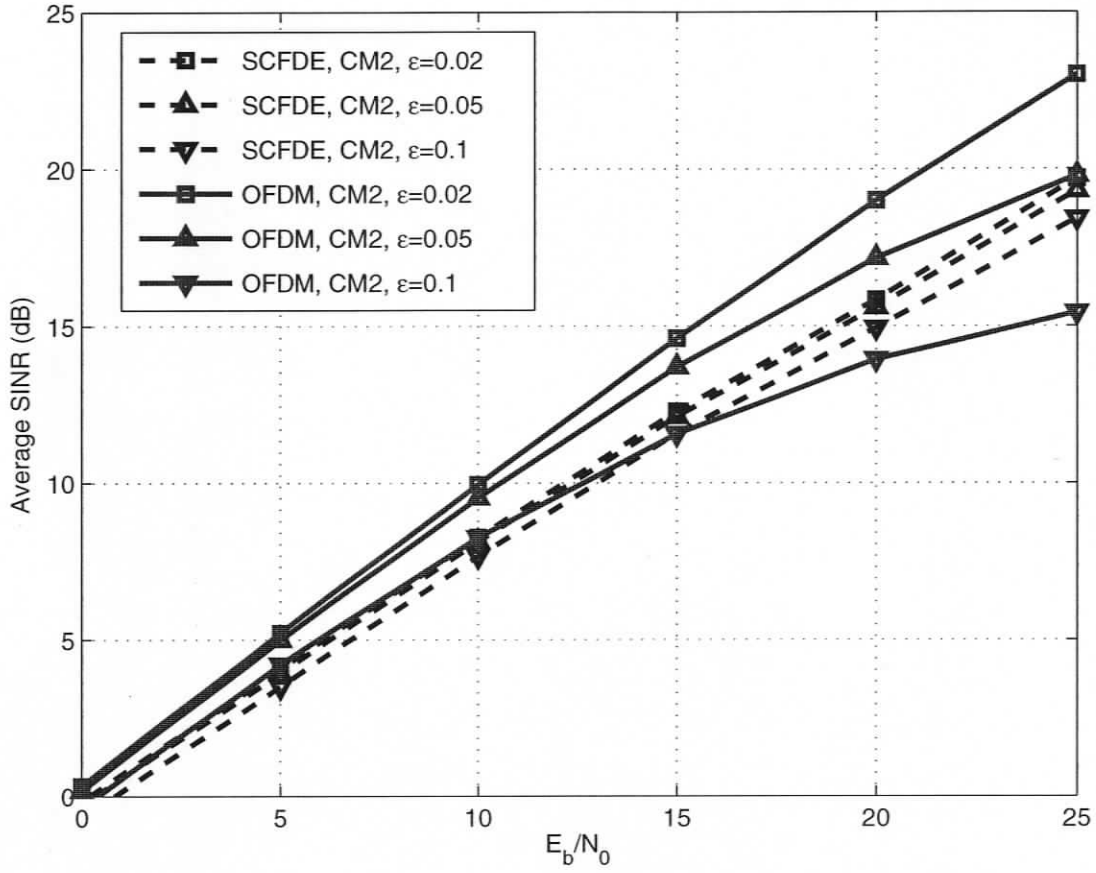

Figure 7.3. *SINR comparison of SC-FDE and OFDM over UWB channel CM2 in the presence of CFO* $\varepsilon = 0.02$, $\varepsilon = 0.05$ *and* $\varepsilon = 0.1$.

and $\varepsilon = 0.05$ in most of the investigated channel models, it does not mean OFDM-UWB has a better BER performance than SC-FDE in the presence of CFO. In fact, due to the enhanced noise power introduced by equalizing certain subcarriers with frequency nulls in OFDM, severe performance degradation will occur for these subcarriers and they dominate the overall performance. The SC-FDE system, however, does not suffer from the loss of frequency diversity. Figs. 7.6-7.9 plot the BER performance of SC-FDE and OFDM over UWB channel models CM1 and CM4, at normalized CFOs of 0.02, 0.05 and 0.1, respectively. Similar to Figs. 7.2-7.5, both systems suffer a performance degradation due to the

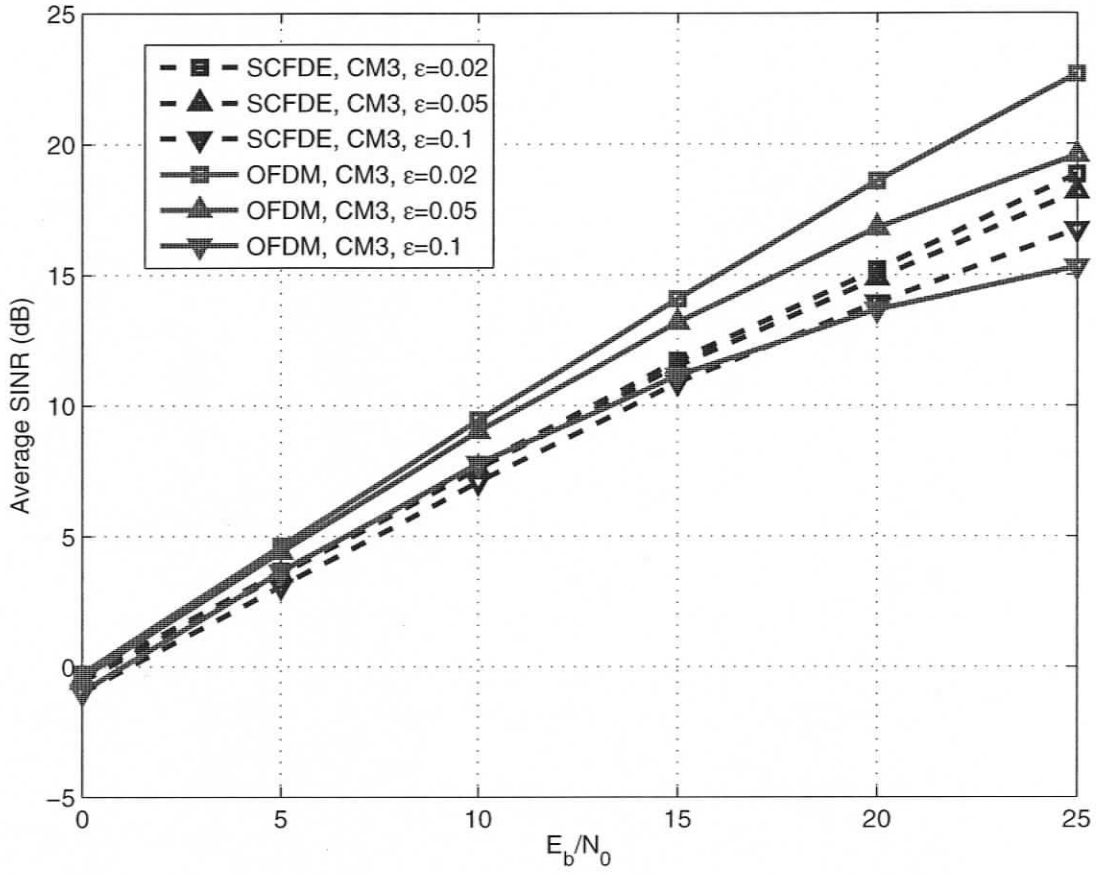

Figure 7.4. *SINR comparison of SC-FDE and OFDM over UWB channel CM3 in the presence of CFO* $\varepsilon = 0.02$, $\varepsilon = 0.05$ *and* $\varepsilon = 0.1$.

increased CFO, with OFDM more sensitive to it, especially when CFO becomes larger or at higher SNRs. For example, with an increased CFO from 0.05 to 0.1, the performance degradation of SC-FDE is around 1 dB, while OFDM suffers more than 3 dB at BER $= 10^{-3}$ in a majority of UWB channel models.

In order to investigate the effect of a constant timing offset within one symbol duration ($\delta = 0$), we present in Figs. 7.10 and 7.11 the BERs of SC-FDE obtained at different sampling timing points $\frac{nT_s}{M}$, where $T_s = 2$ ns, $M = 33$ and $n = 0, 1, \cdots, M-1$. The BERs are evaluated under channel realization 1 for CM4 and channel 50 for CM1 at SNR $= 0$

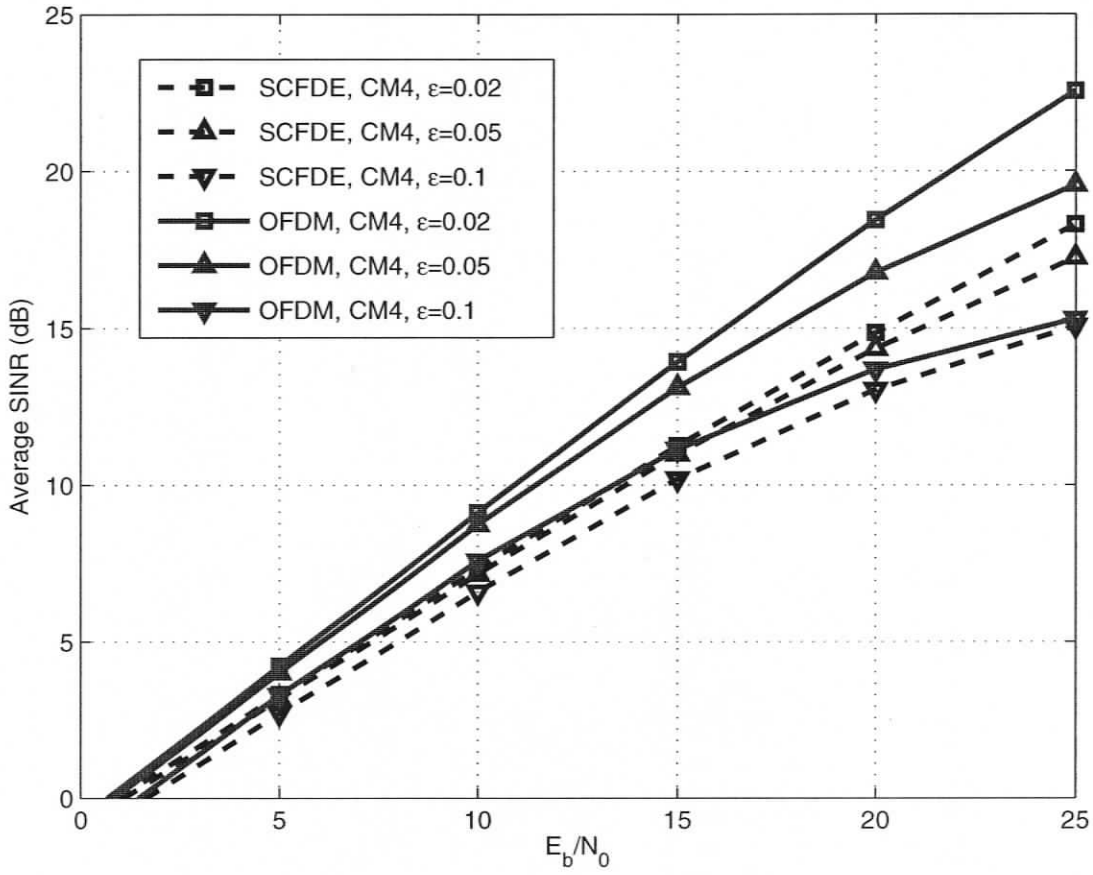

Figure 7.5. *SINR comparison of SC-FDE and OFDM over UWB channel CM4 in the presence of CFO* $\varepsilon = 0.02$, $\varepsilon = 0.05$ *and* $\varepsilon = 0.1$.

dB, 5 dB and 10 dB, respectively. Also plotted in Figs. 7.10 and 7.11 is the normalized channel energy captured by these sampling points. Both figures show a general trend that the more channel energy captured by a sampling position, the less the resulting BER. The performance of SC-FDE is rather channel dependent, and the energy of the sampled equivalent channel at the sampling timing point determines the BER. Furthermore, although not shown here, other channel realizations result in similar performance behavior. Finally, the performance of SC-FDE is more sensitive to different sampling points in CM1 channels than in CM4 channels, because the channel energy captured at a different sampling point

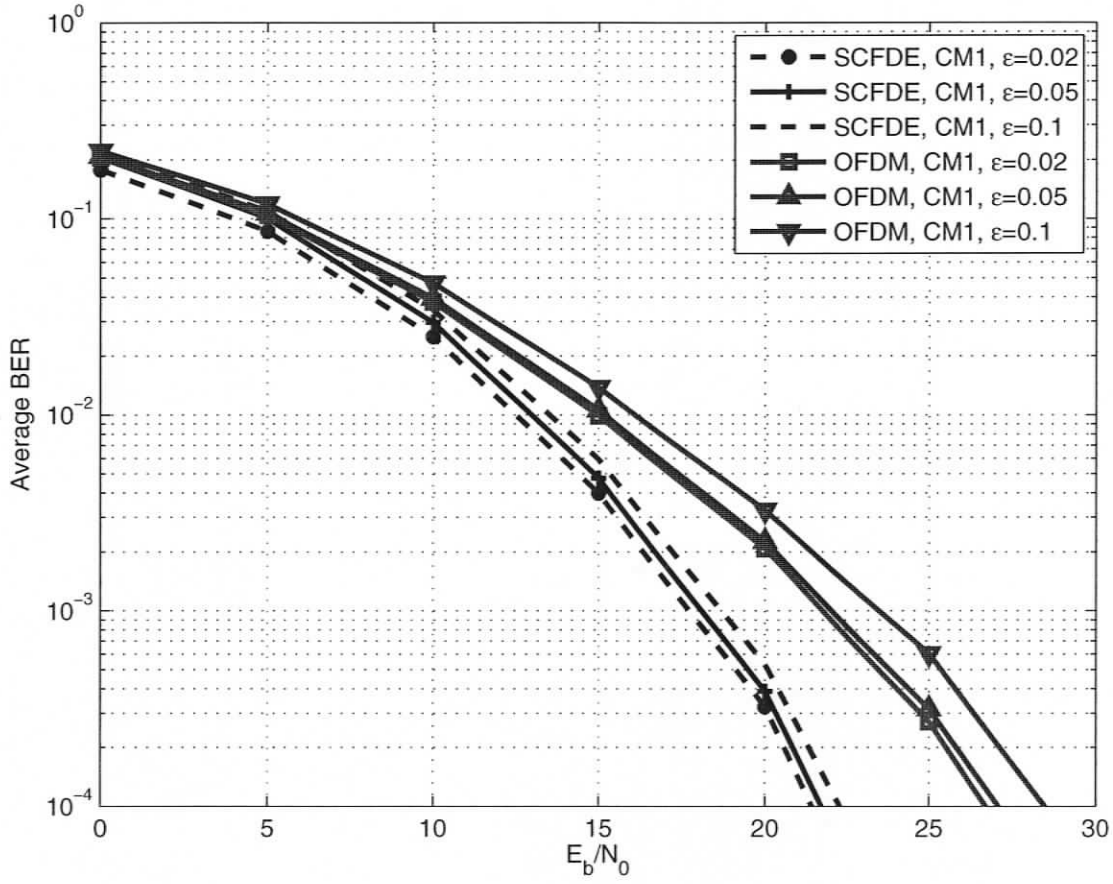

Figure 7.6. *BER of SC-FDE and OFDM over UWB channel CM1 in the presence of CFO* $\varepsilon = 0.02$, $\varepsilon = 0.05$ *and* $\varepsilon = 0.1$.

tends to vary more in less frequency selective channels such as CM1.

In Figs. 7.12-7.13, we present the average BER performance of SC-FDE and OFDM over UWB channel models CM2-CM4 in the presence of a constant STO $\tau = 5$ (i.e., the the actual sampling point shifts from the optimal sampling point by a factor of $\frac{5T_s}{M} = 0.33$ ns), and a timing jitter uniformly distributed from 0 to 0.12 ns and 0 to 0.33 ns, respectively. It can be observed that in the presence of a constant STO, both systems suffer from a severe performance degradation, with OFDM slightly more sensitive to it. For example, Fig. 7.12 shows that OFDM suffers around 6 dB performance degradation at BER$= 4 \times 10^{-3}$ in

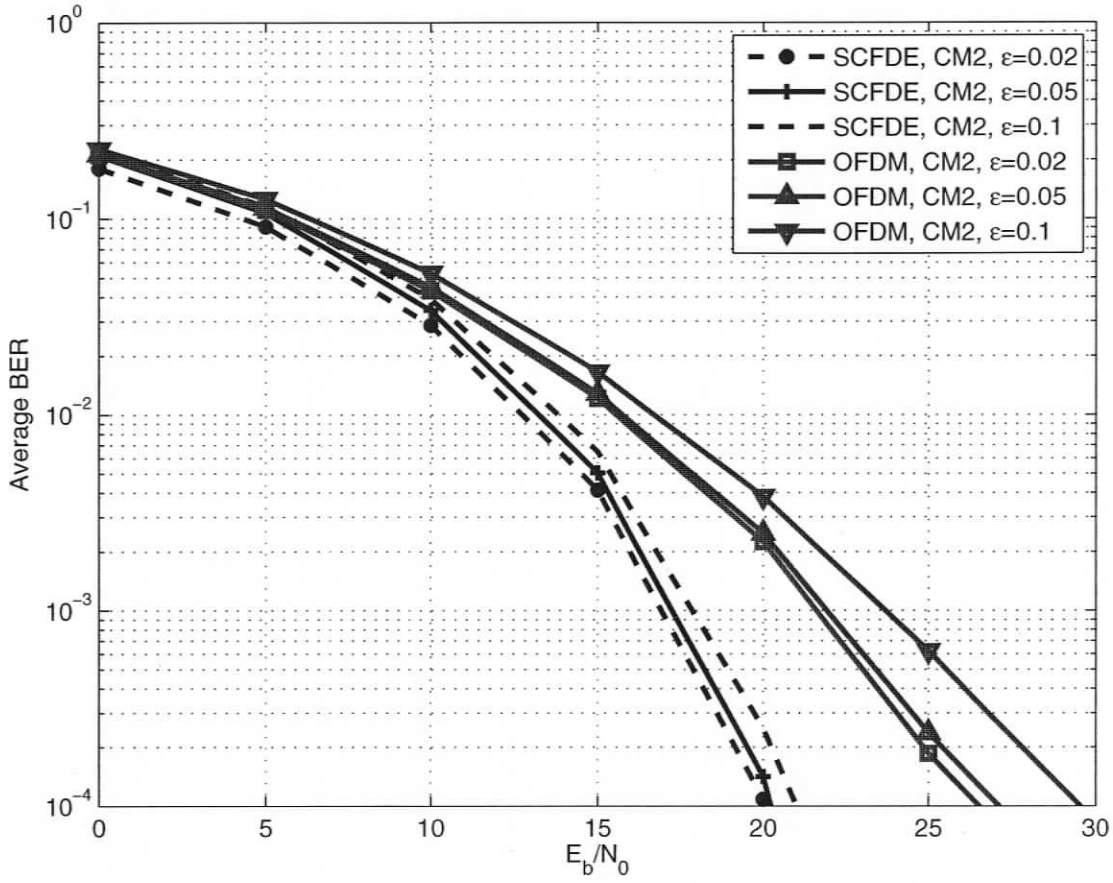

Figure 7.7. *BER of SC-FDE and OFDM over UWB channel CM2 in the presence of CFO* $\varepsilon = 0.02$, $\varepsilon = 0.05$ *and* $\varepsilon = 0.1$.

CM2 while the degradation of SC-FDE is around 3 dB. The reason lies in the fact that in an OFDM system, a constant timing offset τ degrades the original transmitted symbol on the nth carrier x_n by a factor of $e^{\frac{j2\pi n\tau}{N}}$ [55], while SC-FDE does not suffer from such degradation induced by STO. This advantage of SC-FDE, however, diminishes when timing jitter is considered. As can be observed in Figs. 7.12-7.13, although a very small timing jitter uniformly distributed between 0 to $2\Delta t = 0.12$ ns results in slight performance degradation for both systems, severe performance degradation can be observed in both systems when the timing jitter range is larger, e.g., from 0 to $5\Delta t = 0.33$ ns. For OFDM, a uniform timing

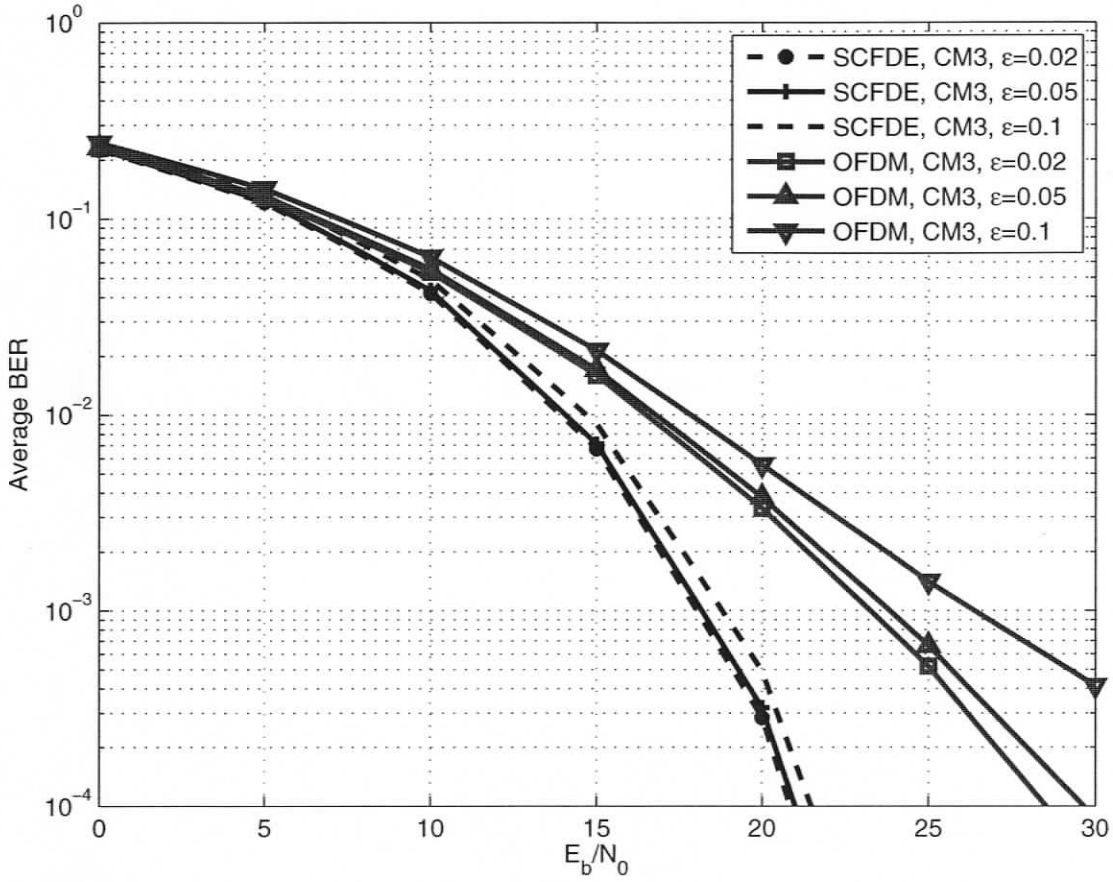

Figure 7.8. *BER of SC-FDE and OFDM over UWB channel CM3 in the presence of CFO* $\varepsilon = 0.02$, $\varepsilon = 0.05$ *and* $\varepsilon = 0.1$.

jitter between 0 to 0.33 ns always underperforms a constant timing offset of 0.33 ns. This is because timing jitter causes ICI in an OFDM system [56]. For SC-FDE, the corresponding two curves cross at around 16 dB in CM2 and CM3. At high SNRs, SC-FDE shows a large error floor in the presence of timing jitter.

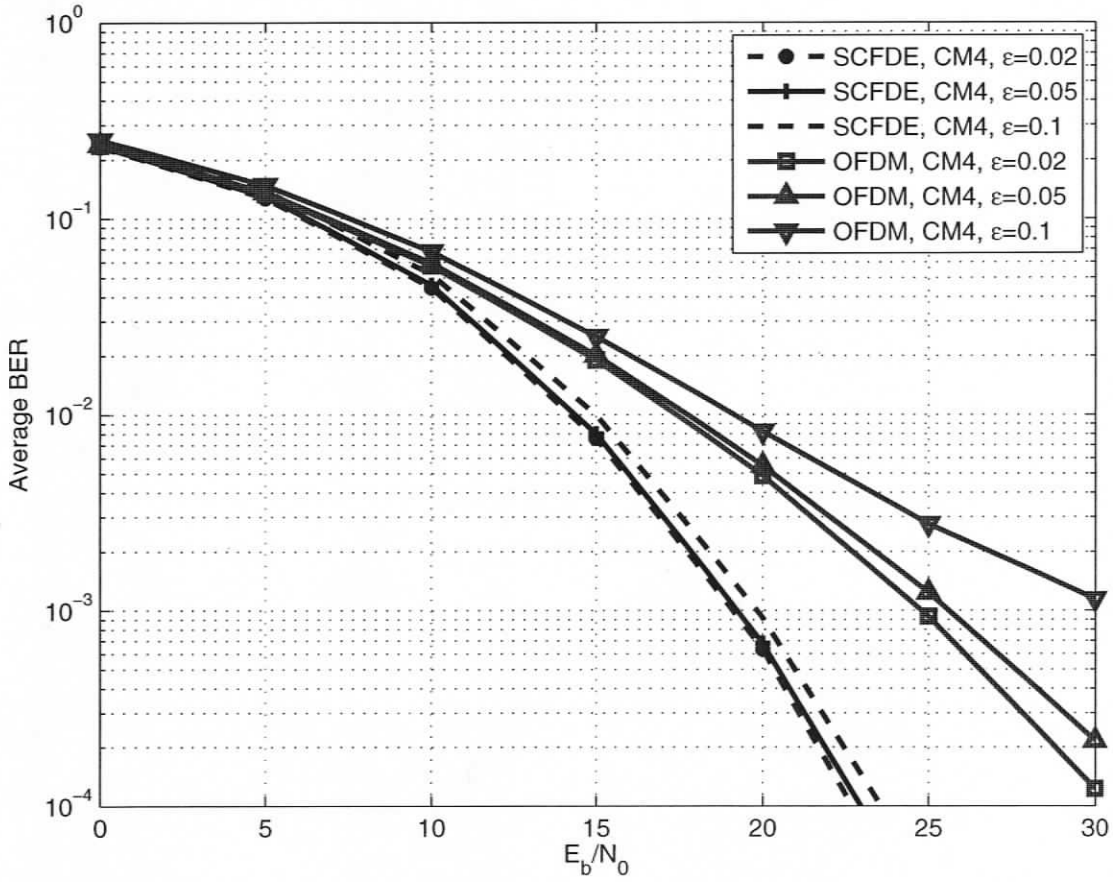

Figure 7.9. *BER of SC-FDE and OFDM over UWB channel CM4 in the presence of CFO* $\varepsilon = 0.02$, $\varepsilon = 0.05$ *and* $\varepsilon = 0.1$.

7.6 Summary

The effects of CFO and STO on the performance of single carrier block transmission with frequency domain MMSE equalization over UWB channels have been investigated. The SINR of SC-FDE in the presence of CFO is derived, numerically calculated and compared with OFDM. Our results have shown that while both systems suffer from a performance degradation in the presence of CFO, OFDM is more sensitive to it. Similar BER performance behavior has been observed for comparison. The effect of a constant STO on the

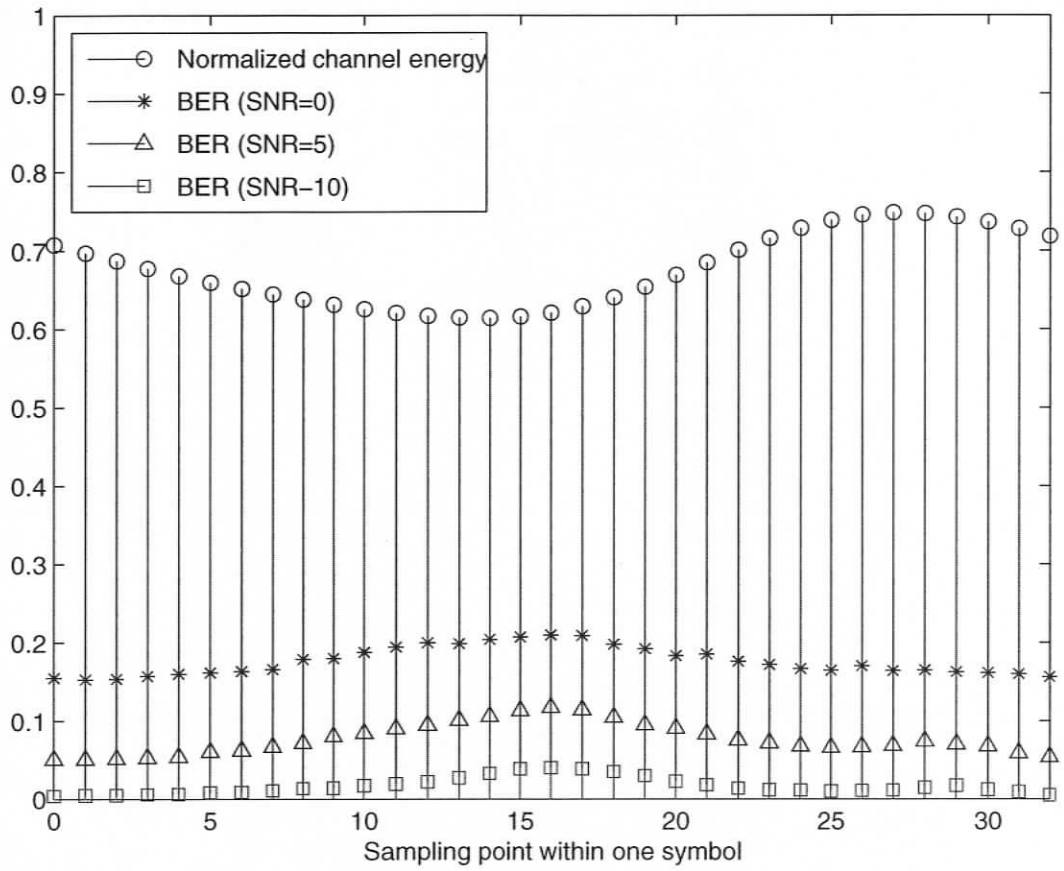

Figure 7.10. *Effects of STO on the performance of SC-FDE UWB over channel realization 1, CM4.*

performance of SC-FDE has been investigated. Our results show that the performance of SC-FDE under a constant timing offset depends on the energy of the sampled equivalent channel captured at the sampling point. However, an SC-FDE system can be fairly sensitive to a uniformly distributed timing jitter, where severe performance degradation can be observed where there is a larger jitter range, especially at high SNRs.

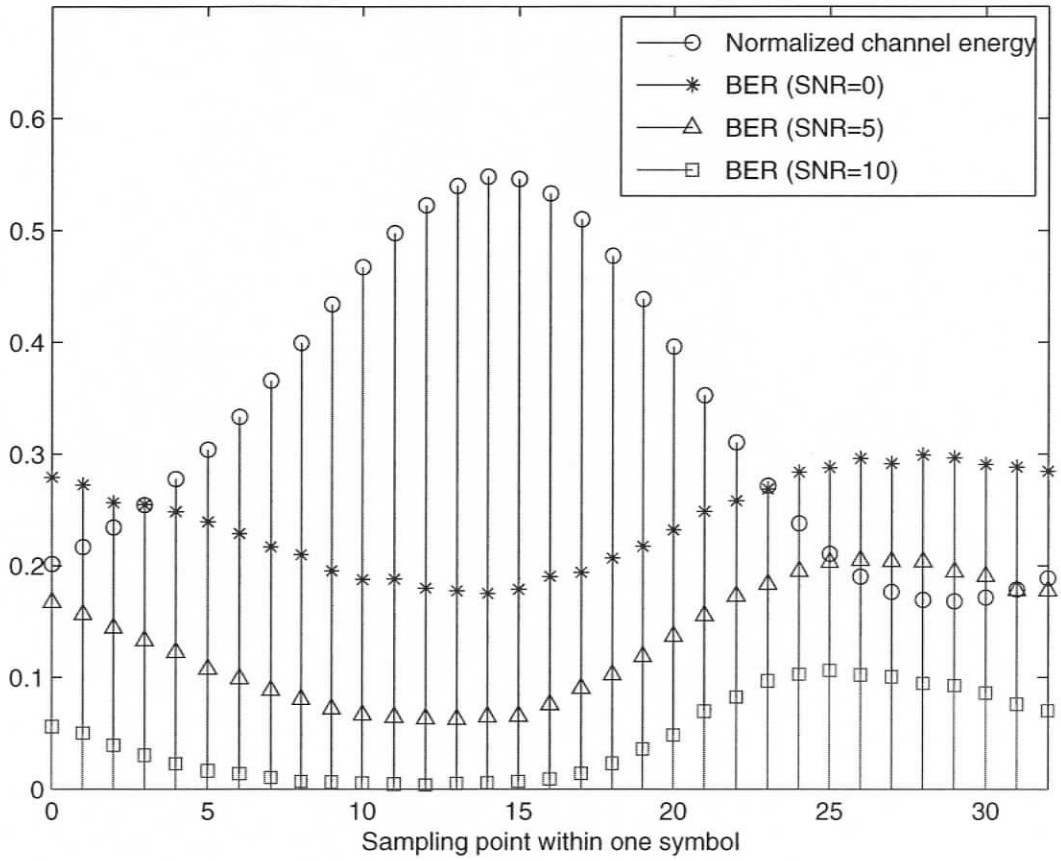

Figure 7.11. *Effects of STO on the performance of SC-FDE UWB over channel realization 50, CM1.*

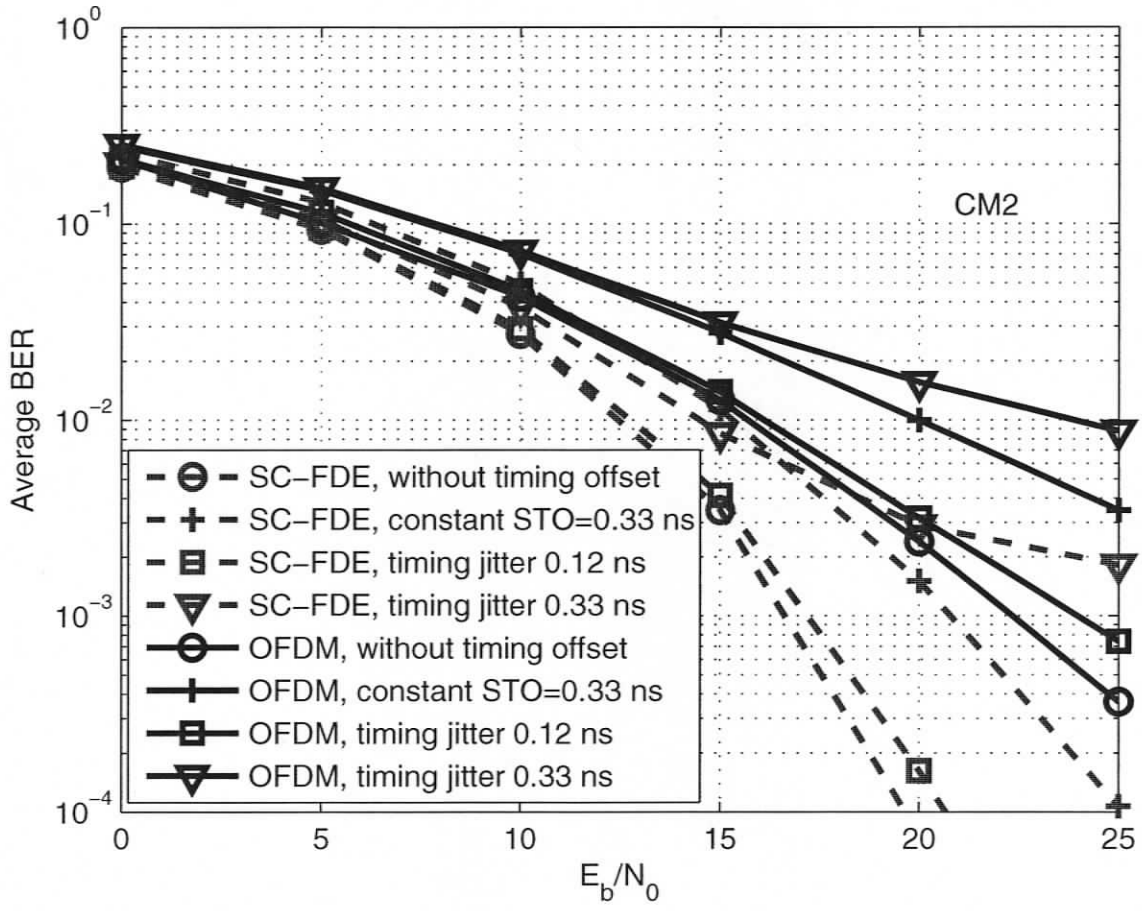

Figure 7.12. *BER performance of SC-FDE UWB over UWB channel model CM2 with timing offset $\tau = 5$ (0.33 ns), and timing jitter 0.33 ns and 0.12 ns*

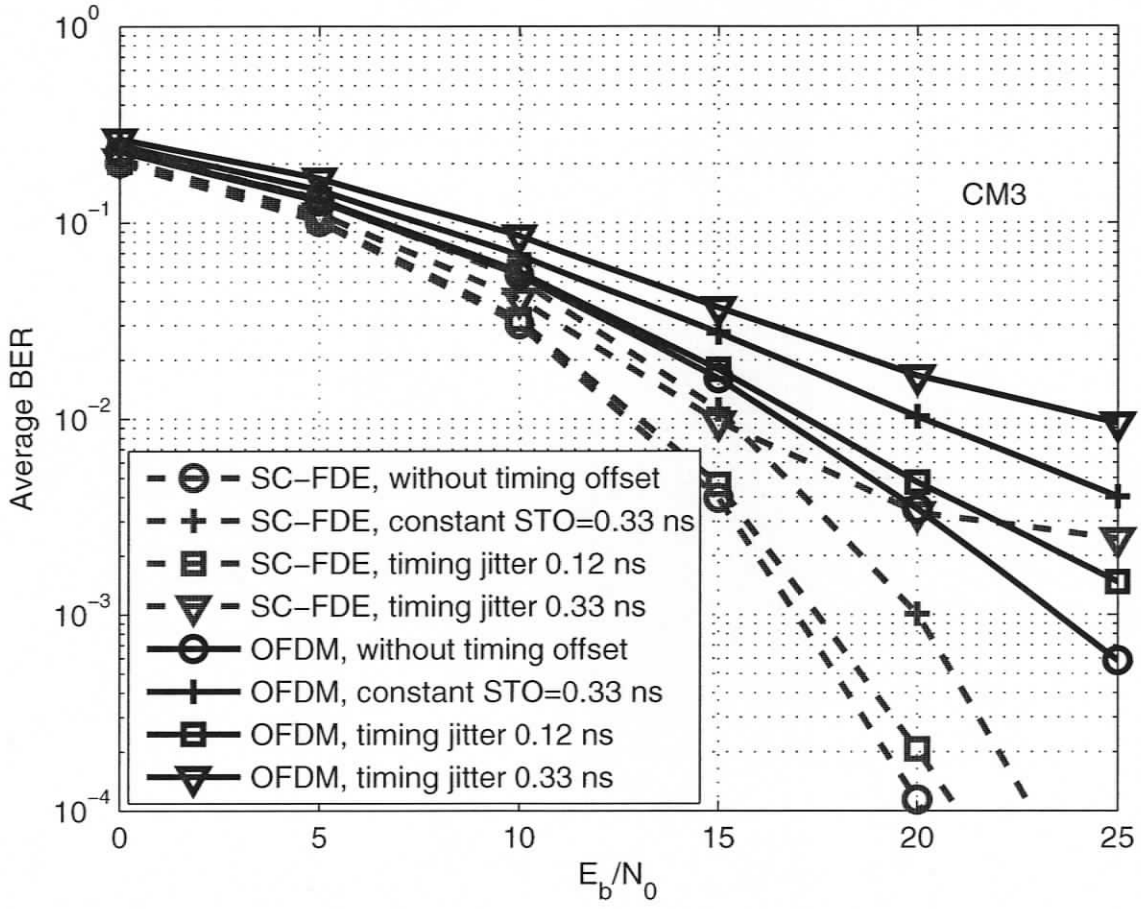

Figure 7.13. *BER performance of SC-FDE UWB over UWB channel model CM3 with timing offset $\tau = 5$ (0.33 ns), and timing jitter 0.33 ns and 0.12 ns*

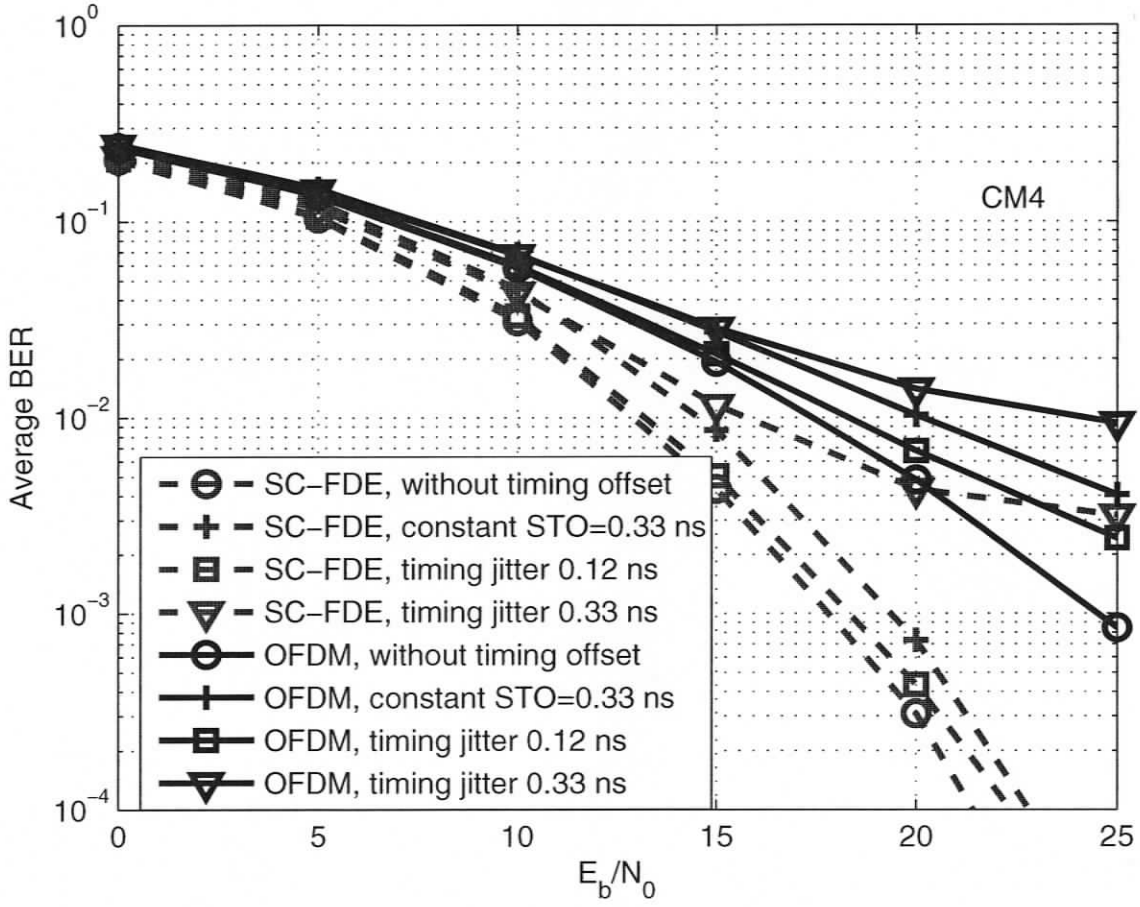

Figure 7.14. *BER performance of SC-FDE UWB over UWB channel model CM4 with timing offset $\tau = 5$ (0.33 ns), and timing jitter 0.33 ns and 0.12 ns*

Chapter 8

Conclusions and Future Work

8.1 Conclusions

UWB physical layer design is a challenging issue due to its high data rate and low complexity requirement. The principle objective of this thesis is to investigate a new transmission and detection scheme, namely SC-FDE, over the IEEE 802.15.3a UWB propagation channels that could possibly achieve a high data rate transmission with a low system complexity, compared to the currently existing high speed UWB technologies, i.e., OFDM-UWB and IR-UWB.

The novelty of SC-FDE UWB compared to the currently proposed IR-UWB and OFDM-UWB is summarized as follows.

1) Unlike IR-UWB where usually extremely narrow pulses are used to transmit data with a large separation between pulses, SC-FDE UWB transmits the signals with full duty cycle pulses consecutively over the channel.

2) Unlike OFDM-UWB where the signal is converted to the time domain by IFFT operator at the transmitter, SC-FDE UWB performs IFFT at the receiver.

3) Unlike OFDM-UWB and IR-UWB where frequency-domain zero-forcing equalization or rake reception are used at the receiver respectively, SC-FDE UWB employs frequency-domain MMSE equalization to eliminate the inter-symbol interference.

The differences in the transmission and detection of SC-FDE have led to several ad-

vantages of SC-FDE over both OFDM-UWB and IR-UWB in the IEEE 802.15.3a UWB communications environment.

The superiority of SC-FDE UWB to OFDM-UWB is summarized as follows.

1) Since SC-FDE is less sensitive to the spectral nulls presented in a frequency selective channel, SC-FDE demonstrates a significant performance superiority to OFDM by around 3-dB without coding when frequency domain MMSE equalization is utilized.

2) SC-FDE has a much simpler transmitter than OFDM, thus allowing a low cost, transmission-only device.

3) More importantly, by performing the IFFT at the receiver, SC-FDE avoids the inherent high PAPR issue at an OFDM transmitter, which is particularly critical to the low cost requirement for UWB since high PAPR at an OFDM transmitter will lead to significantly more expensive power amplifier with high DC power consumption.

The superiority of SC-FDE UWB to IR-UWB is summarized as follows.

1) SC-FDE outperforms IR-UWB by around 5dB in a majority of UWB channels, except strong LOS channels with small delay spread.

2) Using full duty cycle pulse to transmit data, to achieve the same data rate, relative to IR-UWB, SC-FDE UWB allows a wider pulse to transmit for each symbol. This is important because narrower pulse width indicates more expensive pulse generator and higher speed sampling rate ADC that might be too costly for the current CMOS technology.

3) The one-tap frequency-domain equalizer allows SC-FDE UWB to have a much simpler receiver structure than IR-UWB that requires a large number of rake fingers and time-domain equalizer taps to achieve a reasonable performance.

The novel contributions of this thesis on the system design of SC-FDE UWB system are summarized as follows.

1) A novel oversampling diversity scheme has been proposed.

2) A novel low complexity frequency-domain channel estimation scheme has been pro-

posed.

3) A novel low complexity TDMA scheme to address the multiple access issue of SC-FDE UWB has been proposed.

4) A pulse shaping design method to fit the FCC regulation and introduce spectral nulls to limit interference with narrowband signals has been proposed and has been shown to effectively suppress the NBI.

In addition, analysis of the effects of imperfect system parameters on the performance of SC-FDE UWB have been carried out.

1) The effect of channel estimation errors on the performance of SC-FDE UWB has been investigated.

2) The effects of carrier frequency offset and sampling time offset on the performance of SC-FDE UWB have been investigated.

8.2 Future Work

The advantages of SC-FDE over IEEE 802.15.3a UWB channels have been demonstrated in this thesis, together with the investigation of system design problems of SC-FDE UWB. However, some critical issues and more in-depth research work are required to be carried out as an improvement of the current SC-FDE system. The future work based on the SC-FDE UWB system is proposed as follows.

1) Timing estimation and synchronization scheme. It is well known that an effective and efficient synchronization scheme is critical for a communication system to achieve a reasonable system performance. As we showed in Chapter 7 that the performance degradation due to sampling timing offset can vary from 10^{-2} to 10^{-1}. This performance degradation is extremely harmful at high SNRs with BER levels at 10^{-5}. Therefore, to carry out an accurate timing estimation and synchronization scheme at reasonable complexity will be a significant contribution to this work. Another level of synchronization need to be considered is the frame synchronization scheme. As we have discussed in Chapter 4, the TDMA

scheme we proposed is based on the assumption that block boundaries of all users are synchronized. However, this requires a perfect frame synchronization scheme among users; Otherwise MAI will occur. Therefore, it would be also important to investigate the frame synchronization scheme among different users.

2) Carrier estimation and compensation. Also as shown in Chapter 7, carrier frequency offset is an important factor that affects the performance of SC-FDE over UWB channels. Therefore, practical frequency offsets estimation and compensation algorithms need to be carried out.

3) Further analysis of the effect of timing jitter on the performance of SC-FDE UWB. In our work the analysis of the performance of SC-FDE with sampling time offset is investigated based on a constant shift from the optimal sampling instant. In a more practical scenario, the timing shift can be modeled as a random variable, referred to as the timing jitter. Although we simulated the performance of SC-FDE with timing jitter over IEEE 802.15.3a UWB channels, further analysis to explain the performance degradation occurs would be an interesting topic.

4) Sensor networks. As an emerging worldwide standard for low power, high throughput local wireless communications, UWB has been shown to be a promising physical layer candidate for sensor networks because of its inherent support for some of the important requirements - throughput governed adaptive communication range, low power, and low cost. It would therefore be interesting to carry out research on the high-speed wireless sensor networks and investigate the design to realize the benefits of UWB in the sensor networks.

Bibliography

[1] *FCC Document 00-163: Revision of part 15 of the Commission's rules regarding ultra-wideband transmission systems*, Apr. 2002.

[2] J. Foerster, *Channel Modeling Subcommittee Report (Final)*, IEEE P802.15.3a Working Group, P802.15-03/02490r1-SG3a, Feb. 2003.

[3] H. Zhang, T. Udagawa, T. Arita, and M. Nakagawa, "Home entertainment network: combination of ieee 1394 and ultra wideband solutions," in *IEEE Conference on Ultra Wideband Systems and Technology*, May 2002, pp. 144–145.

[4] V. Somayazulu, J. R. Foerster, and S. Roy, "Design challenges for very high data rate UWB systems," in *Systems and Computers, Conference Record of the Thirty-Sixth Asilomar Conference on*, vol. 1, Nov. 2002, pp. 717–721.

[5] *DS-UWB Physical Layer Submission to 802.15 Task Group 3a*, IEEE P802.15.3a Working Group, P802.15-04/0137r3, July 2004.

[6] *Multi-band OFDM Physical Layer Proposal for IEEE 802.15 Task Group 3a*, IEEE P802.15.3a Working Group, P802.15-03/268r2, Nov. 2003.

[7] *DS-CDMA: The Technology Of Choice For UWB*, IEEE P802.15.3a Working Group, P802.15-03/277r0, July 2003.

[8] Y. (Geoffrey) Li, A. F. Molisch, and J. Y. Zhang, "Channel estimation and signal detection for UWB," in *Proc. of the 6th International Symposium on Wireless Personal Multimedia Communications (WPMC03)*, Oct. 2003.

[9] A. H. Tewfik and E. Saberinia, "High bit rate ultra-wideband OFDM," in *Proc. IEEE GlOBECOM*, vol. 3, Nov. 2002, pp. 2260–2264.

[10] E. Saberinia and A. H. Tewfik, "All-digital receiver structures for MC-UWB systems," in *Proc. IEEE VTC*, vol. 1, Oct. 2003, pp. 289–293.

[11] H. Sari, G. Karam, and I. Jeanclaude, "Transmission techniques for digital terrestrial TV broadcasting," *IEEE Commun. Mag.*, vol. 33, pp. 100–109, Feb. 1995.

[12] A. Czylwik, "Comparison between adaptive ofdm and single carrier modulation with frequency domain equalization," in *Proc. IEEE VTC*, vol. 2, May 1997, pp. 865–869.

[13] D. Falconer, S. L. Ariyavisitakul, A. B. Seeyar, and B. Eidson, "Frequency domain

equalization for single-carrier broadband wireless systems," *IEEE Commun. Mag.*, vol. 40, pp. 58–66, Apr. 2002.

[14] J. Tubbax, B. Come, and L. V. Perre, "OFDM versus single carrier with cyclic prefix: a system-based comparison," in *Proc. IEEE VTC*, vol. 2, Oct. 2001, pp. 1115–1119.

[15] Z. Wang, X. Ma, and G. B. Giannakis, "OFDM or single-carrier block transmission," *IEEE Trans. Commun.*, vol. 52, pp. 380–394, Mar. 2004.

[16] J. Louveaux, L. Vandendorpe, and T. Sartenaer, "Cyclic prefixed single carrier and multicarrier transmission: Bit rate comparison," *IEEE Commun. Lett.*, vol. 7, pp. 180–182, Apr. 2003.

[17] N. C. Beaulieu, "The evaluation of error probabilities for intersymbol and cochannel interference," *IEEE Trans. Commun.*, vol. 39, pp. 1740–1749, Dec. 1991.

[18] H. V. Poor and S. Verdu, "Probability of error in MMSE multiuser detection," *IEEE Trans. Inform. Theory*, vol. 43, pp. 858–871, May 1997.

[19] J. Zhang, E. K. Chong, and D. N. C. Tse, "Output MAI distributions of linear MMSE multiuser receivers in DS-CDMA systems," *IEEE Trans. Inform. Theory*, vol. 47, pp. 1128–1144, Mar. 2001.

[20] J. G. Proakis, *Digital Communications*. Fourth Edition, New York, NY: McGraw-Hill, 2001.

[21] W. H. Press, S. A. Teukolsky, W. T. Vetterling, and B. P. Flannery, *Numerical Recipes in C++*. Cambridge: Cambridge University Press, 2002.

[22] A. Gusmao, R. Dinis, and N. Esteves, "On frequency-domain equalization and diversity combining for broadband wireless communications," *IEEE Commun. Lett.*, vol. 51, pp. 1029–1033, July 2003.

[23] V. Lottici, A. D'Andrea, and U. Mengali, "Channel estimation for ultra-wideband communications," *IEEE J. Select. Areas Commun.*, vol. 20, pp. 1638–1645, Dec. 2002.

[24] C. Tellambura, M. G. Parker, Y. J. Guo, S. J. Shepherd, and S. K. Barton, "Optimal sequences for channel estimation using Discrete Fourier Transform techniques," *IEEE Trans. Commun.*, vol. 47, pp. 230–238, Feb. 1999.

[25] W. Chen and U. Mitra, "Frequency domain versus time domain based training sequence optimization," in *Proc. IEEE ICC*, vol. 2, June 2000, pp. 646–650.

[26] I. Barhumi, G. Leus, and M. Moonen;, "Optimal training design for MIMO OFDM systems in mobile wireless channels," *IEEE Trans. Signal Processing*, vol. 51, pp. 1615 – 1624, June 2003.

[27] M. Morelli and U. Mengali;, "A comparison of pilot-aided channel estimation meth-

ods for OFDM systems," *IEEE Trans. Signal Processing*, vol. 49, pp. 3065 – 3073, Dec. 2001.

[28] J. J. Beek, O. Edfors, and M. Sandell, "On channel estimation in OFDM systems," *VTC'95*, vol. 2, pp. 815–819, July 1995.

[29] O. Edfors, M. Sandell, J. J. van de Beek, S. K. Wilson, and P. O. Borjesson, "OFDM channel estimation by singular value decomposition," *IEEE Trans. Commun.*, vol. 46, pp. 931–939, July 1998.

[30] S. M. Kay, *Fundamentals of statistical signal processing-Estimation theory*. New Jersey: Prentice-Hall, 1993.

[31] J. Mottonen, V. Koivunen, and H. Oja;, "Robust autocovariance estimation based on sign and rank correlation coefficients," in *IEEE Signal Proceeding workshop on higher statistics*, vol. 14-16, June 19979, pp. 187–190.

[32] Q. Li and L. A. Rusch, "Multiuser detection for DS-CDMA UWB in the home environment," *IEEE J. Select. Areas Commun.*, vol. 20, pp. 1701–1711, Dec. 2002.

[33] Y. Tang and B. Vucetic, "The FFT-based multiuser detection for DS-CDMA ultra-wideband communication systems," *Proc. of the Ultra Wideband Systems, 2004*, vol. WA4-5, pp. 111–115, May 2004.

[34] S. Zhou, G. B. Giannakis, and C. L. Martret, "Chip-interleaved block-spread code division multiple access," *IEEE Trans. Commun.*, vol. 50, pp. 235–248, Feb. 2002.

[35] J. Brewer, "Kronecker products and matrix calculus in system theory," *IEEE Trans. Circuits Syst.*, vol. 25, pp. 772–781, Sept. 1978.

[36] J. Bellorado, S. S. Ghassemzadeh, L. J. Greenstein, T. Sveinsson, and V. Tarokh, "Coexistence of ultra-wideband systems with IEEE 802.11a wireless LANs," in *Proc. IEEE GLOBECOM*, vol. 1, Dec. 2003, pp. 410–414.

[37] Wisair, "Detect and avoid technology for ultra wideband (UWB) spectrum usage," *white paper*. [Online]. Available: http://www.wisair.com/wp−content/DAA_WP.pdf

[38] Z. Luo, H. Gao, Y. Liu, and J. Gao, "A new UWB pulse design method for narrowband interference suppression," in *Proc. IEEE GLOBECOM*, vol. 6, Dec. 2004, pp. 3488 – 3492.

[39] Y. Wu, A. F. Molisch, S. Y. Kung, and J. Zhang, "Impulse radio pulse shaping for ultra-wide bandwidth (UWB) systems," in *Proc. IEEE PIMRC*, vol. 1, Sept. 2003, pp. 877–881.

[40] X. Wu, Z. Tian, T. N. Davidson, and G. B. Giannakis, "Optimum waveform design for uwb radios," *IEEE Trans. Signal Processing, to appear*.

[41] I. J. Fair, "Construction of codewords and pulse shapes to meet spectral requirements," *ICC'2006, to appear.*

[42] G. Cariolaro and G. Tronca, "Spectra of block coded digital signals," *IEEE Trans. Commun.*, vol. 22, pp. 1555–1564, Oct. 1974.

[43] X. Chu and R. D. Murch, "The effect of NBI on UWB time-hopping systems," *IEEE Trans. Wireless Commun.*, vol. 3, pp. 1431–1436, Sept. 2004.

[44] S. K. Wilson and J. M. Cioffi, "Probability density functions for analyzing multi-amplitude constellations in Rayleigh and Ricean channels," *IEEE Trans. Commun.*, vol. 47, pp. 380–386, Mar. 1999.

[45] Y. Ma, R. Schober, and S. Pasupathy, "Effect of imperfect channel estimation on MRC diversity in fading channels," in *Proc. IEEE ICC'03*, vol. 6, June 2024, pp. 3163 – 3167.

[46] X. Dong and N. C. Beaulieu, "SER of two-dimensional signalings in rayleigh fading with channel estimation errors," in *Proc. IEEE ICC'03*, vol. 4, May 2003, pp. 2763 – 2767.

[47] X. Dong and L. Xiao, "Symbol error probability of two-dimensional signaling in Ricean fading with imperfect channel estimation," *IEEE Trans. Veh. Technol.*, accepted for publication.

[48] A. Papoulis, *Probability, Random variables, and stochastic processes.* New York, NY: McGraw-Hill, 1991.

[49] T. Pollet, M. Bladel, and M. Moeneclaey, "Ber sensitivity of OFDM systems to carrier frequency offset and wiener phase noise," *IEEE Trans. Commun.*, vol. 43, pp. 191–193, Feb.-Apr. 1995.

[50] K. Sathananthan and C. Tellambura, "Probability of error calculation of OFDM systems with frequency offset," *IEEE Trans. Commun.*, vol. 49, pp. 1884–1888, Nov. 2001.

[51] Y. Han, H. Huh, and J. Krogmerier, "Comparison of error probability for OFDM and SC-FDE," in *Proc. of IEEE Conference Record of the Thirty-Seventh Asilomar Conference on Signals, Systems and Computers*, vol. 1, Nov. 2003, pp. 497–501.

[52] T. Pollet and M. Moeneclaey, "The effect of carrier frequency offset on the performance of band limited single carrier and OFDM signals," in *Proc. IEEE GLOBECOME*, vol. 1, Nov. 1996, pp. 719–723.

[53] X. Ma, H. Kobayashi, and S. Schwartz, "Effect of frequency offset on BER of OFDM and single carrier systems," in *Proc. IEEE PIMRC*, vol. 3, Sept. 2003, pp. 2239–2243.

[54] F. Horlin, S. D. Rore, E. Lopez-Estraviz, F. Naessens, and L. V. der Perre, "MC-

CDMA performance in the presence of carrier frequency offset, sample clock offset and IQ imbalance," in *Proc. IEEE GLOBECOM*, vol. 6, Nov. 2005, pp. 3206 – 3210.

[55] I. Arsic, V. Stankovic, D. Drajic, and Z. Nikolic, "Performance of the OFDM system," *IEEE Telecommunications in Modern Satellite, Cable and Broadcasting Service*, vol. 2, pp. 767 – 768, Sept. 2001.

[56] O. Uzoma and Y. Li, "Effect of timing jitter on OFDM based UWB systems," *IEEE J. Select. Areas Commun.*, to appear. Apr. 2006.

[57] Z. Wang and G. B. Giannakis, "Wireless multicarrier communications: where fourier meets shannon," *IEEE Signal Processing Mag.*, vol. 17, pp. 29–48, May 2000.

[58] Y. Wang, X. Dong, P. H. Wittke, and S. Mo, "Cyclic prefixed single carrier transmission in ultra-wideband communications," *IEEE Trans. Wireless Commun., to appear.*

[59] R. A. Horn and C. R. Johnson, *Matrix analysis*. Cambridge: Cambridge University Press, 1999.

Appendix A

In this Appendix, we show the rationality of the assumption that $\mathbf{R_{HH}}$ is positive definite. Denote the auto-correlation matrix of the time-domain channel taps $\tilde{\mathbf{h}}$ as $\mathbf{R}_{\tilde{\mathbf{h}}\tilde{\mathbf{h}}}$, that is, $\mathbf{R}_{\tilde{\mathbf{h}}\tilde{\mathbf{h}}} = \mathbb{E}[\tilde{\mathbf{h}}\tilde{\mathbf{h}}^H]$ which is a real symmetric matrix and therefore can be diagonalized as [59]

$$\mathbf{R}_{\tilde{\mathbf{h}}\tilde{\mathbf{h}}} = \mathbf{V}\Lambda_{\tilde{\mathbf{h}}}\mathbf{V}^T \tag{A.1}$$

where $\mathbf{V} \in \mathbb{M}_N$ is a unitary matrix and $\Lambda_{\tilde{\mathbf{h}}}$ is a diagonal matrix with eigenvalues $\lambda_{\tilde{\mathbf{h}}_i}, i = 0,1,\cdots,N-1$ of $\mathbf{R}_{\tilde{\mathbf{h}}\tilde{\mathbf{h}}}$ on its diagonal. Furthermore, $\mathbf{R}_{\tilde{\mathbf{h}}\tilde{\mathbf{h}}}$ is also positive semi-definite since it is an auto-correlation matrix [48]. We assume that some of the eigenvalues in $\lambda_{\tilde{\mathbf{h}}_i}, i = 0,1,\cdots,N-1$, equal to zero. Denote $\Lambda'_{\tilde{\mathbf{h}}}$ as the diagonal matrix with its ith diagonal entry substituted by δ for $\lambda_{\tilde{\mathbf{h}}_i} = 0$. That is,

$$\lambda'_{\tilde{\mathbf{h}}_i} = \begin{cases} \lambda_{\tilde{\mathbf{h}}_i} & \text{for } \lambda_{\tilde{\mathbf{h}}_i} > 0 \\ \delta & \text{for } \lambda_{\tilde{\mathbf{h}}_i} = 0 \end{cases} \tag{A.2}$$

where δ is chosen to be a small positive value that can be as close to zero as possible. Therefore, the positive definite counterpart of the positive semi-definite matrix $\mathbf{R}_{\tilde{\mathbf{h}}\tilde{\mathbf{h}}}$ can be obtained as

$$\mathbf{R}'_{\tilde{\mathbf{h}}\tilde{\mathbf{h}}} = \mathbf{V}\Lambda'_{\tilde{\mathbf{h}}}\mathbf{V}^T \tag{A.3}$$

with its (m,n)th element as $\sum_{i=0}^{N-1} \lambda'_{\tilde{\mathbf{h}}_i} v_{mi} v_{ni}$. Since $\mathbf{V}$ is the unitary matrix, we have $v_{ij} \leq 1$. Therefore, the difference between each element in $\mathbf{R}_{\tilde{\mathbf{h}}\tilde{\mathbf{h}}}$ and $\mathbf{R}'_{\tilde{\mathbf{h}}\tilde{\mathbf{h}}}$ due to the substitution of zero eigenvalues by δ will be no more than $m\delta$, where m is the number of zero eigenvalues of $\mathbf{R}_{\tilde{\mathbf{h}}\tilde{\mathbf{h}}}$. As long as δ is chosen to be small enough, the difference between $\mathbf{R}_{\tilde{\mathbf{h}}\tilde{\mathbf{h}}}$ and $\mathbf{R}'_{\tilde{\mathbf{h}}\tilde{\mathbf{h}}}$ is negligible. Therefore, for analysis purpose, it is reasonable to assume the time-domain

channel auto-correlation matrix $\mathrm{R}_{\tilde{\mathbf{h}}\tilde{\mathbf{h}}}$ as positive definite, with positive eigenvalues $\lambda'_{\tilde{\mathbf{h}}_i}$ for $i = 0, 1, \cdots, N-1$. Following (A.1), we have

$$\mathrm{R}_{\mathbf{HH}} = N\mathbf{F}\mathrm{R}_{\tilde{\mathbf{h}}\tilde{\mathbf{h}}}\mathbf{F}^H = \mathbf{U}\Lambda_{\mathbf{H}}\mathbf{U}^H \tag{A.4}$$

where $\mathbf{U} \in \mathbb{M}_N$ and $\mathbf{U} = \mathbf{FV}$ is a unitary matrix. Moreover, $\Lambda_{\mathbf{H}}$ is a diagonal matrix with the eigenvalues of $\mathrm{R}_{\mathbf{HH}}$ as $\lambda_i = N\lambda'_{\tilde{\mathbf{h}}_i} > 0$ for $i = 0, 1, \cdots N-1$. Therefore, $\mathrm{R}_{\mathbf{HH}}$ is also positive definite.

Appendix B

It is well known that the inverse of an $N \times N$ matrix $\mathbf{x}$ is $\frac{\mathbf{x}\dagger}{\det(\mathbf{x})}$, where $\mathbf{x}\dagger$ is the $N \times N$ matrix with its (i,j)-th element given by the (i,j)-th cofactor of $\mathbf{x}$. Accordingly, we have

$$\mathbb{T}\mathrm{r}\left\{\mathbf{W}^{-1}\right\} = \frac{1}{\det(\mathbf{W})}\left(\det(\mathbf{W}_1) + \det(\mathbf{W}_2) + \cdots + \det(\mathbf{W}_N)\right) \tag{B.1}$$

where $\mathbf{W}_i \in \mathbb{M}_{N-1}$ is the principle submatrix of $\mathbf{W}$ obtained by deleting the ith row and column of matrix $\mathbf{W}$, which is defined in Appendix C.

The Bergstrom's inequality states that [59]

$$\frac{\det(\mathbf{A}+\mathbf{B})}{\det(\mathbf{A}_i+\mathbf{B}_i)} \geq \frac{\det(\mathbf{A})}{\det(\mathbf{A}_i)} + \frac{\det(\mathbf{B})}{\det(\mathbf{B}_i)} \quad i = 0, \cdots N-1, \tag{B.2}$$

is valid for any positive definite matrix $\mathbf{A}, \mathbf{B} \in \mathbb{M}_N$, where $\mathbf{A}_i \in \mathbb{M}_{N-1}$ denotes the principle submatrix of $\mathbf{A}$ obtained by deleting the ith row and column of $\mathbf{A}$, and similarly for $\mathbf{B}_i$. Furthermore, the equality holds when $\mathbf{A}$ and $\mathbf{B}$ are diagonal.

Following (C), we denote matrix $\mathbf{W}$ as

$$\mathbf{W} = \mathbf{A} + \mathbf{B}, \tag{B.3}$$

where $\mathbf{A}$, $\mathbf{B}$ are

$$\mathbf{A} = \Lambda_{\mathbf{H}}^{-1} \tag{B.4}$$

and

$$\mathbf{B} = \Lambda_{\mathbf{H}}^{-1}\mathbf{U}^H\sigma_n^2(\mathbf{P}^H\mathbf{P})^{-1}\mathbf{U}\Lambda_{\mathbf{H}}^{-1} \tag{B.5}$$

respectively. Matrix $\mathbf{A}$ is real and positive definite since λ_i is positive and real as in Appendix A. Also, matrix $\mathbf{B}$ is positive definite since for all nonzero column vector $\mathbf{z}$, we

have

$$\begin{aligned} \mathbf{z}^H\mathbf{B}\mathbf{z} &= (\Lambda_{\mathbf{H}}^{-1}\mathbf{z})^H\mathbf{M}\Lambda_{\mathbf{H}}^{-1}\mathbf{z} \\ &= \mathbf{y}^H\mathbf{M}\mathbf{y} \\ &> 0, \end{aligned} \tag{B.6}$$

where $\mathbf{y} = \Lambda_{\mathbf{H}}^{-1}\mathbf{z}$, $\mathbf{M} = \mathbf{U}^H\sigma_n^2(\mathbf{P}^H\mathbf{P})^{-1}\mathbf{U}$. The inequality in (B.6) is due to the fact that $\mathbf{M}$ is positive definite with the ith eigenvalue being $\frac{\sigma_n^2}{|P_i|^2} > 0$.

Furthermore, it is straightforward to see that

$$\frac{\det(\mathbf{A})}{\det(\mathbf{A}_i)} = \frac{1}{\lambda_i} > 0, \text{ for } i = 0, 1, \cdots N-1. \tag{B.7}$$

We also show in Appendix C that

$$\frac{\det(\mathbf{B})}{\det(\mathbf{B}_i)} > 0, \text{ for } i = 0, 1, \cdots N-1. \tag{B.8}$$

Therefore,

$$\frac{\det(\mathbf{A}+\mathbf{B})}{\det(\mathbf{A}_i+\mathbf{B}_i)} \geq \frac{\det(\mathbf{A})}{\det(\mathbf{A}_i)} + \frac{\det(\mathbf{B})}{\det(\mathbf{B}_i)} > 0, \text{ for } i = 0, 1, \cdots N-1. \tag{B.9}$$

Applying the Bergstrom's inequality to eqn. (B.3) and inequality (B.9), we have

$$\frac{\det(\mathbf{W}_i)}{\det(\mathbf{W})} \leq \frac{1}{\frac{\det(\mathbf{A})}{\det(\mathbf{A}_i)} + \frac{\det(\mathbf{B})}{\det(\mathbf{B}_i)}} \tag{B.10}$$

with the maximum achieved when $\mathbf{B}$ is diagonal. This condition satisfies when $|P_i|^2 = c$, where c is a constant for $i = 0, 1, \cdots, N-1$. Applying Parseval's theorem to $\{p_n\}$ and $\{P_k\}$, we have that

$$\sum_{k=0}^{N-1} |P_k|^2 = N. \tag{B.11}$$

Therefore, constant c should be chosen as $c = 1$ for the maximum value in (B.10) to be achieved, or equivalently, $\mathbf{P}^H\mathbf{P} = \mathbf{I}_N$.

Under the condition when equality holds, we have

$$\frac{\det(\mathbf{A})}{\det(\mathbf{A}_i)} = \frac{1}{\lambda_i}, \text{ for } i = 0, 1, \cdots N-1, \tag{B.12}$$

and

$$\frac{\det(\mathbf{B})}{\det(\mathbf{B}_i)} = \frac{\sigma_n^2}{\lambda_i^2}, \text{ for } i = 0, 1, \cdots N-1. \tag{B.13}$$

Following (B.10), (B.12) and (B.13), we have

$$\frac{\det(\mathbf{W}_i)}{\det(\mathbf{W})} \leq \frac{\lambda_i^2}{\lambda_i + \sigma_n^2}, \text{ for } i = 0, 1, \cdots, N-1 \tag{B.14}$$

where the equality holds when $\mathbf{P}^H\mathbf{P} = \mathbf{I}_N$. It follows from (B.1) that

$$\mathbb{T}\mathrm{r}\left\{\mathbf{W}^{-1}\right\} \leq \sum_{i=0}^{N-1} \frac{\lambda_i^2}{\lambda_i + \sigma_n^2} \tag{B.15}$$

where the equality holds when $\mathbf{P}^H\mathbf{P} = I_N$.

Appendix C

In this Appendix, we show that $\frac{\det(\mathbf{B})}{\det(\mathbf{B}_i)} > 0$. It is known that the $\frac{\det(\mathbf{B}_i)}{\det(\mathbf{B})}$ is the ith diagonal entry of matrix $\mathbf{B}^{-1}$ (See Appendix B). Also, from (B.5), we have that the ith diagonal entry of $\mathbf{B}^{-1}$ is $\frac{\sum_{j=0}^{N-1} |u_{ji}|^2 |P_j|^2 \lambda_i^2}{\sigma_n^2} > 0$. Therefore,

$$\frac{\det(\mathbf{B})}{\det(\mathbf{B}_i)} > 0. \tag{C.1}$$

Appendix D

Let's use $\tilde{\mathbf{p}}$ to denote the $N \times L$ column-wise circulant matrix with its first column being the pilot block $\mathbf{p} = [p_0, p_1, p_L, \cdots, p_{N-1}]^H$. The MMSE estimated time-domain channel taps $\hat{\mathbf{h}}$ can be obtained as

$$\hat{\mathbf{h}} = \mathrm{R}_{\mathbf{hh}}(\mathrm{R}_{\mathbf{hh}} + \sigma_n^2(\tilde{\mathbf{p}}^H\tilde{\mathbf{p}})^{-1})^{-1}\tilde{\mathbf{p}}^H\mathbf{y} \tag{D.1}$$

where $\mathrm{R}_{\mathbf{hh}}$ is the correlation matrix of time-domain channel taps, σ_n^2 is the noise variance, $\mathbf{y} = \tilde{\mathbf{p}}\mathbf{h} + \mathbf{n}$ is the received time-domain signal and the MSE lower bound is achieved when $\tilde{\mathbf{p}}^H\tilde{\mathbf{p}} = c\mathbf{I}$, where c is a constant. For simplicity and without loss of generality, we assume $c = 1$. The channel taps obtained by time-domain MMSE estimation can therefore be written as

$$\hat{\mathbf{h}} = \mathrm{R}_{\mathbf{hh}}(\mathrm{R}_{\mathbf{hh}} + \sigma_n^2\mathbf{I})^{-1}\tilde{\mathbf{p}}^H\mathbf{y}. \tag{D.2}$$

Now if we perform FFT on the MMSE estimated time-domain taps, we have

$$\begin{aligned}
\hat{\mathbf{H}} &= \mathbf{F}_{N\times L}\hat{\mathbf{h}} \\
&= \mathbf{F}_{N\times L}\mathrm{R}_{\mathbf{hh}}(\mathrm{R}_{\mathbf{hh}} + \sigma_n^2\mathbf{I})^{-1}\tilde{\mathbf{p}}^H\mathbf{y} \\
&= \mathbf{F}_{N\times L}\mathrm{R}_{\mathbf{hh}}\mathbf{F}_{N\times L}^H(\mathbf{F}_{N\times L}^H)^{-1}(\mathrm{R}_{\mathbf{hh}} + \sigma_n^2\mathbf{I})^{-1}\tilde{\mathbf{p}}^H\mathbf{y}
\end{aligned} \tag{D.3}$$

where $\mathbf{F}_{N\times L}$ is the $N \times L$ dimension matrix containing the first L columns of the Fourier matrix $\mathbf{F}$.

Since

$$\begin{aligned}
\mathrm{R}_{\mathbf{HH}} &= \mathbb{E}\{\mathbf{F}_{N\times L}\mathbf{h}\mathbf{h}^H\mathbf{F}_{N\times L}^H\} \\
&= \mathbf{F}_{N\times L}\mathrm{R}_{\mathbf{hh}}\mathbf{F}_{N\times L}^H
\end{aligned} \tag{D.4}$$

where $\mathrm{R}_{\mathbf{HH}}$ is the frequency-domain channel correlation matrix. Applying (D.3), we have the estimated frequency-domain channel taps

$$\begin{aligned}\hat{\mathbf{H}} &= \mathrm{R}_{\mathbf{HH}}(\mathrm{R}_{\mathbf{hh}}\mathbf{F}_{N\times L}^{H}+\sigma_n^2\mathbf{F}_{N\times L}^{H})^{-1}\tilde{\mathbf{p}}^{H}\mathbf{y}\\ &= \mathrm{R}_{\mathbf{HH}}(\mathbf{F}_{N\times L}^{-1}(\mathbf{F}_{N\times L}\mathrm{R}_{\mathbf{hh}}\mathbf{F}_{N\times L}^{H}+\mathbf{F}_{N\times L}\sigma_n^2\mathbf{F}_{N\times L}^{H}))^{-1}\tilde{\mathbf{p}}^{H}\mathbf{y}\\ &= \mathrm{R}_{\mathbf{HH}}(\mathrm{R}_{\mathbf{HH}}+\sigma_n^2\mathbf{F}_{N\times L}\mathbf{F}_{N\times L}^{H})^{-1}\mathbf{F}_{N\times L}\tilde{\mathbf{p}}^{H}\mathbf{y}. \qquad \text{(D.5)}\end{aligned}$$

Denote

$$\mathbf{Q}_{\mathbf{t}} = \mathrm{R}_{\mathbf{HH}}(\mathrm{R}_{\mathbf{HH}}+\sigma_n^2\mathbf{F}_{N\times L}\mathbf{F}_{N\times L}^{H})^{-1}. \qquad \text{(D.6)}$$

MSE can be written as

$$\begin{aligned}\mathrm{MSE} &= \frac{1}{N}\mathbb{T}\mathrm{r}\{\mathbb{E}[(\mathbf{H}-\hat{\mathbf{H}})(\mathbf{H}-\hat{\mathbf{H}})^{H}]\}\\ &= \frac{1}{N}\mathbb{T}\mathrm{r}\{\mathbf{R}_{\mathbf{HH}}-\mathbf{Q}_{\mathbf{t}}\mathbf{F}_{N\times L}\tilde{\mathbf{p}}^{H}\mathbb{E}[\mathbf{y}\mathbf{H}^{H}]-\mathbb{E}[\mathbf{H}\mathbf{y}^{H}]\tilde{\mathbf{p}}\mathbf{F}_{N\times L}^{H}\mathbf{Q}_{\mathbf{t}}{}^{H}+\mathbf{Q}_{\mathbf{t}}\mathbf{F}_{N\times L}\tilde{\mathbf{p}}^{H}\mathbb{E}[\mathbf{y}\mathbf{y}]^{H}\tilde{\mathbf{p}}\mathbf{F}_{N\times L}^{H}\mathbf{Q}_{\mathbf{t}}{}^{H}\}\\ &= \frac{1}{N}\mathbb{T}\mathrm{r}\Big\{\mathbf{R}_{\mathbf{HH}}-\mathbf{Q}_{\mathbf{t}}\mathbf{F}_{N\times L}\tilde{\mathbf{p}}^{H}\tilde{\mathbf{p}}\mathbf{R}_{\mathbf{hh}}\mathbf{F}_{N\times L}^{H}-\mathbf{F}_{N\times L}\mathbf{R}_{\mathbf{hh}}\tilde{\mathbf{p}}^{H}\tilde{\mathbf{p}}\mathbf{F}_{N\times L}^{H}\mathbf{Q}_{\mathbf{t}}{}^{H}\\ &\quad +\mathbf{Q}_{\mathbf{t}}\mathbf{F}_{N\times L}\tilde{\mathbf{p}}^{H}\left(\tilde{\mathbf{p}}\mathbf{R}_{\mathbf{hh}}\tilde{\mathbf{p}}^{H}+\sigma_n^2\right)\tilde{\mathbf{p}}\mathbf{F}_{N\times L}^{H}\mathbf{Q}_{\mathbf{t}}{}^{H}\Big\}. \qquad \text{(D.7)}\end{aligned}$$

Applying the fact that $\tilde{\mathbf{p}}^{H}\tilde{\mathbf{p}}=\mathbf{I}$ and (D.3), we have

$$\begin{aligned}\mathrm{MSE} &= \frac{1}{N}\mathbb{T}\mathrm{r}\{\mathbf{R}_{\mathbf{HH}}-\mathbf{Q}_{\mathbf{t}}\mathbf{R}_{\mathbf{HH}}-\mathbf{R}_{\mathbf{HH}}\mathbf{Q}_{\mathbf{t}}{}^{H}+\mathbf{Q}_{\mathbf{t}}\mathbf{R}_{\mathbf{HH}}\mathbf{Q}_{\mathbf{t}}{}^{H}+\sigma_n^2\mathbf{Q}_{\mathbf{t}}\mathbf{F}_{N\times L}\mathbf{F}_{N\times L}^{H}\mathbf{Q}_{\mathbf{t}}{}^{H}\}\\ &= \frac{1}{N}\mathbb{T}\mathrm{r}\{\mathbf{R}_{\mathbf{HH}}-\mathbf{Q}_{\mathbf{t}}\mathbf{R}_{\mathbf{HH}}-\mathbf{R}_{\mathbf{HH}}\mathbf{Q}_{\mathbf{t}}{}^{H}+\mathbf{Q}_{\mathbf{t}}(\mathbf{R}_{\mathbf{HH}}+\sigma_n^2\mathbf{F}_{N\times L}\mathbf{F}_{N\times L}^{H})\mathbf{Q}_{\mathbf{t}}{}^{H}\}\\ &= \frac{1}{N}\mathbb{T}\mathrm{r}\{\mathbf{R}_{\mathbf{HH}}-\mathbf{Q}_{\mathbf{t}}\mathbf{R}_{\mathbf{HH}}\} > \mathrm{MSE}' \qquad \text{(D.8)}\end{aligned}$$

which has exactly the same expression of the MSE obtained by frequency-domain MMSE estimation (eqn. (3.10)), except that $\mathbf{Q}_{\mathbf{t}}$ is replaced by $\mathbf{Q}$ in eqn. (3.10). We have shown in Chapter 3 that the lower bound MSE obtained by frequency-domain MMSE estimation is achieved when the pilot symbols have a flat spectrum. Or equivalently, the matrix $\mathbf{Q}$ that achieves the MSE lower bound for the frequency-domain MMSE estimation can be written as

$$\mathbf{Q} = \mathrm{R}_{\mathbf{HH}}(\mathrm{R}_{\mathbf{HH}}+\sigma_n^2\mathbf{I}_N)^{-1}. \qquad \text{(D.9)}$$

Since $\mathbf{F}_{N\times L}\mathbf{F}_{N\times L}^{H} \neq \mathbf{I}_N$, the matrix $\mathbf{Q_t}$ obtained by performing FFT on the estimated time-domain channel taps when time domain MSE lower bound is achieved (eqn. (3.6)) is not the same as (D.9). Therefore, the obtained MSE (D.8) cannot achieve the MSE lower bound obtained by the frequency-domain MMSE estimation. That is, although N frequency-domain channel taps can be obtained by performing Fourier transform on the L time-domain MMSE taps, this method does not result in the MSE lower bound achieved by the frequency-domain MMSE estimator that directly estimates N frequency-domain channel taps.

Appendix E

In this appendix, we derive the expression for $\xi_{1k} = \mathbb{E}[C_k]$. We know from (6.5) and (6.16) that

$$\begin{aligned} \Omega &= \mathbb{E}[C_k] \\ &= \int_{r_k}\int_{\theta_k} r_k e^{j\theta_k} f_{r_k,\theta_k}(r_k,\theta_k) dr_k d\theta_k \end{aligned} \tag{E.1}$$

Denote

$$\rho_{\pm}(r_k) = \frac{1-2Br_k^2 \pm \sqrt{1-4Br_k^2}}{r_k^3\sqrt{1-4Br_k^2}} \tag{E.2}$$

and

$$\lambda_{\pm}(r_k) = \frac{1 \pm \sqrt{1-4Br_k^2}}{4r_k^2\sigma_k^2}. \tag{E.3}$$

Eqn. (E.1) can be rewritten as

$$\begin{aligned} \Omega &= \frac{1}{4\pi\sigma_k^2} e^{-\frac{|\mu_k|^2-B}{2\sigma_k^2}} \times \\ &\quad \left\{ \int_{r_k}\int_{\theta_k} r_k\rho_+(r_k) e^{j\theta_k - \lambda_+(r_k)(1-2|\mu_k|r_k\cos(\theta_k+\phi_k))} \right. \\ &\quad \left. + \int_{r_k}\int_{\theta_k} r_k\rho_-(r_k) e^{j\theta_k - \lambda_-(r_k)(1-2|\mu_k|r_k\cos(\theta_k+\phi_k))} \right\} dr_k d\theta_k \\ &= \frac{1}{4\pi\sigma_k^2} e^{-\frac{|\mu_k|^2-B}{2\sigma_k^2}} (\Omega_1 + \Omega_2) \end{aligned} \tag{E.4}$$

where

$$\Omega_{1,2} = \int_{r_k} r_k\rho_{\pm}(r_k) e^{-\lambda_{\pm}(r_k)} \int_0^{2\pi} e^{j\theta_k + 2\lambda_{\pm}(r_k)|\mu_k|r_k\cos(\theta_k+\phi_k)} d\theta_k dr_k \tag{E.5}$$

and the sign $\pm$ applies to Ω_1 and Ω_2, respectively. Note that the inner integral in Ω_1 and Ω_2 can be simplified to

$$\begin{aligned}\Omega_\theta &= \int_0^{2\pi} \mathrm{e}^{j\theta_k + 2\lambda_\pm(r_k)|\mu_k| r_k \cos(\theta_k+\phi_k)} d\theta_k \\ &= \mathrm{e}^{-j\phi_k} \int_0^{2\pi} \mathrm{e}^{j(\theta_k+\phi_k) + 2\lambda_\pm(r_k)|\mu_k| r_k \cos(\theta_k+\phi_k)} d\theta_k \\ &= 2\pi \mathrm{e}^{-j\phi_k} I_1\left(2\lambda_\pm(r_k)|\mu_k| r_k\right). \end{aligned} \tag{E.6}$$

where I_n is the nth order modified Bessel function of the first kind.

The first integral Ω_1 in (E.4) now becomes

$$\begin{aligned}\Omega_1 &= 2\pi \mathrm{e}^{-j\phi_k} \int_{r_k} r_k \rho_+(r_k) \mathrm{e}^{-\lambda_+(r_k)} \mathrm{I}_1\left(2\lambda_+(r_k)|\mu_k| r_k\right) dr_k \\ &= 2\pi \mathrm{e}^{-j\phi_k} \int_{r_k} \frac{1 - 2Br_k^2 + \sqrt{1-4Br_k^2}}{r_k^2\sqrt{1-4Br_k^2}} \mathrm{I}_1\left(\frac{|\mu_k|\left(1+\sqrt{1-4Br_k^2}\right)}{2\sigma_k^2 r_k}\right) \mathrm{e}^{-\frac{1+\sqrt{1-4Br_k^2}}{4r_k^2\sigma_k^2}} dr_k. \end{aligned} \tag{E.7}$$

By making a change of variable in (E.7) as

$$t = \frac{|\mu_k|\left(1+\sqrt{1-4Br_k^2}\right)}{2\sigma_k^2 r_k}, \tag{E.8}$$

we have

$$r_k = \frac{t\sigma_k^2|\mu_k|}{t^2\sigma_k^4 + B|\mu_k|^2} \tag{E.9}$$

and

$$dr_k = \sigma_k^2|\mu_k| \frac{B|\mu_k|^2 - t^2\sigma_k^4}{(t^2\sigma_k^4 + B|\mu_k|^2)^2}. \tag{E.10}$$

Furthermore, since

$$r_k = \frac{\sqrt{R_k^2 + I_k^2}}{R_k^2 + I_k^2 + B}, \tag{E.11}$$

there is $r_k \in (0, \frac{1}{2\sqrt{B}})$. Therefore, $t \in \left(\infty, \frac{\sqrt{B}|\mu_k|}{\sigma_k^2}\right)$ and

$$\Omega_1 = \frac{4\pi\sigma_k^2}{|\mu_k|} \mathrm{e}^{-j\phi_k} \mathrm{e}^{-\frac{B}{2\sigma_k^2}} \int_{\frac{\sqrt{B}|\mu_k|}{\sigma_k^2}}^{\infty} \frac{t^2}{t^2 + \frac{B|\mu_k|^2}{\sigma_k^4}} \mathrm{I}_1(t) \mathrm{e}^{-\frac{\sigma_k^2}{2|\mu_k|^2}t^2} dt. \tag{E.12}$$

Similarly, we have

$$\Omega_2 = 2\pi e^{-j\phi_k} \int_{r_k} \frac{1-2Br_k^2-\sqrt{1-4Br_k^2}}{r_k^2\sqrt{1-4Br_k^2}} I_1\left(\frac{|\mu_k|\left(1-\sqrt{1-4Br_k^2}\right)}{2\sigma_k^2 r_k}\right) e^{-\frac{1-\sqrt{1-4Br_k^2}}{4r^2\sigma_k^2}} dr_k. \tag{E.13}$$

By a change of variable in (E.13)

$$t = \frac{|\mu_k|\left(1-\sqrt{1-4Br_k^2}\right)}{2\sigma_k^2 r_k} \tag{E.14}$$

where $t \in \left(0, \frac{\sqrt{B}|\mu_k|}{\sigma_k^2}\right)$, the second integral Ω_2 in (E.4) can be rewritten as

$$\Omega_2 = \frac{4\pi\sigma_k^2}{|\mu_k|} e^{-j\phi_k} e^{-\frac{B}{2\sigma_k^2}} \int_0^{\frac{\sqrt{B}|\mu_k|}{\sigma_k^2}} \frac{t^2}{t^2+\frac{B|\mu_k|^2}{\sigma_k^4}} I_1(t) e^{-\frac{\sigma_k^2}{2|\mu_k|^2}t^2} dt. \tag{E.15}$$

Applying (E.12) and (E.15) to (E.4) yields

$$\begin{aligned} \Omega &= \frac{1}{|\mu_k|} e^{-j\phi_k} e^{-\frac{|\mu_k|^2}{2\sigma_k^2}} \int_0^{\infty} \frac{t^2}{t^2+\frac{B|\mu_k|^2}{\sigma_k^4}} e^{-\frac{\sigma_k^2}{2|\mu_k|^2}t^2} I_1(t) dt \\ &= \frac{1}{\sqrt{2}\sigma_k} e^{-j\phi_k} e^{-\frac{|\mu_k|^2}{2\sigma_k^2}} \int_0^{\infty} \frac{\sqrt{u}}{u+\frac{|P_k|^2}{\sigma_b^2}} e^{-u} I_1\left(\eta_k\sqrt{u}\right) du \end{aligned} \tag{E.16}$$

where $\eta_k = \frac{\sqrt{2}|\mu_k|}{\sigma_k}$ and a change of variable $u = \frac{\sigma_k^2}{2|\mu_k|^2}t^2$ has been made. Therefore, the final expression for eqn. (E.1) can be obtained as

$$\Omega = \mathbb{E}[C_k] = \frac{1}{\sqrt{2}\sigma_k} e^{-j\phi_k} e^{-\frac{|\mu_k|^2}{2\sigma_k^2}} \Psi_k(\frac{1}{2}, 1, 1) \tag{E.17}$$

where $\Psi_k(\cdot)$ is defined as

$$\Psi_k(\varsigma, \tau, \upsilon) = \int_0^{\infty} \frac{u^{\varsigma}}{\left(u+\frac{|P_k|^2}{\sigma_b^2}\right)^{\tau}} e^{-u} I_{\upsilon}(\eta_k\sqrt{u}) du. \tag{E.18}$$